

Studies on Generation and Manipulation of Laser Cooled Atoms

By

Surjya Prakash Ram

PHYS03200704011

Raja Ramanna Centre for Advanced Technology, Indore

*A thesis submitted to the
Board of Studies in Physical Sciences*

*In partial fulfillment of requirements
For the Degree of*

DOCTOR OF PHILOSOPHY

of

HOMI BHABHA NATIONAL INSTITUTE



October, 2013

Homi Bhabha National Institute

Recommendations of the Viva Voce Board

As members of the Viva Voce Board, we certify that we have read the dissertation prepared by **Surjya Prakash Ram** entitled **Studies on Generation and Manipulation of Laser Cooled Atoms** and recommend that it may be accepted as fulfilling the dissertation requirement for the Degree of Doctor of Philosophy.

P. D. Gupta Date: 22/8/14
Chairman: Prof. P. D. Gupta

S R Mishra Date: 22-8-2014
Guide: Prof. S. R. Mishra

B. N. Jagatap Date: 22-08-2014
Member 1: Prof. B. N. Jagatap

H. S. Rawat Date: 22-08-2014
Member 2: Prof. H. S. Rawat

Arup Banerjee Date: 22-08-2014
Member 3: Prof. Arup Banerjee

Hema Ramachandran Date: 22/8/14
External Examiner: Prof. Hema Ramachandran

Final approval and acceptance of this dissertation is contingent upon the candidate's submission of the final copies of the dissertation to HBNI.

I hereby certify that I have read this dissertation prepared under my direction and recommend that it may be accepted as fulfilling the dissertation requirement.

Date: 22-8-2014
Place: RRcAT, Indore

Guide: S R Mishra
Prof. S. R. Mishra

STATEMENT BY AUTHOR

This dissertation has been submitted in partial fulfillment of requirements for an advanced degree at Homi Bhabha National Institute (HBNI) and is deposited in the Library to be made available to borrowers under rules of the HBNI.

Brief quotations from this dissertation are allowable without special permission, provided that accurate acknowledgement of source is made. Requests for permission for extended quotation from or reproduction of this manuscript in whole or in part may be granted by the Competent Authority of HBNI when in his or her judgment the proposed use of the material is in the interests of scholarship. In all other instances, however, permission must be obtained from the author.



Surjya Prakash Ram

DECLARATION

I, hereby declare that the investigation presented in the thesis has been carried out by me. The work is original and has not been submitted earlier as a whole or in part for a degree / diploma at this or any other Institution / University.



Surjya Prakash Ram

List of Publications arising from the thesis

Journal

1. “Enhanced atom transfer in a double magneto-optical trap setup”, S. R. Mishra, S. P. Ram, S. K. Tiwari and S. C. Mehendale, *Phys. Rev. A*, **2008**, Vol. 77, 065402(1-4).
2. “A comparison of pulsed and continuous atom transfer between two magneto-optical traps”, S. P. Ram, S. K. Tiwari and S. R. Mishra, *J. Korean Phys. Soc.*, **2010**, Vol. 57, 1303-1307.
3. “Investigation of atom transfer using a red-detuned push beam in a double magneto-optical trap setup”, S. P. Ram, S. R. Mishra, S. K. Tiwari and S. C. Mehendale, *Rev. Sci. Instrum.*, **2011**, Vol. 82, 126108(1-3).
4. “Push beam spot-size dependence of atom transfer in a double magneto-optical trap setup”, S. P. Ram, S. K. Tiwari, S. R. Mishra and H. S. Rawat, *Rev. Sci. Instrum.*, **2013**, Vol. 84, 073102(1-6).
5. “Optimization of transfer of laser-cooled atom cloud to a quadrupole magnetic trap”, S. P. Ram, S. K. Tiwari, S. R. Mishra and H. S. Rawat, *Pramana J. Phys.*, **2014**, Vol. 82, p. 419-423.
6. “Temperature and phase-space density of cold atom cloud in a quadrupole magnetic trap”, S. P. Ram, S. R. Mishra, S. K. Tiwari and H. S. Rawat, *J. Korean Phys. Soc.*, **2014** (in Press).

Conferences

1. “Generation of optical pulses with a variable delay from a single beam using AOMs in tandem: Application to temperature measurement of cold atoms”, S. P. Ram, S. R. Mishra and S. K. Tiwari, *Proceedings of DAE-BRNS National Laser Symposium (NLS-07)*, Dec. 17-20, **2007**, (Vadodara, India).
2. “A study on temporal evolution of temperature in optical molasses”, S. P. Ram, S. K. Tiwari, S. R. Mishra and S. C. Mehendale, *Proceedings of DAE-BRNS National Laser Symposium (NLS-08)*, Jan. 7-10, **2009**, (LASTEC, New Delhi).
3. “Enhanced transfer of cold atoms between two MOTs using a pulsed push beam”, S. P. Ram, S. K. Tiwari and S. R. Mishra, *Proceedings of DAE-BRNS National Laser Symposium (NLS-09)*, Jan. 13-16, **2010** (BARC, Mumbai).

4. “Magnetic trapping of ^{87}Rb atoms”, S. P. Ram, S. K. Tiwari, S. R. Mishra and S. C. Mehendale, *Proceedings of DAE-BRNS National Laser Symposium (NLS-19)*, Dec. 01-04, **2010**, (RRCAT, Indore).
5. “Investigation of atom transfer by resonant and off-resonant push beam in a double magneto-optical trap setup”, S. P. Ram, S. K. Tiwari, S. R. Mishra and S. C. Mehendale, *Proceedings of DAE-BRNS National Laser Symposium (NLS-19)*, Dec. 01-04, **2010**, (RRCAT, Indore).
6. “Optimization of transfer of laser cooled atom cloud to a quadrupole magnetic trap”, S. P. Ram, S. K. Tiwari, S. R. Mishra and H. S. Rawat, *Proceedings of DAE-BRNS National Laser Symposium (NLS-21)*, Feb. 6-9, **2013**, (BARC, Mumbai).
7. “Push beam spot -size dependence on atom transfer in a double-MOT setup”, S. P. Ram, S. K. Tiwari, S. R. Mishra and H. S. Rawat, *Proceedings of DAE-BRNS National Laser Symposium (NLS-21)*, Feb. 6-9, **2013**, (BARC, Mumbai).



Surjya Prakash Ram

Dedicated to

Papa,

My loving wife & sweet daughter Anwasha

ACKNOWLEDGEMENTS

It is my great pleasure to thank the people who have helped and inspired me during this thesis work.

I sincerely thank my Ph. D. guide Dr. S. R. Mishra for his continued help, encouragement and guidance throughout the course of this work. His enthusiasm, dedication and motivating approach have kept me inspired all the time, which proved to be of great help in completing this Ph. D. work. I also want to thank him for his care and attention towards my progress as a researcher.

I am also thankful to Dr. H. S. Rawat, Head, LPAS, RRCAT, who has always supported me during this work. His encouraging words have always kept my morale high throughout this work. I am also grateful to Dr. S. C. Mehendale, Ex-Head, LPAD, RRCAT, for his encouragement, help and support during this work. I also take this opportunity to thank Dr. P. D. Gupta, Director, RRCAT, for his keen interest in my work and continuous help and support provided by him during this Ph. D. work.

Thanks are also due to the Doctoral Committee members Dr. P. D. Gupta (Chairman), Dr. B. N. Jagatap, Dr. H. S. Rawat, Dr. S. R. Mishra (Guide) and Dr. Arup Banerjee for their valuable suggestions and constructive comments during each Doctoral Committee meetings, which proved to be instrumental in improving overall scientific and technical quality of the work presented in this thesis.

I am also thankful to my collaborator Shri S. K. Tiwari for his collaboration and the help provided at various stages of this work. I also thank my colleagues Dr. V. B. Tiwari, Shri Surendra Singh and Shri Vivek Singh for several scientific and technical help provided by them. Thanks are also due to Smt Lalita Jain, LESD, RRCAT and Shri K. V. A. N. P. S. Kumar, UHVTL, RRCAT, who offered their technical help with great enthusiasm as and when I approached them. I also thank Shri Sanjiv Tiwari, Shri Surendra Singh, Dr. M. M. Manekar and Dr. Y. Verma for a careful reading of the thesis chapters.

I also thank to the colleagues of LPAS, RRCAT for making a lively and healthy

research environment which kept me up all the time during this work. Thanks are also due to the office staff members Smt Sapna Rege, Shri P. N. Ravindran and Shri Kailash Parmar for their help whenever the need arose.

I am deeply indebted to my mother Smt Padmabati Ram whose enormous love and affection have contributed to this work in its own way. I also want to thank my sisters (Smt Rashmi and Kum Lovely) and brother (Shri Trideo) for their love, affection and moral encouragement.

Finally, my heart-felt thanks are due to my wife Dr. Nibedita Ram for her love, care and constant support during my research work. She also participated in various scientific discussions with me and helped me to be correct whenever I was not so. I also thank my sweet daughter Anvesha, whose arrival made my life filled with joy and happiness. I also extend my gratitude towards my in-laws family for their support and love.

Surjya Prakash Ram

Contents

Synopsis	iv
List of figures	xiii
1 Introduction	1
1.1 Fundamentals of laser atom cooling and trapping	2
1.1.1 Laser atom interaction: manipulation of atomic motion	3
1.1.2 Optical pumping: internal state manipulation	5
1.1.3 Laser Doppler cooling mechanism	6
1.1.4 Optical molasses	7
1.1.5 Magneto-optical trap	7
1.1.6 A Magneto-optical trap for Rb atoms	9
1.1.7 Doppler cooling limit	10
1.1.8 Sub-Doppler Cooling	10
1.2 Magnetic trapping of atoms	11
1.2.1 Quadrupole trap	12
1.2.2 Quadrupole-Ioffe configuration trap (QUIC trap)	13
1.3 Evaporative cooling	14
1.4 Bose-Einstein condensation (BEC)	14
1.5 Applications of cold atoms	17
2 Experimental Apparatus	19
2.1 Introduction	19

2.2	Vacuum system of the experimental setup	20
2.2.1	Vacuum chamber for VC-MOT	22
2.2.2	Vacuum chamber for UHV-MOT	22
2.2.3	Design considerations for the differential pumping	23
2.2.4	Getters as a source of Rubidium vapor	25
2.2.5	Procedure followed to achieve the desired vacuum	25
2.3	Laser systems and optical layout	27
2.3.1	Frequency stabilization of ECDL systems	28
2.3.2	Generation of various optical beams	31
2.4	MOT coils	35
2.5	Formation of MOTs	35
2.6	Characterization of cold atoms in MOTs	36
2.6.1	Measurement of number of atoms in MOT	36
2.6.2	Measurement of atom cloud temperature	38
2.7	Design of magnetic trap	39
2.8	Loading of a magnetic trap	41
2.9	Evaporative cooling system	42
2.10	Absorption probe imaging	43
2.11	Controller system	44
2.12	Summary	48
3	Atom transfer with resonant push beam	49
3.1	Introduction	49
3.2	Use of resonant push beam in presence of a hollow beam for atom transfer	50
3.2.1	Description of the setup with hollow beam	51
3.2.2	Result on atom transfer in presence of hollow beam	54
3.3	Continuous versus pulsed push beam for atom transfer	58
3.3.1	Experimental Description	59
3.3.2	Observation and results	61
3.4	Summary	66

4	Atom transfer with red-detuned push beam	67
4.1	Introduction	67
4.2	Use of a red-detuned push beam in retro-reflection geometry	68
4.2.1	Experimental setup for push beam in retro-reflection geometry	68
4.2.2	Results on atom transfer with push beam in retro-reflection geometry	69
4.3	Dependence of red-detuned push beam spot-size on atom transfer	75
4.3.1	The description of the experimental setup	76
4.3.2	Results on push beam spot-size dependent atom transfer	77
4.4	Summary	84
5	Magnetic trapping of laser cooled ^{87}Rb atoms and evaporative cooling in the magnetic trap	85
5.1	Introduction	85
5.2	Magnetic trapping of laser cooled atoms	86
5.3	Preparation of UHV-MOT atom cloud for magnetic trapping	87
5.4	Characterization of atom cloud in the quadrupole magnetic trap	91
5.5	Studies on phase-space density in the quadrupole magnetic trap	94
5.6	Formation of QUIC trap	103
5.7	Evaporative cooling in the magnetic trap	105
5.8	Summary	107
6	Conclusions	109
	Bibliography	113



Homi Bhabha National Institute

Ph. D. PROGRAMME

1. Name of the Student	: Surjya Prakash Ram
2. Name of the Constituent Institution	: Raja Ramanna Centre for Advanced Technology
3. Enrolment No.	: PHYS03200704011
4. Title of the Thesis	: Studies on Generation and Manipulation of Laser Cooled Atoms
5. Board of Studies	: Physical Sciences

SYNOPSIS

Over the last few decades there has been a phenomenal progress in the field of ultra-cold atoms. The field has seen amazingly new developments, which include ultra-precision spectroscopy, ultra-cold collision physics, quantum optics, cold molecules, matter wave optics, ultra-cold plasmas and most importantly Bose-Einstein condensation (BEC) [1-4]. Experimental realization of BEC is, perhaps, the landmark accomplishment of ultra-cold atom research and that has led to an explosive growth of research in quantum degenerate gases including metastable and fermionic atoms, superfluidity, quantized vortices, Josephson junction, quantum phase transitions etc. It has also provided an opportunity to study the wave particle duality of matter and has formed the basis of research in non-linear and quantum atom optics. The applications of laser-cooled atoms are equally fascinating and include, for example, precision atomic clocks [1], ultra-precise gravity gradiometer [3], atom lithography [5] and quantum information processing [4]. Underlying this explosive growth are the innovative techniques of generation and manipulation of ultra-cold atoms.

This thesis deals with development of techniques for generation and characterization of cold atomic samples in the range of few hundred μK to $1\ \mu\text{K}$ temperature and their use in going over to quantum degeneracy. A double magneto-optical trap (MOT) setup for ^{87}Rb atoms, consisting of a vapor chamber MOT (VC-MOT) and an ultra-high vacuum MOT (UHV-MOT), is developed in-house and used for study of transfer of cold atoms from VC-MOT to UHV-MOT, magnetic trapping of atoms and optimization of phase-space density, and evaporative cooling in a magnetic trap for generation of ultra-cold atoms.

In the double-MOT setup [6], transfer of atoms from VC-MOT to the UHV-MOT is of prime importance for implementation of evaporative cooling in magnetic trap. This transfer process has been investigated in detail, which has bearing on the achievement of a large number of atoms in the UHV-MOT in a double-MOT setup. In the atom transfer studies, a push beam has been used for transfer of atoms from the VC-MOT to the UHV-MOT in different geometries and configurations to maximize the number of atoms in the UHV-MOT. It is found that a pulsed resonant push beam with a low power can result in higher number of atoms accumulated in the UHV-MOT than the continuous wave (CW) push beam. The experimental results have been explained on the basis of parameters affecting the atom transfer in both the cases. The investigations during this work revealed that use of a red-detuned (and higher power) continuous wave push beam of an optimized spot-size results in the maximum number of atoms in the UHV-MOT. The number of atoms transferred to the UHV-MOT is also dependent on the push beam power, its detuning, and capture speed of the UHV-MOT.

Using the above mentioned double-MOT setup, the transfer of laser cooled atom cloud from UHV-MOT/molasses to a magnetic trap [7] has also been studied. It is shown explicitly that the temperature and r.m.s. size of the laser cooled atom cloud in the molasses governs the value of optimum magnetic field gradient at which the phase space density in the magnetic trap can be maximum.

In order to generate the ultra-cold atomic samples of ^{87}Rb , the evaporative cooling of ^{87}Rb atoms in a Quadrupole-Ioffe configuration (QUIC) magnetic trap [8] has been performed. For this, atoms trapped in magnetic trap are subjected to a variable frequency RF field to effect evaporation. After evaporative cooling, a typical bimodal distribution in the optical density profile of the evaporatively cooled cloud is observed indicating the evidence

of occurrence of BEC in the cold atomic cloud.

The thesis is organized in six chapters and work included there is detailed below:

Chapter 1 provides a brief introduction to the subject of cooling and trapping of atoms including various techniques of laser cooling, magnetic trapping and evaporative cooling. Various kinds of forces like scattering force and dipole force due to the interaction of atoms with laser beams are also described. This chapter thus provides the experimental and theoretical basis for the work reported in the subsequent chapters.

Chapter 2 describes various cooling and trapping systems developed in-house for ^{87}Rb atoms. These include MOT, double-MOT, magnetic trap, evaporative cooling and detection systems. The discussion also covers developments relating to frequency stabilization of lasers, vacuum systems, magnetic trap coils, and controller system for execution of various processes in a synchronized manner. These systems are used to investigate the atom transfer processes, magnetic trapping and evaporative cooling described in subsequent chapters. The double-MOT setup consists of a vapor chamber MOT (VC-MOT) at $\sim 1\text{-}2 \times 10^{-8}$ Torr pressure (with Rb-vapor) and an UHV-MOT at $\sim 5 \times 10^{-11}$ pressure. The objective of developing a double-MOT setup is to collect a large number of atoms in the VC-MOT (having a higher vapor pressure $\sim 10^{-8}$ Torr) and then transfer the collected atoms to the UHV environment for magnetic trapping and evaporative cooling.

Chapter 3 discusses the transfer of atoms from VC-MOT to UHV-MOT using a resonant push beam. Firstly we discuss the use of a resonant push beam in continuous wave (CW) mode in conjunction with an auxiliary hollow beam having dark centre in the transverse intensity profile. An indigenously developed axicon mirror is used for the generation of the hollow beam. The optical arrangement consists of a weakly focused hollow laser beam propagating opposite to the push beam direction such that both the MOTs (VC-MOT and UHV-MOT) are in the dark region of the hollow beam. Significant enhancement in the number of atoms in the UHV-MOT is observed in the presence of the hollow beam when its frequency is tuned near the cooling transition of ^{87}Rb atom. Various processes involved in the enhancement of the number of atoms in UHV-MOT are investigated. It is found that for a red-detuned hollow beam, the enhancement is due to cooling of atoms in the flux from VC-MOT, whereas, for the blue-detuned hollow beam, the enhancement observed in number of atoms in UHV-MOT is due to transverse guiding of atoms in the flux by push beam which

provides a higher number reaching the UHV-MOT volume. Further a comparative study of CW transfer and pulsed transfer of atoms between two MOTs using a resonant push beam is made. Here we study the transfer of atoms from VC-MOT to UHV-MOT in four different forms of push beam, namely - (i) CW focused, (ii) CW unfocused, (iii) pulsed focused, and (iv) pulsed unfocused, and compare the results in terms of number of atoms accumulated in UHV-MOT. It is found that the use of a pulsed unfocused push beam on a partially loaded VC-MOT cloud in repetitive cycles can result a higher number of atoms accumulated in UHV-MOT than the number obtained in UHV-MOT either with CW focused/unfocused push beam or with pulsed focused push beam. In the experiments with pulsed unfocused push beam, we observe that VC-MOT duration and push beam duration, both, have optimum values to get maximum number of atoms in UHV-MOT. The processes affecting number of atoms accumulated in UHV-MOT have been investigated in detail, which are described in this chapter.

Chapter 4 details the use of a red-detuned push beam in the atom transfer process in the above described double-MOT setup. The pushing and guiding effect of a red-detuned beam is reported here. The advantage of using a red-detuned push beam over a resonant push beam is also discussed. The chapter begins with the discussion on the use of a red-detuned push beam in retro-reflection geometry. As is well-known that the guiding effect due to dipole potential of push beam is intensity dependent, we have used the push beam in retro-reflection geometry to enhance the guiding dipole potential of push beam for the atoms in the flux. Due to increased push beam intensity, this geometry provides a stronger confinement and guiding of atoms in the flux transferred from VC-MOT to UHV-MOT which has helped in enhancing the number of atoms in the UHV-MOT. The discussion is then followed by studies of the effect of push beam spot-size and power on the number of atoms accumulated in the UHV-MOT. Experimentally it is observed that the number of atoms accumulated in UHV-MOT varies with the push beam spot-size (for a given power) at the VC-MOT and attains a maximum value at an optimum push beam spot-size. We find that the number of atoms accumulated in the UHV-MOT in the different regime of push beam spot-size is dependent on the capture speed of the UHV-MOT, speed of the atom flux from VC-MOT, the rate of number of atoms reaching the UHV-MOT, and the guiding potential experienced by the atoms during transfer.

Chapter 5 is devoted to studies involving magnetic trapping and evaporative cooling. For evaporative cooling of atoms in the magnetic trap, the higher energy atoms from the trap are removed by the application of radio frequency radiation, leading to decrease in the temperature and increase in the phase-space density. The phase-space density (ρ) is given as $\rho = n\lambda_{dB}^3$, where n is the number density and λ_{dB} is the thermal de-Broglie wavelength. Since the evaporative cooling is required to reach the final phase-space density $\rho \sim 1$ for attainment of BEC, the initial phase-space density of atoms in the magnetic trap is of significant importance. This in turn depends on the parameters during the transfer of laser cooled atom cloud from the molasses to quadrupole magnetic trap. We have studied the transfer of cold atoms from molasses stage to a quadrupole magnetic trap. It is shown that by choosing the experimental parameters appropriately, the phase space density of the atom cloud in the magnetic trap can be maximized after transfer of atoms from the molasses to the magnetic trap. Further, for a given temperature and size of the molasses cloud, there exists an optimum value of magnetic field gradient for which the phase space density in the quadrupole magnetic trap is maximum.

Atoms trapped in quadrupole trap are transferred to a Quadrupole-Ioffe configuration (QUIC) trap which removes the drawback of Majorana spin-flip losses of atoms in quadrupole trap. The ^{87}Rb atoms in the QUIC trap were subjected to evaporative cooling by applying a variable frequency RF radiation from a single loop antenna. We repeated RF-evaporation cycles with different ranges of frequency scan and different powers of RF source. The evaporatively cooled cloud of atoms is characterized by absorption probe imaging technique. For certain set of parameters for evaporative cooling, we observed a bimodal distribution in the optical density profile of the cloud, which is indicative of Bose-Einstein condensation of atoms in the cloud. The dependence of this bimodal distribution on the final frequency of RF field during the scan confirms the occurrence of BEC in the trapped atom cloud.

Finally the main conclusions of the research work as well as the scope of future work are presented in **Chapter 6**.

References:

1. "*Advances in Atomic Physics: An Overview*", Claude Cohen-Tannoudji and David Guéry-Odelin, World Scientific, Hackensack, NJ, (2011).

2. “*Bose-Einstein Condensation in Atomic Gases*”, Proceedings of the International School of Physics “Enrico Fermi,” Course CXL, Varenna, 1998, (edited by M. Inguscio, S. Stringari, and C. E. Wieman, IOS Press, Amsterdam, 1999).
3. “*Atomic interferometry and Laser Spectroscopy*”, Ch. J. Bordé, in *Laser Spectroscopy X*, Ed. M. Ducloy; “Atom Interferometry”, ed. Paul R. Berman (Academic Press, 1997); High precision gravity measurements using atom interferometry, A. Peters et al, *Metrologia* 38, 25 (2001).
4. J J García-Ripoll, P Zoller, and J I Cirac, *J. Phys. B: At. Mol. Opt. Phys.* 38, S567 (2005).
5. “*Laser cooling and trapping*”, H. J. Metcalf and P. van der Straten, Springer-Verlag New York, 1999.
6. C. J. Myatt, N. R. Newbury, R. W. Ghrist, S. Loutzenhiser, and C. E. Wieman, *Opt. Lett.* 21, 290 (1996).
7. A. L. Migdall, J. V. Prodan, W. D. Phillips, T. H. Bergeman and H. J. Metcalf, *Phys. Rev. Lett.* 54, 2596, (1985).
8. T. Esslinger, I. Bloch and T. W. Hänsch. *Phys. Rev. A* 58, R2664 (1998).

List of Publications:

Journal Articles

(Included in the thesis)

a. Published

1. Push beam spot-size dependence of atom transfer in a double magneto-optical trap setup
S. P. Ram, S. K. Tiwari, S. R. Mishra, H. S. Rawat
Rev. Sci. Instrum., Vol. 84, p. 073102, 2013.
2. Investigation of atom transfer using a red-detuned push beam in a double magneto-optical trap setup
S. P. Ram, S. R. Mishra, S. K. Tiwari, S. C. Mehendale
Rev. Sci. Instrum., Vol. 82, no. 12, p. 126108, 2011
3. A comparison of pulsed and continuous atom transfer between two magneto-optical traps
S. P. Ram, S. K. Tiwari, S. R. Mishra
J Korean Phys Soc, Vol. 57, no. 5, p. 1303, 2010.
4. Enhanced atom transfer in a double magneto-optical trap set-up,
S. R. Mishra, S. P. Ram, S. K. Tiwari, S. C. Mehendale,
Phys Rev A, Vol. 77, no. 6, p. 065402, 2008.

b. To be submitted

5. Optimization of phase space density in loading of a quadrupole magnetic trap,
S. P. Ram, S. K. Tiwari, S. R. Mishra, H. S. Rawat

(Not included in the thesis)

6. Collective modes of a quasi-two-dimensional Bose condensate in large gas parameter regime,
S. R. Mishra, S. P. Ram, A. Banerjee,
Pramana: Journal of Physics, Vol. 68, no. 6, p. 913, 2007.

Conference Presentations/Publications

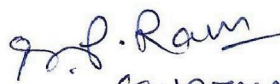
1. Push beam spot -size dependence on atom transfer in a double-MOT setup
S. P. Ram, S. K. Tiwari, S. R. Mishra, H. S. Rawat
DAE-BRNS National Laser Symposium (NLS-21), BARC, Mumbai, Feb., 6-9, 2013
2. Optimization of transfer of laser cooled atom cloud to a quadrupole magnetic trap
S. P. Ram, S. K. Tiwari, S. R. Mishra, H. S. Rawat
DAE-BRNS National Laser Symposium (NLS-21), BARC, Mumbai, Feb., 6-9, 2013
3. Magnetic trapping of laser cooled ^{87}Rb atoms in a Quadrupole-Ioffe configuration trap with a metal core Ioffe coil
S. P. Ram, S. K. Tiwari, S. R. Mishra,
DAE-BRNS National Laser Symposium (NLS-20), Anna University, Chennai, Jan., 9-12, 2012, p. 749
4. Investigation of atom transfer by resonant and off-resonant push beam in a double magneto-optical trap setup
S. P. Ram, S. K. Tiwari, S. R. Mishra, S. C. Mehendale
DAE-BRNS National Laser Symposium (NLS-19), RRCAT, Indore, Dec., 01-04, 2010
5. Magnetic trapping of ^{87}Rb atoms
S. P. Ram, S. K. Tiwari, S. R. Mishra, S. C. Mehendale
Proc. DAE-BRNS National Laser Symposium (NLS-19), RRCAT, Indore, Dec., 01-04, 2010
6. A novel technique to store and process absorption probe images of cold atom cloud
H. S. Vora, **S. P. Ram, S. R. Mishra**
Proc. DAE-BRNS National Laser Symposium (NLS-19), RRCAT, Dec., 01-04, 2010
7. Enhanced transfer of cold atoms between two MOTs using a pulsed push beam,
S. P. Ram, S. K. Tiwari and S. R. Mishra,
Proc. NLS-09, January 13-16, 2010 (BARC, Mumbai).
8. Detection of state-manipulated population in ^{87}Rb -MOT by absorption probe imaging,

S. K. Tiwari, **S. P. Ram** and S. R. Mishra,

Poster presented in *Topical Conference on Atomic Molecular and Optical Physics (TC-2010)*, 3-6 March 2010, RRCAT, Indore.

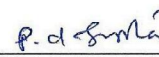
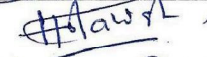
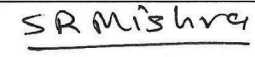
9. A study on temporal evolution of temperature in optical molasses,
S. P. Ram, S. K. Tiwari, S. R. Mishra and S. C. Mehendale,
Proc. NLS-08, January 7-10, 2009, (LASTEC, New Delhi).
10. A modified QUIC trap with metal-core Ioffe coil,
S. R. Mishra, S. Patidar, **S. P. Ram**, and S. K. Tiwari,
Proc. NLS-08, January 7-10, 2009, (LASTEC, New Delhi).
11. Generation of optical pulses with a variable delay from a single beam using AOMs in tandem: Application to temperature measurement of cold atoms,
S. P. Ram, S. R. Mishra, S. K. Tiwari,
Proc. NLS-07, Dec., 17-20, 2007, (Vadodara, India).
12. Use of a hollow laser beam to improve atom transfer in a double-MOT system,
S. R. Mishra, **S. P. Ram**, S. K. Tiwari, S. C. Mehendale,
Proc. NLS-07, Dec., 17-20, 2007, (Vadodara, India).

Signature of Student


(SURJYA PRAKASH RAM)

Date 8th Sept. 2013.

Doctoral Committee:

S. No.	Name	Designation	Signature	Date
1.	Dr. P. D. Gupta	Chairman		8.9.2013
2.	Dr. B. N. Jagatap	Member		8.9.2013
3.	Dr. H. S. Rawat	Member		8/9/2013
4.	Dr. A. Banerjee	Member		8.9.2013
5.	Dr. S. R. Mishra	Convener (Guide)		8.9.2013

List of Figures

1.1	A temperature and 1D-velocity scale in the context of laser cooling of Rubidium atom.	2
1.2	Principle of optical pumping for a $F = 1/2 \rightarrow F' = 1/2$ transition. . . .	5
1.3	Configuration of a MOT used in our experiments. In the MOT, three pairs of $(\sigma^+ - \sigma^-)$ laser beams of equal intensity and frequency are used. The magnetic field gradient is generated by a pair of coils placed in quadrupole configuration (the white arrows depicts the current direction in the coils).	8
1.4	(a): Quadrupole trap formed by two identical coils carrying current in opposite directions (shown by arrow).(b): Variation in magnetic trap potential with position. The solid line and dashed line show the potential experienced by the low field seeking and high field seeking states respectively.	12
1.5	(a):Schematic of the QUIC trap (formed by three coils: two quadrupole coils and an Ioffe coil; current direction in the coils are shown by arrow).(b): Magnetic field distribution along the Ioffe coil axis.	13
2.1	Schematic of the vacuum system. RG: Rubidium getters, DPT: differential pumping tube, GC: glass cell, BA: Bayerd-Alpert Gauge, EG: extractor gauge, NEG: non-evaporable getter pump, SIP & NEG: combination pump of sputter ion pump and NEG module. A sputter-ion pump of capacity 20 l/s and a turbo molecular pump of capacity 70 l/s in conjunction with a NW63CF pneumatic gate valve is connected to the upper part of the chamber (not shown).	21
2.2	Image of the vacuum system.	22

2.3	Two chambers at pressure P_1 and P_2 are connected using a tube of conductance C and a pump of pumping speed S	24
2.4	The schematic of the frequency detuning of various lasers used in the experiments with respect to the hyperfine atomic transitions of ^{87}Rb atom. Δ_C is the set detuning of the cooling laser, and Δ_{PB} is the detuning of the push beam laser. Δ_{PB} is set to zero for resonant push beam experiments, whereas, it is varied from 0 to -1.2 GHz for red-detuned experiments. Both the transitions $(5S_{1/2} F = 2) \rightarrow (5P_{3/2} F' = 3)$ and $(5S_{1/2} F = 1) \rightarrow (5P_{3/2} F' = 2)$ have the natural line-width of ~ 6 MHz. Diagram not to scale.	28
2.5	The schematic of the saturated absorption spectroscopy (SAS) setup. ECDL: extended-cavity diode laser, FI: Faraday isolator, $\lambda/2$: half-wave retardation plate, PBS: polarizing beam splitter cube, GP: glass plate, M: mirror, BD: beam dump, NPBS: non-polarizing beam splitter cube, PD1 and PD2 are the photodiodes, p1 and p2 are probe beams. OSC: Oscilloscope.	30
2.6	Saturated absorption signals generated in a SAS setup. The transitions for the corresponding peaks and cross-overs are shown in the figure. (a) and (b) corresponds to the spectrum for transitions $(5S_{1/2} F = 2) \rightarrow (5P_{3/2} F')$ and $(5S_{1/2} F = 1) \rightarrow (5P_{3/2} F')$ respectively.	31
2.7	A photograph of the table. The lines shows the path of the various generated optical beams. The lines with double arrows represents the AOMs in double-pass configuration. The Splitting of VC-MOT beams and UHV-MOT beams are not shown here. Refer to the text for more details.	32
2.8	Schematic of the fluorescence imaging technique. A typical fluorescence image of a MOT is also shown.	37
2.9	Schematic of the arrangement of the coils in QUIC trap for our setup.	40
2.10	Variation in the magnetic field along the Ioffe coil axis with distance at quadrupole coil current 23 A and variable Ioffe current. The solid lines show the simulated magnetic field.	40

2.11	Schematic of the RF field stimulated transitions leading to ejection of an atom during RF-evaporation process.	42
2.12	Image of the single loop antenna used for radiating the RF-field.	42
2.13	An image of the optical density of a cloud after RF evaporation. The profile along a horizontal line is shown in the graph.	43
2.14	Schematic of the absorption probe technique. A typical CCD image of probe beam transmitted through ^{87}Rb atom cloud is also shown. The dark spot near the centre in the image shows the absorption of probe intensity by atom cloud.	44
2.15	An image of the graphical user interface used for entry of various parameters for execution of the different events.	46
3.1	Schematic of the experimental setup. DLB: diode laser beam, AX: axicon mirror, $\lambda/2$: half wave plate, $\lambda/4$: quarter wave plate, PBS: polarizing beam splitter, L1, L2, L3: lenses of 80 mm, 250 mm, 300 mm focal length, HB: hollow beam, MB: MOT beams, PB: push beam, IP: sputter ion pump, G: vacuum gauge, GC: glass cell, QC: quadrupole coil, DPT: differential pumping tube, upper MOT:VC-MOT and lower MOT:UHV-MOT.	52
3.2	Intensity profiles of the hollow beam at different positions. (a): at VC-MOT, (b): at 5 mm below the VC-MOT, and (c): at UHV-MOT. The hollow beam images are shown in the right hand side of the figure.	53
3.3	Measured variation of number of atoms in UHV-MOT (lower MOT) with detuning of hollow beam frequency; (a) at hollow beam power of 23 mW and (b) at hollow beam power of 28 mW. The squares show the measured values and dashed curves are for guiding the eye to the measured data. The horizontal lines show the number in the absence of hollow beam.	55
3.4	Variation of number of atoms in VC-MOT (upper MOT) with detuning of hollow beam frequency. The squares show the measured values and dashed curve is to guide eye to the measured data. The horizontal line shows the number in the absence of hollow beam.	56

3.5	Schematic of the experimental setup and sequence of pulses for the pulsed push beam transfer scheme (τ_{VM} : duration of VC-MOT and τ_{PB} : push beam duration).	59
3.6	Variation in number of atoms in the UHV-MOT with τ_{PB} (duration of the unfocused push beam) for different VC-MOT loading durations τ_{VM} . The continuous horizontal line and dashed line show the numbers of atoms in the UHV-MOT for a focused CW push beam and an unfocused CW push beam, respectively, both with optimized powers.	63
3.7	The measured variation in temperature of the VC-MOT cloud with VC-MOT loading duration (τ_{VM}).	65
4.1	Schematic of the experimental setup. Here ‘ d ’ is the separation between UHV-MOT center and push beam retro-reflecting mirror.	70
4.2	Observed variation in number of atoms in UHV-MOT with push beam frequency detuning $\delta/2\pi$ from ($5S_{1/2} F = 2$) \rightarrow ($5P_{3/2} F' = 3$) transition of ^{87}Rb for push beam power of ~ 21 mW and $d = 135$ mm. Characteristic error bars determined from scatter in the values obtained in repeated measurements are shown for some data points.	71
4.3	Calculated variation of dipole potential and scattering force at UHV-MOT centre with push beam frequency detuning ($\delta/2\pi$) (from cooling transition peak of ^{87}Rb) for a fixed push beam power of ~ 21 mW and $d = 135$ mm. Here resultant denotes the sum of dipole potentials (scattering forces) due to forward and retro-reflected beams with appropriate sign.	73
4.4	Measured variation in UHV-MOT fluorescence with input push beam power at fixed push beam frequency detuning of $\delta/2\pi = -1.1$ GHz from the cooling transition of ^{87}Rb . Squares and circles show data obtained with retro-reflected push beam for $d = 55$ mm and 135 mm respectively, whereas crosses show data without retro-reflection of push beam. Characteristic error bars determined from scatter in the values obtained in repeated measurements are shown for some data points.	74

-
- 4.5 (A) Measured variation in number of atoms in UHV-MOT (capture speed $v_c = 20.2$ m/s) with push beam spot-size for different powers in push beam; (a): 15 mW, (b): 20 mW and (c): 25 mW. (B) Measured variation after modifying the v_c for UHV-MOT to 18.4 m/s (curve (e)), for a push beam power of 20 mW. For comparison, the data of curve (b) in (A) with higher v_c value ($= 20.2$ m/s) is replotted as curve (d) in (B). 77
- 4.6 Calculated variation in speed of an atom ejected from the VC-MOT with push beam spot-size for different values of push beam power. The continuous horizontal line shows the estimated capture speed of UHV-MOT ($v_c = 20.2$ m/s). 79
- 4.7 The calculated variation in the peak dipole potential of push beam with distance from VC-MOT along propagation direction, for the push beam spot-size of $200 \mu\text{m}$ at the VC-MOT position. Different curves show the potential for ^{87}Rb atoms in different hyperfine states at different push beam powers. The arrow indicates the position of UHV-MOT where atoms are pumped to ($5S_{1/2} F = 2$) state due to presence of the UHV-MOT re-pumping beam. 82
- 4.8 Loading graph of UHV-MOT for different values of push beam spot-size at the VC-MOT; (a) spot-size $146 \mu\text{m}$ (power 15 mW) and (b) spot-size $172 \mu\text{m}$ (power 20 mW). The continuous curves are for guiding eye to the measured data. 83
- 5.1 Variation in number of atoms collected in a quadrupole magnetic trap (having field gradient $b \sim 95$ G/cm) with change in the cooling laser frequency detuning (Δ_{CM}) for compressed MOT. 88

5.2 Schematic of the optical pumping method. The solid black lines represent the Zeeman states for the ($5S_{1/2} F = 2$) and ($5P_{3/2} F' = 3$) for ^{87}Rb atom in presence of a bias field. A σ^+ light resonant to ($5S_{1/2} F = 2$) \rightarrow ($5P_{3/2} F' = 3$) excite the transitions (shown by solid red arrow), followed by spontaneous emission (shown by dotted wavy arrow) cycle. Finally, the population from different Zeeman states optically pumped to ($5S_{1/2} |F = 2, m_F = 2\rangle$) state. 89

5.3 (a): The variation in fluorescence from the atom cloud in magnetic trap (proportional to number of atoms) with the power of the optical pumping beam for a duration of $500 \mu\text{s}$ and a bias field of $\sim 2 \text{ G}$.(b): Fluorescence images of cloud of ^{87}Rb atoms trapped in a quadrupole trap for different values of power in optical pumping (OP) beam. 90

5.4 The schematic of the experimental setup. VB: VC-MOT beams, UB: UHV-MOT beams, PB: push beam, VMQC: VC-MOT quadrupole coil, UMQC: UHV-MOT quadrupole coil, RG: Rubidium getters, DPT: differential pumping tube, GC: glass cell, BA: Bayerd-Alpert Gauge, EG: extractor gauge, NEG: non-evaporable getter pump, SIP & NEG: combination pump. 92

5.5 The sequence and durations of various stages from VC-MOT formation to magnetic trapping and detection of ^{87}Rb atoms in the experiments. . . . 93

5.6 The variation in the CCD counts due to fluorescence from atoms trapped in the quadrupole magnetic trap with time for $\sim 13 \text{ A}$ ($b = 95 \text{ G/cm}$) of current in the quadrupole coils. The dotted curve is a guide to the eye. . . 94

5.7 Schematic of the arrangement of the coils for quadrupole magnetic trap and axes of the coordinate system. 96

5.8 The calculated variation in final temperature T_f (figure (a)), final peak density $n'_f(0)$ (figure (b)) and final phase-space density $\rho_f(0)$ (figure (c)) in the quadrupole magnetic trap with field gradient b for the different temperatures and sizes of cloud in molasses. For graphs (i) and (ii) (in figures (b) and (c)), $N' = 2.0 \times 10^7$ and 2.9×10^7 has been used respectively, which are close to the experimentally observed values. 99

5.9 Measured variation in the temperature of atoms in the magnetic trap with the field gradient b . Squares show the temperature measured from the size of the cloud in magnetic trap, and circles show the temperature measured by free expansion method. The cloud temperature and size in the molasses were $T_i = 235 \mu K$ and $\sigma_i = 0.8 mm$ respectively. 100

5.10 Measured variation in peak number density and phase-space density in the magnetic trap with the quadrupole field gradient b , for two sets of temperature and r.m.s size of the cloud in the molasses. The maximum number of atoms in the magnetic trap is $N' = 2.9 \times 10^7$ and 2.0×10^7 for curve (i) and (ii), but N' has varied with the field gradient b . The dashed curves are guide to the eye. 101

5.11 A comparison of experimentally measured values and theoretically estimated values of number density (A) and phase-space density (B). In graph (I) (in (A) and (B)) the data for $T_i = 190 \mu K$ and $\sigma_i = 0.85 mm$ from Fig. 5.10 are replotted here. In graph (II) (in (A) and (B)) the measured values of N' (which are dependent on b) have been used in equation (5.11) and (5.12) to estimate the theoretical values. The dashed curves are guide to the eye. 102

5.12 Magnetic field distribution along Ioffe coil axis. The Inset shows the non-zero offset of the QUIC trap. 103

5.13 (a): The oscilloscope traces showing variation in current in the quadrupole coils and Ioffe coil with time. Absorption images of cloud (i.e. the optical density) trapped in the quadrupole trap and the QUIC trap are also shown. (b): Measured life-time of atoms in the QUIC trap obtained from variation in number of atoms in it with time. 104

5.14 Optical density images obtained from absorption probe images and its profile along the central line of atom cloud after RF evaporation in the QUIC trap. The bimodal distribution observed in the profile (c) is an indication of onset of Bose-Einstein condensation of atoms in the cloud. . 106

5.15 A 3D plot of optical density of the absorption image shown in Fig. 5.14(c) after three-point averaging. Sharp peak in the center depicts the bimodal distribution in the cloud. 107

Chapter 1

Introduction

The field of ultra-cold atoms is rapidly growing and still expanding area of research in physics and has seen a remarkable progress during the last few decades [1, 2]. It has triggered a lot of new developments, which include ultra-precision spectroscopy [3–6], ultra-cold collision physics [7], quantum optics [8, 9], cold molecules [10], matter wave optics [11], ultra-cold plasmas [12] and most importantly Bose-Einstein condensation [13, 14].

Though it was established earlier that light exerts mechanical force on matter, only after the advent of lasers, experiments related to manipulation of external degrees of freedom of atoms (position and momentum) by application of light forces were performed [6]. The earlier demonstrations of laser cooling were the slowing down of sodium atoms in a Zeeman slower [15] and cooling of sodium atoms in a 3D optical molasses [16]. When a quadrupole field is used in conjunction with optical molasses, magneto-optical trap (MOT) was born [17]. Nowadays, due to its simplicity the MOT acts as a work horse for the generation of cold atoms of temperature in the range of few tens to few hundreds micro-kelvin. It has also paved the way for accomplishment of a landmark in the field of atomic physics i.e. Bose-Einstein condensation (BEC) in dilute gases (close to non-interacting systems). It is a phenomena predicted by Einstein, when he extended Bose's predictions for photons [18], to massive non-interacting particles having integral spin (bosons) [19]. He observed that, below a certain temperature the lowest energy state

becomes macroscopically populated [20]. It is a pure quantum mechanical phenomena entirely different from the transition of gases \Rightarrow liquids \Rightarrow solids. BEC was observed in dilute alkali atoms by employing the techniques of laser cooling and magnetic trapping [21–23].

In this chapter, we briefly describe about the concepts used to cool and trap neutral atoms. The forces responsible for cooling of atoms have been discussed first. Subsequently the concept of magneto-optical trap is discussed. This is followed by magnetic trapping, where an outline about the quadrupole and quadrupole-Ioffe configuration trap is presented. Then the evaporative cooling technique, which is used to cool further the laser cooled atom cloud, has been discussed. A brief theoretical description about BEC is also presented. Finally, the applications of cold atoms in various fields have been discussed.

1.1 Fundamentals of laser atom cooling and trapping

Laser cooling is the method to cool the atom down to unexpected low temperature of the order of micro-kelvin which were never possible before using the conventional cryogenic cooling techniques. Prior to the description of the laser cooling technique, it is necessary

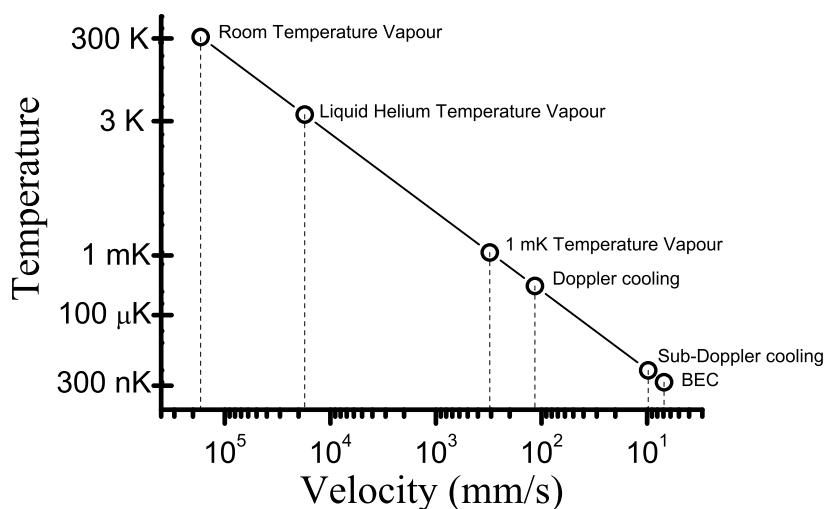


Figure 1.1: A temperature and 1D-velocity scale in the context of laser cooling of Rubidium atom.

to understand the concept of temperature in this context, which is entirely different compared to the thermodynamic temperatures. Here, the temperature describes the spread in velocities in an atomic distribution. Generally, The atoms follow a Maxwell-Boltzmann distribution having an important parameter: the root mean square velocity (v_{rms}), which gives the information about the velocity spread in the distribution. From the kinetic theory of gases in 1D, we can relate the thermal energy $\frac{1}{2}k_B T$ to the v_{rms} as follows,

$$\frac{1}{2}k_B T = \frac{1}{2}mv_{rms}^2, \quad (1.1)$$

where k_B is Boltzmann's constant, T is the temperature and m is the atomic mass. Therefore reducing the v_{rms} , ultimately leads to reduction in the temperature. Fig. 1.1 gives an idea about the changes in velocity and temperature scales, one encounters during the laser cooling of Rubidium atoms. The average velocity of atoms reduces to few mm/s from few hundred $meter/s$.

1.1.1 Laser atom interaction: manipulation of atomic motion

Light can be used as a tool to manipulate and control the external degrees of freedom of an atom, i.e. position and momentum of the atom. This is based on recoil effect resulting from absorption and emission of photons, which changes the momentum of atom. When an atom interacts resonantly with the laser beams, three main processes comes into the picture which are stimulated absorption, spontaneous emission and stimulated emission. These processes give rise to dissipative force when an atom absorbs the photons from a laser beam repeatedly. However, during the non-resonant interaction of atom with laser beam, the conservative force called “dipole force” is exerted on the atom by the laser beam. These two forces have been discussed in the literature in detail by several authors [1, 2, 24–27].

- *Dissipative force*

The dissipative force resulted due to the cycle of unidirectional absorption and spontaneous emission in random direction. By this process, the momentum of

photons get transferred to the atom. This force is also called scattering force or radiation pressure force. The magnitude of the scattering force due to a single beam can be written as,

$$\begin{aligned} \vec{F}_s &= \text{gain in momentum in single cycle} \\ &\quad \times \text{number of fluorescence cycles per second,} \\ \vec{F}_s &= \hbar \vec{k}_L \gamma_{sc}, \end{aligned} \tag{1.2}$$

where \hbar is the reduced Planck's constant, γ_{sc} is the photon scattering rate, $|\vec{k}_L| = 2\pi/\lambda$ is the wave number of the photon of wavelength λ . For a two level atom γ_{sc} is given by,

$$\gamma_{sc} = \frac{\Gamma}{2} \frac{(\Omega^2/2)}{\Delta_L^2 + (\Omega^2/2) + (\Gamma^2/4)} = \frac{\Gamma}{2} \frac{(I/I_s)}{1 + (I/I_s) + (2\Delta_L/\Gamma)^2}. \tag{1.3}$$

Here, Γ is the natural line width and Ω is the Rabi frequency for the transition between the ground and excited state, $\Delta_L = \omega_{DL} - \omega_0$ is the laser detuning from resonance (with ω_{DL} is the angular laser frequency, and ω_0 is the angular atomic resonance frequency), I is the intensity of the laser beam and $I_{sat} (= c\epsilon_0\Gamma^2\hbar^2/4|d_{ge}|^2)$ (d_{ge} is the effective dipole moment) is the saturation intensity. This scattering force can give a maximum deceleration $\sim 10^5g$ (g is the acceleration due to gravity), which clearly shows the potential of the resonant laser light acting on atoms. This force also saturates at high intensity.

- *Reactive force*

The reactive force arises from laser induced dipole moment of atom and its interaction with the laser field. Its magnitude is dependent on the spatial derivative of the intensity profile of the laser beam and the detuning of the laser beam from the atomic resonance. Because of this, this force is called gradient force or dipole force. The magnitude of the dipole force is given as,

$$\vec{F}_d = -\frac{\hbar\Delta_L}{4} \frac{\vec{\nabla}\Omega^2}{\Delta_L^2 + (\Omega^2/2) + (\Gamma^2/4)} = -\frac{\hbar\Delta_L}{4} \frac{\vec{\nabla}(I/I_s)}{1 + (I/I_s) + (2\Delta_L/\Gamma)^2}. \quad (1.4)$$

This dipole force does not saturate with intensity and have a dispersive nature with frequency. For $\Delta_L < 0$ (red-detuning), the force attracts the atoms towards the region of higher intensity, and for $\Delta_L > 0$ (blue-detuning), the force repel the atoms from the region of higher intensity.

These two forces can be used to manipulate the atomic motion. The scattering force which is dissipative in nature, can be made velocity dependent and hence becomes useful for cooling of atoms. The detail is described in subsection 1.1.3. The dipole force is useful for trapping and guiding of cold atoms.

1.1.2 Optical pumping: internal state manipulation

Apart from cooling, which manipulates external states of atoms, light can be used to manipulate internal states of atom. Optical pumping is a process in which the atomic population is transferred to a particular sublevel(s) after multiple cycles of emission and absorption, when atoms interact with incident optical field of a particular polarization. Consider a system where the transition $F = 1/2 \rightarrow F' = 1/2$ can be excited (schematic is depicted in Fig. 1.2). The transitions by σ^+ polarized light obey the selection rule

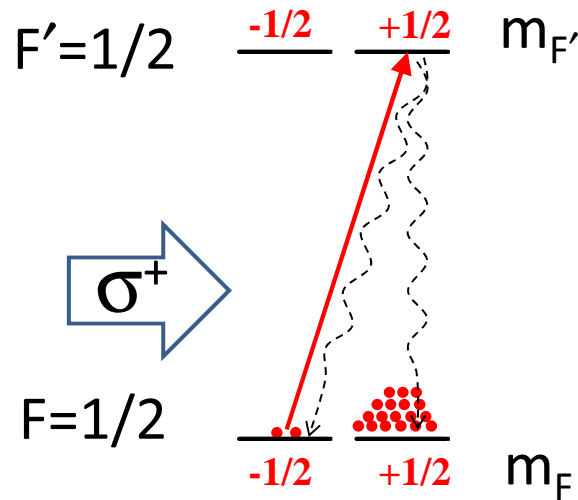


Figure 1.2: Principle of optical pumping for a $F = 1/2 \rightarrow F' = 1/2$ transition.

$\Delta m_F = +1$. Hence, the σ^+ light takes the atomic population from the ground state sublevel $m_F = -1/2$ to the excited state sublevel $m_{F'} = +1/2$, which can decay back to all the two ground state sublevels $m_F = -1/2$, and $m_F = +1/2$. After multiple cycles of excitation and de-excitation the population is transferred to $m_F = +1/2$ sublevel because no transition is possible out of this sublevel. In this case the atomic population is said to be optically pumped to $m_F = +1/2$ sublevel.

1.1.3 Laser Doppler cooling mechanism

The scattering force of laser beam on atom can be utilized to reduce the speed of the atoms. The Doppler cooling is one such mechanism which exploits the Doppler effect to generate the cooling effect of laser beam on an atom. An atom under motion with a particular velocity can be in the resonance with the oppositely propagating laser beam when the Doppler shifted frequency of laser beam experienced by the atom equals the atomic transition frequency. As a result, the laser beam can exert a net force on the atom which can reduce its velocity. Such scattering force is detuning dependent (equation (1.2)) and is velocity dependent as well. Exploiting this, T.W. Hänsch and A.L. Schawlow [28] have proposed using three pairs of counter-propagating red-detuned beams to cool atoms.

The net force on the atom in presence of two counter-propagating laser beams is given as [29],

$$F_{sz} = \hbar k_L \frac{\Gamma}{2} \left[\frac{(I/I_s)}{1 + (I/I_s) + (2(\Delta_L - k_L v)/\Gamma)^2} \right] - \hbar k_L \frac{\Gamma}{2} \left[\frac{(I/I_s)}{1 + (I/I_s) + (2(\Delta_L + k_L v)/\Gamma)^2} \right], \quad (1.5)$$

where Δ_L is modified to $\Delta_L \pm k_L v$ to account for Doppler shift. In the limit of small velocity $k_L v \ll \Gamma$, F_{sz} can be approximated by:

$$F_{sz} \approx -\alpha v = -4\hbar k_L^2 \frac{I}{I_s} \frac{2\Delta_L/\Gamma}{[1 + (I/I_s) + (2\Delta_L/\Gamma)^2]^2} v. \quad (1.6)$$

With red-detuned light, $\alpha > 0$, the atom will see a damping or cooling force as that

of a particle in a viscous medium. That is why this arrangement of a pair of counter-propagating red-detuned laser beams is known as one-dimensional optical molasses for an atom.

1.1.4 Optical molasses

Chu et al. [16] have first time experimentally realized cooling of atoms in three-dimension by generalizing the above Doppler cooling mechanism. For this, three orthogonal pair of counter-propagating laser beams derived from same laser and having a frequency slightly lower than the transition frequency were used. In the intersection region of the laser beams in this geometry, a moving atom always experiences an opposition due to the scattering force from the counter-propagating laser beam. It results in a damping in the motion of the atom. Due to its similarity with the motion of a particle in a viscous medium, “Optical molasses” term was coined.

1.1.5 Magneto-optical trap

Though the cooling of atoms in optical molasses helps in reducing the kinetic energy, it lacks to provide any spatial confinement. Due to lack of trapping or confinement, the atom may diffuse out of the overlapping region with time. Also, the effectiveness of cooling in molasses depends upon the detuning which becomes larger with cooling of atoms. After cooling, an atom may reach to a velocity range where the Doppler shift no longer brings the atom to the resonance and hence the cooling ceases. To circumvent these problems Dalibard suggested to introduce an inhomogeneous magnetic field which introduces a position dependent scattering force. Raab et al. [17] first demonstrated a magneto-optical trap (MOT) in a beam of atoms by the inclusion of such magnetic field (created by quadrupole coils) to generate this position dependent force. Later on Monroe et al. [30] have directly loaded the MOT in a vapor cell. Due to the simplicity and robustness of MOT, it has become a widely used source of cold atoms.

In the MOT, three pairs ($\sigma^+ - \sigma^-$) of laser beams are used. A spherical quadrupole field is superimposed in such a way that its center matches with the intersection point of

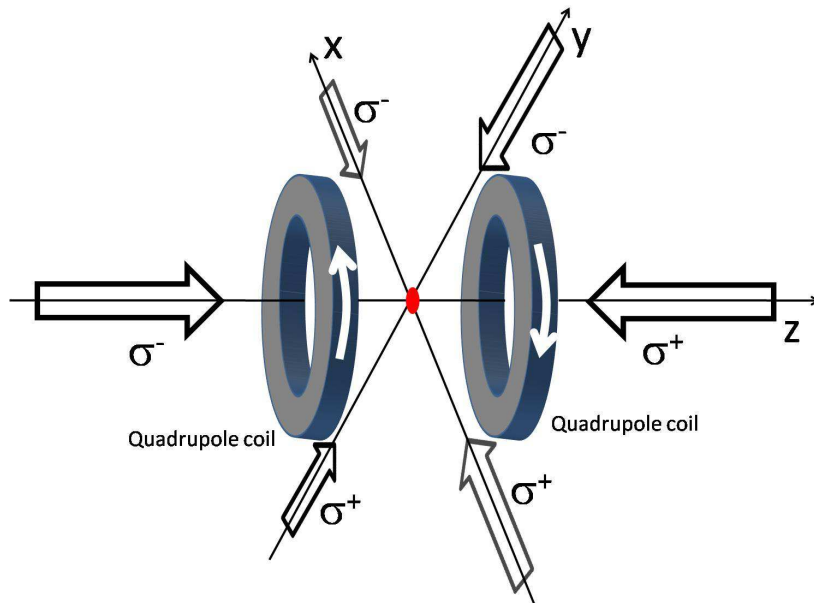


Figure 1.3: Configuration of a MOT used in our experiments. In the MOT, three pairs of $(\sigma^+ - \sigma^-)$ laser beams of equal intensity and frequency are used. The magnetic field gradient is generated by a pair of coils placed in quadrupole configuration (the white arrows depicts the current direction in the coils).

the beams. For an appropriate combination of magnetic field and laser beam polarization, an atom moving away from the center will experience a force directing it towards the center of the trap. The standard MOT configuration is shown in Fig. 1.3. In the low intensity limit, the total force on an atom placed in between two counter-propagating beams in presence of magnetic field gradient is given by,

$$F_{sz} = \hbar k_L \frac{\Gamma}{2} \left[\frac{(I/I_s)}{1 + (I/I_s) + (2(\Delta_L - k_L v + \mu' B_z/\hbar)/\Gamma)^2} \right] - \hbar k_L \frac{\Gamma}{2} \left[\frac{(I/I_s)}{1 + (I/I_s) + (2(\Delta_L + k_L v - \mu' B_z/\hbar)/\Gamma)^2} \right], \quad (1.7)$$

where $\mu' = (g_e m_e - g_j m_j) \mu_B B_z$ is the effective magnetic moment for the transition, in which g_e and g_j are Landé g factor for excited state and ground state respectively, μ_B is the Bohr magneton and $B_z (= bz = \frac{dB}{dz} z)$ is the magnetic field in the z direction due to spherical quadrupole trap. For Doppler shift and Zeeman shift values less than detuning Δ_L , the equation (1.7) can be approximated as,

$$F_{sz} \approx -\alpha v - \kappa z \quad \text{with} \quad \kappa = \frac{\mu' b}{\hbar k_L} \alpha. \quad (1.8)$$

In the force experienced by the atom, in addition to the velocity dependent part a position dependent part arises due to Zeeman shift contribution. Hence, the force not only damps the motion of the atom but also confines the atom spatially.

MOT provides a trap capable of accumulating large number of atoms, but the temperature and density that can be achieved is limited due to a number of reasons [31–34]. To increase the density a very convenient stage is compressed MOT (CMOT) [35], performed by increasing the detuning of the cooling laser and increasing the field gradient used for MOT. As a result, the radiation pressure reduces which increases the density of atoms in MOT. Further, to lower the temperature of atoms in MOT, the magnetic field is turned off to leave the atoms in optical molasses, where sub-Doppler cooling mechanisms can take place. To further lower the temperature achieved by MOT, CMOT and optical molasses stages, another cooling stage “evaporative cooling” is necessary. The evaporative cooling can be performed in a trap where the atoms can be stored for a longer time (discussed in section 1.3).

1.1.6 A Magneto-optical trap for Rb atoms

In our setup we have performed laser cooling of ^{87}Rb atoms. The circularly polarized laser beams are $\sim 2\pi \times 15$ MHz detuned from the $(5S_{1/2} F = 2) \rightarrow (5P_{3/2} F' = 3)$ transition. To sustain the cooling process, normally another laser known as repumping laser (resonant to $(5S_{1/2} F = 1) \rightarrow (5P_{3/2} F' = 2)$) is mixed with the cooling beam. The reason is, during the cooling transition (having scattering rate $\sim 6 \times 10^7$ photons/s) the atom has a finite probability of making an off-resonant transition $(5S_{1/2} F = 2) \rightarrow (5P_{3/2} F' = 2)$ (having scattering rate $\sim 3 \times 10^4$ photons/s). From these two probabilities, it is clear that for roughly 200 cooling transitions there may be one off-resonant transition will take place, and there is 50 % probability of decaying of the atom from $(5P_{3/2} F' = 2)$ to $(5S_{1/2} F = 1)$ state. As a result, the atom pumped to $(5S_{1/2} F = 1)$ will no longer participate in the cooling cycle. Therefore, to bring the atom back to participate in the

cooling cycle, another laser resonant to $(5S_{1/2} F = 1) \rightarrow (5P_{3/2} F' = 2)$ is used.

1.1.7 Doppler cooling limit

Due to the stochastic nature of photon absorption and emission the scattering force produces a momentum diffusion/heating of the atoms. The balance of the cooling and heating rates result in a lower limit to the final temperature attainable through Doppler cooling alone. For beams with low intensity, this minimum temperature known as the Doppler limit is $T_D = \hbar\Gamma/2k_B$. For Rb atom this value is $140 \mu K$.

1.1.8 Sub-Doppler Cooling

After the successful demonstration of optical molasses [16], a precise measurement of temperature in molasses [36] established that, temperature below than Doppler limit can be achieved. As the Doppler cooling theory was unable to explain this behavior, it was necessary to invoke a sub-Doppler cooling mechanism. The sub-Doppler cooling mechanism has considered the following facts:

- Multi-level structure of the atom results in a variable light shift of different levels,
- Spatial polarization gradient formed due to superposition of counter-propagating laser beams and
- optical pumping of atoms in to other states.

Taking these features into account, a polarization gradient cooling mechanism “Sisyphus cooling” (for orthogonal linear polarization: $\text{lin}\perp\text{lin}$) and “motion-induced orientation cooling” (for orthogonal circular polarization: $\sigma^+ - \sigma^-$) were studied. A detailed description of these methods can be found in [37, 38].

The damping produced by these sub-Doppler cooling mechanisms is much stronger as compared to the Doppler cooling mechanism. Momentum recoil by a single photon puts a limit to this cooling mechanism. The recoil temperature which is lowest attainable is given as $T_R = \hbar^2 k_L^2 / mk_B$. For Rb atom this value is $362 nK$. But this value of

temperature is usually not achievable in the laser cooling process due to the destructive effects of multiple scattering (i.e. re-absorption of spontaneously emitted photons).

1.2 Magnetic trapping of atoms

Trapping of atoms played a very crucial role in reaching to the high phase space density regime needed for BEC. Different types of traps based on interaction of atoms with the external field (magnetic [39, 40], optical [41], or a hybrid of magnetic and optical [42]) were proposed and demonstrated. The trap, we have used is a magnetic trap, which is based on interaction of the magnetic dipole moment of the atom ($\vec{\mu}$) and the external magnetic field (\vec{B}). The potential energy experienced by the atom is given as,

$$U = -\vec{\mu} \cdot \vec{B} = g_F m_F \mu_B |B|. \quad (1.9)$$

where g_F is the Landé g factor and m_F is the Zeeman sublevel of the hyperfine level F . The force on the atom F_{mag} ($= g_F m_F \mu_B \nabla |B|$) pushes the atoms with $g_F m_F > 0$ ($g_F m_F < 0$) towards low field (high field) and are known as low-field seeking state (high-field seeking state) (As shown in Fig. 1.4). As creation of a local maximum of magnetic field in free space is not possible, the low field seeker states are the only trappable states. Several groups worldwide have used different types of designs for magnetic traps for neutral atoms [43]. These include,

- (i). Quadrupole trap
 - (ii). Ioffe-Pritchard trap
 - (iii). Cloverleaf trap
 - (iv). Base-ball trap
 - (v). Quadrupole- Ioffe configuration (QUIC) trap
- etc.

For ^{87}Rb atoms there exist three trappable states e.g. $5S_{1/2} |F = 2, m_F = 2\rangle$, $5S_{1/2} |F = 2, m_F = 1\rangle$ and $5S_{1/2} |F = 1, m_F = -1\rangle$. We have used the $5S_{1/2} |F = 2, m_F = 2\rangle$ state for magnetic trapping as it can provide stronger confinement to the atoms as compared to the other two states, for the same strength of field.

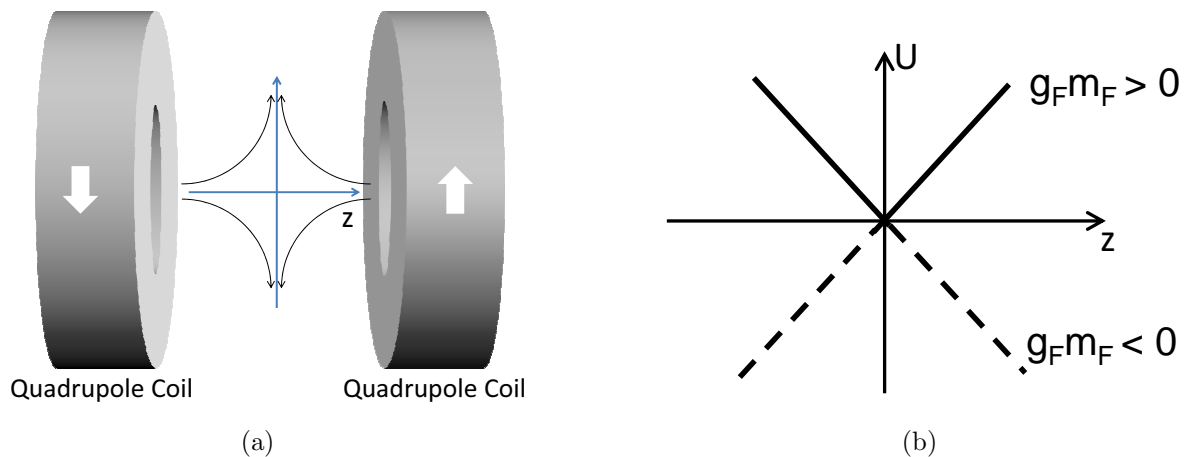


Figure 1.4: (a): Quadrupole trap formed by two identical coils carrying current in opposite directions (shown by arrow). (b): Variation in magnetic trap potential with position. The solid line and dashed line show the potential experienced by the low field seeking and high field seeking states respectively.

1.2.1 Quadrupole trap

As discussed above, low field seeking states can be trapped in a local minima of an inhomogeneous field. A very simple configuration to trap atoms is the quadrupole field generated by a pair of coils by flowing current in opposite direction. At the center of the trap the quadrupole field is approximately given as [43],

$$\vec{B} = b \left[\frac{x}{2}, \frac{y}{2}, -z \right], \quad (1.10)$$

where b is the field gradient along the axial direction (z). The quadrupole trap generates a potential of V shape with a minimum (zero) at the center (as shown in Fig. 1.4). The main problem with the quadrupole trap is the zero field at the center where atoms may make a spin flip (Majorana flip) and go to untrappable state and hence may be lost from the trap [40]. For this reason the quadrupole trap is not suitable for evaporative

cooling which requires a longer life-time of the trap. For evaporative cooling purpose, various techniques are employed to eliminate the Majorana spin flip losses. These include “plug the hole” [23], “Time orbiting potential (TOP) trap” [21, 40], “the Ioffe-Pritchard trap” [44, 45], “the cloverleaf trap” [46], “the Base ball trap” [47], “quadrupole-Ioffe configuration (QUIC) trap” [48] etc.. Among the various geometries, the QUIC trap is simpler and operates at a lower current. We adapted the QUIC trap for evaporative cooling of ^{87}Rb atoms during this thesis work.

1.2.2 Quadrupole-Ioffe configuration trap (QUIC trap)

A QUIC trap consists of two identical quadrupole coils and one Ioffe coil which is conical at one end (Schematic is shown in Fig. 1.5). This trap is quadrupole trap when there is no current in Ioffe coil. If the current through the Ioffe coil is increased, the magnetic field along the axis of Ioffe coil (and hence trapping potential) starts deforming and finally gives a quadratic field distribution with non-zero off-set field (Fig. 1.5). This is known as Ioffe configuration for the QUIC trap. The non-zero off-set field suppresses the Majorana spin flip losses. The QUIC trap operates at a lower current as compared to the other traps (e.g. Ioffe-Pritchard trap) which is easier to handle.

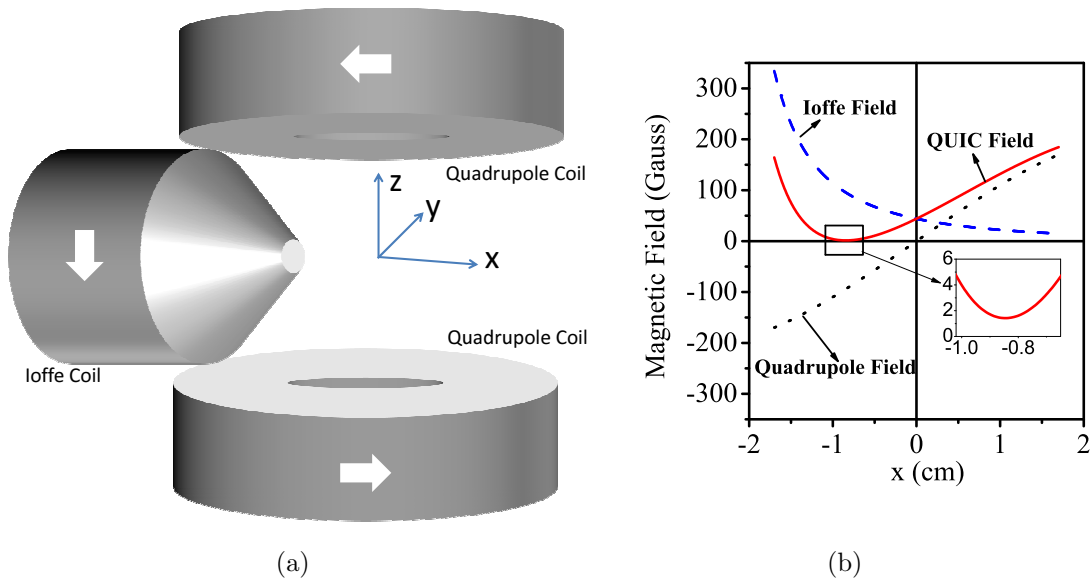


Figure 1.5: (a):Schematic of the QUIC trap (formed by three coils: two quadrupole coils and an Ioffe coil; current direction in the coils are shown by arrow).(b): Magnetic field distribution along the Ioffe coil axis.

The magnetic field of the QUIC trap near the non-zero off-set field can be approximately given as [49–51],

$$B(x, y, z) = B_0 + \frac{1}{2}B''x^2 + \frac{1}{2}\frac{B'^2}{B_0}(y^2 + z^2), \quad (1.11)$$

where B_0 is the magnetic off-set field, B' is the radial field gradient, B'' is the curvature along the x-direction (Ioffe coil axis). The resulting potential due to the field given as,

$$U(x, y, z) = g_F m_F \mu_B B(x, y, z) = U_0 + \frac{1}{2}m\omega_x^2 x^2 + \frac{1}{2}m\omega_\rho(y^2 + z^2), \quad (1.12)$$

where m is the mass of the atom, U_0 ($= g_F m_F \mu_B B_0$) is the minima of the trapping potential, ω_x ($= \sqrt{g_F m_F \mu_B B''/m}$) and ω_ρ ($= \sqrt{g_F m_F \mu_B B'^2/mB_0}$) are the angular axial and angular radial trap frequencies respectively.

1.3 Evaporative cooling

Evaporative cooling is a method to reach the temperature below the temperature regimes achievable by laser cooling technique. The idea of evaporative cooling was introduced by Hess for Hydrogen [52]. But this technique proved to be very useful in alkali atoms to reach the quantum degeneracy [21]. In magnetic traps it is implemented by using radio-frequency (RF) radiations [53]. The principle is as follows: the atoms with higher energy are selectively removed from the trap by applying the RF radiation. The RF radiation makes the atoms flip the spin and pumped to an untrappable state and hence, leave the trap. As a result, rest of the atoms in the trap thermalize to a lower temperature by elastic collision.

1.4 Bose-Einstein condensation (BEC)

All the particles in nature are either ‘bosons’ (having integer spin) or ‘fermions’ (having half integral spin). The wave function describing the system of bosons remains symmetric

under interchange of any two particles, whereas the fermions show an anti-symmetric behavior in the similar case. Another important property of bosons is that, any number of bosons can occupy the same available state. But fermions do not obey this statistics and a single fermion can be accommodated in a given state. Bosons follow Bose-Einstein statistics and show a special behavior of macroscopic accumulation in the lowest energy state below a certain temperature, known as Bose-Einstein condensation (BEC). The temperature below which which BEC occurs is known as critical temperature. The value of the critical temperature T_c for N number of atoms in a cubic box with volume V can be evaluated as,

$$k_B T_c = \left(\frac{h^2}{2\pi m} \right) \left(\frac{N/V}{\zeta(3/2)} \right)^{2/3}. \quad (1.13)$$

where $\zeta(x)$ is the Riemann zeta function and $\zeta(3/2) \approx 2.612$. It is important to note here that T_c is the temperature at which the thermal deBroglie wavelength $\lambda_{dB} (\equiv h/\sqrt{2\pi m k_B T})$ is of the same order of magnitude as the average interparticle separation. The equation (1.13) can be rearranged in terms of phase space density (ρ) as,

$$\rho = n \lambda_{dB}^3 \approx 2.612, \quad (1.14)$$

where $n (\equiv N/V)$ is the density of the gas. At temperature lower than T_c , the condensate fraction (N_0) can be calculated as,

$$\frac{N_0}{N} = 1 - \left(\frac{T}{T_c} \right)^{3/2}. \quad (1.15)$$

The above expressions are for ideal gas in a box, but the BEC achieved in dilute gases is in spatially varying potentials. When atoms are confined in a spatially varying potential the critical temperature is significantly altered. Another important feature of traps with spatially varying potentials is the inhomogeneous density distribution of the Bose gases which can be tailored by tailoring the potential shape. This provides further opportunity to trap bosons and study the Bosonic degeneracy in lower or fractional dimensions. In a

3D harmonic trap, the confining potentials is given as,

$$V(r) = \frac{1}{2}m(\omega_x^2 + \omega_y^2 + \omega_z^2)r^2, \quad (1.16)$$

where the ω_i are the trapping frequencies. Bagnato et al. [54] have extended Einstein's theory of BEC in a box to the gas trapped in a harmonic potential. Due to the inhomogeneity of the trap, the density of states get modified and results in a change in the critical temperature and condensate fraction. The T_c for a gas trapped in a potential of the form (1.16) is given by [1, 14],

$$k_B T_c = \frac{\hbar \bar{\omega} N^{1/3}}{[\zeta(3)]^{1/3}} \approx 0.94 \hbar \bar{\omega} N^{1/3}, \quad (1.17)$$

where $\bar{\omega} (= (\omega_x \omega_y \omega_z)^{1/3})$ is the geometric mean of the trapping frequencies. For the same trapping potential, the condensate fraction at temperature T is given as ,

$$\frac{N_0}{N} = 1 - \left(\frac{T}{T_c} \right)^3. \quad (1.18)$$

In the above evaluation of critical temperature and condensate fraction, the case of ideal gas (non-interacting nature) is considered. But in the real condensates, in the regime of high density, the gases show an interacting nature and modify the behavior of condensate significantly [14, 55]. The density of the atoms in the ground state of an harmonic oscillator has a Gaussian spatial profile, whereas the interactions result a different profile which is a inverted parabolic profile (under Thomas-Fermi approximation) given by,

$$n = n_0 \max \left(1 - \frac{x^2}{r_x^2} - \frac{y^2}{r_y^2} - \frac{z^2}{r_z^2}, 0 \right), \quad (1.19)$$

where $n_0 (= \frac{15}{8\pi} \frac{N}{r_x r_y r_z})$ is the peak condensate density, $r_i = \sqrt{2\mu/m\omega_i^2}$ is the width of the condensate. The chemical potential (μ) is given by,

$$\mu = \frac{\hbar \bar{\omega}}{2} \left(\frac{15 N_0 a_s}{\bar{a}} \right)^2 / 5, \quad (1.20)$$

where a_s is the s-wave scattering length and $\bar{a} = \sqrt{\hbar/m\bar{\omega}}$ is the mean harmonic oscillator length of the trapping potential.

1.5 Applications of cold atoms

The cooling of atoms has provided a great deal of control and manipulation of atoms which proving to be useful for various applications in basic research as well as in state-of-art technolgy devices for precision measurements and other applications. The basic research with cold atoms have seen amazingly new developments in ultra-precision spectroscopy, ultra-cold collisions, quatum optics, cold molecules, matter waves and Bose-Einstein condensation[13]. Experimental realization of BEC is perhaps the landmark achievement in this field. The use of Bose condensates provides unique opportunity to re-explore various interesting physics problems like superfluidity, quantum phase transition, Joesephson junction, quantum vortices etc.

The applications of cold atoms in state-of-art devices are equally fascinating which include precision atomic clocks, ultra-precise accelerometer, sensitive atom gyroscope, gravity gradiometer, atom lithography and quantum information processing [3–6, 8, 56]. Though, presently the cold atom setups are bulky and not handy for transportation. However, the research and developments are taking shape to miniaturize the cooling and trapping setups using “atom-chip” techniques [57–59].

Chapter 2

Experimental Apparatus

2.1 Introduction

In this chapter, a brief description of experimental apparatus used in the studies in this thesis is presented. The apparatus consists of several frequency stabilized laser systems, ultrahigh vacuum (UHV) chambers, a double magneto-optical trap (double-MOT) setup for ^{87}Rb atoms, magnetic traps for cold atoms, RF evaporative cooling systems, detection and characterization equipments, and a PC-based controller system to implement various cooling stages in a desired sequence. The double-MOT setup [60] is very convenient to implement the two stage cooling of atoms, which are laser cooling (first stage) and evaporative cooling (second stage) respectively. The laser cooling stage results typically the temperature of cold atoms in the range 50 - 500 μK , whereas the evaporative cooling can result the temperature in the range of sub-micro-Kelvin to few micro-Kelvin. The double-MOT setup developed in-house by us to generate samples of cold ^{87}Rb atoms is also based on similar scheme, where laser cooling of ^{87}Rb atoms in the magneto-optical traps (MOTs) provides the first stage of cooling and evaporative cooling of these laser cooled samples in a magnetic trap leads to the second stage of cooling. Our double-MOT setup consists of two separate chambers at different pressures maintained by a differential pumping tube. One of the chamber is at a pressure $\sim 1 \times 10^{-8}$ Torr (with Rb-vapor) where the first MOT of ^{87}Rb atoms is formed by collecting the atoms from

the background Rb-vapor in this chamber. This MOT is known as vapor chamber MOT (VC-MOT). The second MOT is formed in a different chamber kept at an ultra-high vacuum (UHV) ($\sim 6 \times 10^{-11}$ Torr) environment. The second MOT is known as UHV-MOT (it is also referred as science-MOT by several groups in the world), for which the Rb atoms are provided by transferring atoms from the VC-MOT. The atoms collected in the UHV-MOT are used for magnetic trapping and evaporative cooling to generate atomic samples having further lower temperature. The UHV environment in the chamber is suitable for the long life-time of atoms in the magnetic trap which is necessary for the evaporative cooling process due to its slow nature.

The different components and systems used in the experimental apparatus are briefly discussed in the following sections. However, to keep the discussion not too lengthy, we have not presented the detailed discussion about the various other components used in the experiments such as different optical components (mirrors, retardation plates, polarizing beam splitters, beam expanders, optical isolators, Acousto-optic modulators (AOMs)), opto-mechanical components, power supplies, magnetic coils, detectors and CCD cameras etc. Similarly, the complexities associated with the operation of several electronics components and execution of various processes with precise timing and appropriate sequence have also not been discussed fully.

2.2 Vacuum system of the experimental setup

The vacuum system is a very important part of the double-MOT setup. The vacuum system consists of various stainless steel (SS) components including chambers, conflat flanges, nipples, four-way cross, tees, gate valves, etc. It also consists of several glass view-ports, quartz glass cell, electrical feed-throughs for connecting Rb-getters, and several pumps. The pumps used in our setup include turbo-molecular pump (TMP), sputter-ion pumps (SIPs) and Non-Evaporable Getter (NEG) pumps. The components such as chambers, conflat flanges, nipples, four-way cross, tees etc were fabricated in-house. A special care was taken to protect the knife-edges, as these are crucial for achieving

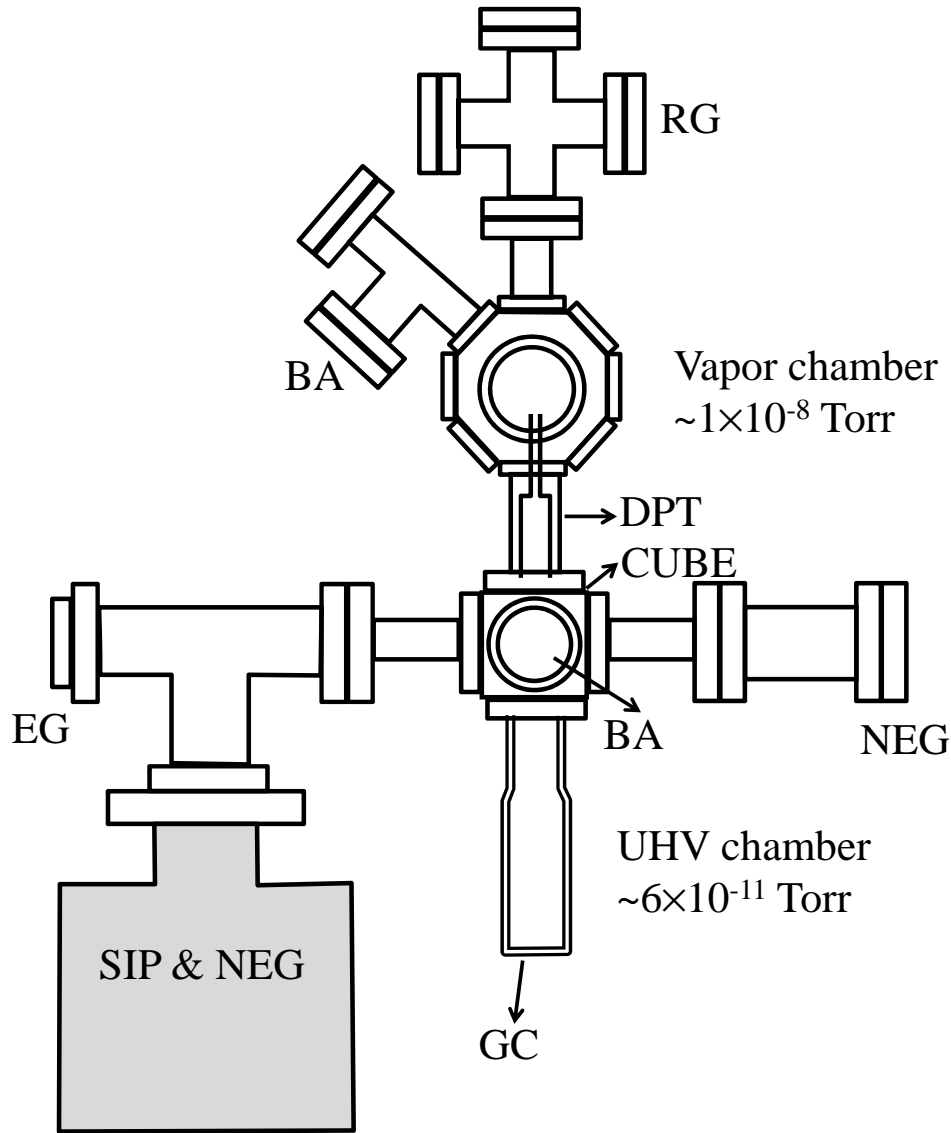


Figure 2.1: Schematic of the vacuum system. RG: Rubidium getters, DPT: differential pumping tube, GC: glass cell, BA: Bayerd-Alpert Gauge, EG: extractor gauge, NEG: non-evaporable getter pump, SIP & NEG: combination pump of sputter ion pump and NEG module. A sputter-ion pump of capacity 20 l/s and a turbo molecular pump of capacity 70 l/s in conjunction with a NW63CF pneumatic gate valve is connected to the upper part of the chamber (not shown).

vacuum. The in-house fabricated components were chemically cleaned in an in-house facility, where ultrasonic cleaning in organic solvent and alkali cleaning were carried out before assembling into the final setup. The other components like viewports, quartz glass cell, gate valves, and pumps were procured from the commercial suppliers. The schematic and a photograph of the setup is shown in Fig. 2.1 and Fig. 2.2 respectively. The main parts of the vacuum system are as follows.

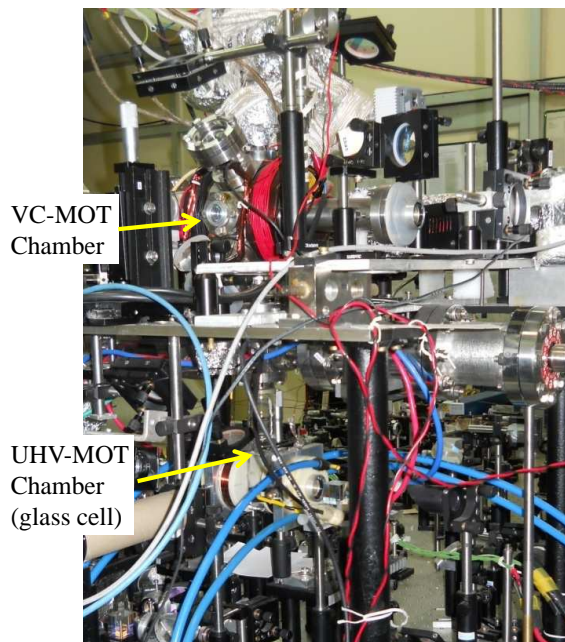


Figure 2.2: Image of the vacuum system.

2.2.1 Vacuum chamber for VC-MOT

In our setup, the chamber for VC-MOT (also referred as VC-MOT chamber) is an octagonal hollow SS chamber which is kept at low pressure ($\sim 10^{-8}$ Torr with Rb-vapor). This chamber has eight faces having knife-edges of size NW25CF and two faces having knife-edges of size NW63CF (Fig. 2.1). A 70 l/s capacity turbo molecular pump (TMP) (*Turbo-V70LP, Varian*) is connected to this chamber via a pneumatic gate valve (*Filinger Gate valve 63CF*) to provide the initial roughing to the whole vacuum system. A SIP of capacity 20 l/s (*VacIon 20 l/s Starcell*) is also connected to this chamber via a right angle metal gate valve. The gate valve can be adjusted to control the effective pumping speed of SIP for the vapor chamber. A Bayerd-Alpert gauge (sealed type) (BOC Edward make) was also connected to the octagonal chamber to monitor the pressure in the VC-MOT chamber. The Rb-vapor is injected in this chamber by heating the Rb-getters which are inserted in the chamber by using the electrical feedthroughs.

2.2.2 Vacuum chamber for UHV-MOT

In our setup, the UHV-MOT is formed inside a quartz glass cell (also referred as UHV-MOT chamber) which is kept at very low pressure (10^{-10} to 10^{-11} Torr). This glass cell

(*Optiglass UK*) is mounted on a rotatable NW35CF size SS flange using a glass to metal seal. This end of the cell is connected to a six-way hollow cube. The sides of this cube have appropriate knife-edges to connect CF flanges of size NW35CF (Fig. 2.1). This way cube is also utilized to connect the VC-MOT chamber to the glass cell. The upper side of the cube is connected to the chamber for VC-MOT through the differential pumping tube (DPT), whereas lower side of the cube is connected to the glass cell. The other sides of the cube are utilized to connect a combination pump (*VacIon plus, 150 l/s Starcell and a NEG module, Varian*) and an independent NEG pump (*GP-100MK5, SORB-AC MK5 type cartridge pump from SAES getters, Italy*). These pumps provide the desired UHV pressure in the cube and glass cell, while keeping the VC-MOT chamber at higher pressure due to DPT. The pressure in this UHV chamber is monitored through current in SIP of combination pump as well as by using an extractor type gauge (*Oerlikon leybold*) connected to pumping line of the cube.

2.2.3 Design considerations for the differential pumping

The differential pumping tube (DPT) is a very crucial part of the vacuum system, which maintains the pressure difference between the VC-MOT chamber and the UHV-MOT chamber. The conductance (in litres/sec) of this tube of length L (in cm) and diameter D (in cm) is given as [61]:

$$C = 12.4D^3/L, \quad (2.1)$$

The above expression for conductance holds good for Nitrogen gas and it gives an over-estimate of the conductance for Rubidium vapor.

If the two chambers are at pressure P_1 and P_2 , and connected using the tube of conductance C (as depicted in Fig. 2.3), then, the throughput to the second chamber is $(P_1 - P_2)C$ Torr l/s. If a pump with pumping speed S l/s connected to the second chamber at pressure P_2 , then the throughput taken into the pump will be P_2S Torr l/s. These two throughput values should be equal under equilibrium. Thus one gets,

$$C(P_1 - P_2) = SP_2,$$

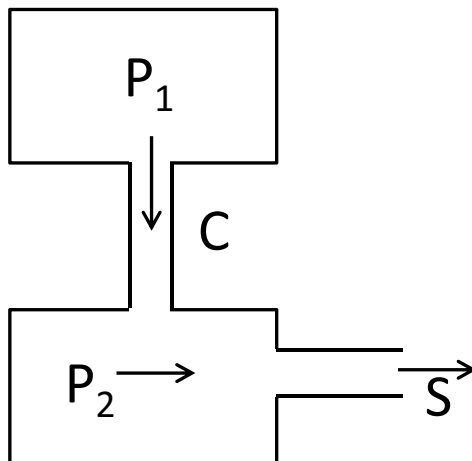


Figure 2.3: Two chambers at pressure P_1 and P_2 are connected using a tube of conductance C and a pump of pumping speed S .

$$C = \frac{P_2 S}{(P_1 - P_2)} \approx \frac{P_2}{P_1} S, \quad \text{for } P_1 \gg P_2. \quad (2.2)$$

One can aim to keep C of DPT as low as possible to get the P_1/P_2 as high as possible. But, the main constraint in choosing the size (diameter and length) of DPT comes from the consideration of transverse expansion of atom flux during the transfer of cold atoms from VC-MOT to UHV-MOT to load the UHV-MOT. Initially we had used a tapered DPT of conical shape with inner diameters of 5.0 mm (towards VC-MOT chamber) which gradually increased to 12.0 mm at the other end (towards the UHV-MOT chamber) over a length of 80 mm. The tapered design of the tube was chosen to accommodate the expansion of atom flux during the atom transfer from VC-MOT to UHV-MOT. With this tube, we obtained the $P_1 = 1 \times 10^{-8}$ Torr and $P_2 = 1.2 \times 10^{-9}$ which are consistent with value of C of DPT ($C \sim S/100$ l/s) and effective pumping speed S of the pumps. Using this design, we performed some experiments to study atom transfer between two MOTs [62]. But the value of P_2 obtained in UHV-MOT chamber with this tube was not low enough to get sufficiently long life-time of atoms in the magnetic trap in this chamber. Hence a modification in the design of DPT was required. As the work progressed, we had tried few other designs [63, 64]. But finally, we selected a narrow tube of length 122 mm. The upper part (VC-MOT side) of this tube has inner diameter of 2.25 mm upto 60 mm length, whereas the remaining part of the tube has inner diameter of 5 mm. With this tube and with appropriate operation of pumps as well as de-gasing

of chambers (via prolonged baking), we could achieve the P_1 and P_2 in the chambers as 1×10^{-8} Torr and 6×10^{-11} Torr respectively. These pressure values were suitable for magnetic trapping and evaporative cooling experiments. At the same time, the atom transfer from VC-MOT to UHV-MOT could also be achieved with this design of DPT without much difficulty when a red-detuned push beam was focused on VC-MOT. This is because the DPT provided a clear passage to the diverging push laser beam as well as to the expanding atom flux through it.

2.2.4 Getters as a source of Rubidium vapor

We have used Rubidium getters (*Rb/NF/3.4/12 FT10+10, SAES Getters*) for the generation of Rb vapor inside the VC-MOT chamber. These getters were welded on the pins of an UHV feedthrough which is inserted in the tee connected to VC-MOT chamber. Two such set of getters were fixed on each arm of this tee, so that on exhaust of one set, the other set can be used without breaking the vacuum. As the material of the feedthrough is copper on which the getters cannot be directly mounted, we first brazed SS strips on the two ends of the copper feedthrough (which were to be kept towards vacuum) and then the getters (3 Nos) were spot welded on it in series. When a DC current was supplied to the getters via the feedthrough, the Rb vapor was generated due to heating of the getter strip. To supply a DC current to the getters, we have used a DC regulated power supply (*Testronix 0-15V/0-10A*). We supplied a current of 2.5 A to 4 A depending upon the requirement of vapor pressure in the VC-MOT chamber.

2.2.5 Procedure followed to achieve the desired vacuum

Our experimental setup is a double-MOT system, that has two pressure regimes. The pressure in the chamber for VC-MOT and UHV-MOT should be in the range of $\sim 10^{-8}$ Torr and $\sim 10^{-11}$ Torr respectively. A systematic approach for pumping and baking stages were adopted to achieve these desired pressures in both the chambers. After assembling the whole system, the turbo molecular pump (TMP) system of capacity 70 l/s was switched-ON, which was connected to the VC-MOT chamber. Our TMP system

uses a dry-scroll pump as a roughing pump. This type of pumps are clean pumps which do not have any oil and hence there is no chance of oil contamination in the vacuum chamber. The TMP was operated for 24 hours, so that most of the gases could be pumped out. The pressure after 24 hour operation was typically 10^{-7} Torr. To go below 10^{-7} Torr, baking of the whole system was necessary. As our system contains SS part, glass view-ports, glass cell, which have different bakable temperatures, we preferred a uniform heating of whole system at a low temperature ($\sim 200^{\circ}\text{C}$) for a prolonged duration of about one week.

For bakeout operation, the whole system was wrapped initially with Aluminium foils and then with heating tapes. Aluminium foil helps in distributing the heat from the heaters as well as protecting the surface from burnt marks. To heat the glass cell, we have used a heater of hot-blower type. Special care has been taken during wrapping, such that overlapping of the heating tape should not take place and an uniform heating of all the parts can be performed. The SIP connected to the UHV chamber (glass cell) (*VacIon plus 150 l/s*) has an inbuilt heater, whereas the SIP connected to the VC-MOT chamber (*VacIon 20 l/s*) does not have any inbuilt heating mechanism. Therefore, we have wrapped a heater tape on this SIP externally for the baking of this pump. The current in the heaters were controlled by variable transformers (VARIACs), which in turn controls the temperature during baking. We have gradually increased the temperature to $\sim 200^{\circ}\text{C}$. The SIP heater was also operated during bakeout operation for the degassing of its inner surfaces. The temperature at various points were measured using thermocouples attached at several points on the chamber. After baking the system for approximately six days at 200°C , we started degassing of different components viz. vacuum gauges, Rb getters. The degassing was done to remove the contaminants over the surface of the components. After that, we started reducing the temperature. When the temperature $\sim 150^{\circ}\text{C}$, we activated the NEG pumps by supplying the required current for a specific duration through them. The SIPs were turned on intermittently (switched-ON for 2 minutes and then switched-OFF several times). This helps in removing the contaminants from the inner surface of SIPs. To activate the Rb-getters, we have flown a current 6 A

to 8 A for 4 to 5 seconds several times in the interval of 1 minutes. This was done to break the outer layer over the getters and hence Rb vapors can be finally obtained at the operatable current (2.5 A to 4 A). Then the chamber was allowed to cool gradually by reducing the temperature, and finally the gate valve which isolates the vacuum chamber from the TMP was closed. After 48 hours of this bakeout procedure, we have obtained a pressure of $\sim 4 \times 10^{-9}$ Torr in the VC-MOT chamber and $\sim 5 \times 10^{-11}$ Torr in the UHV-MOT chamber. These pressures were measured without Rb vapor in the chamber.

2.3 Laser systems and optical layout

A number of optical beams with precise frequency were required, for the operation of MOT, state preparation of magnetic trap, detection of atom cloud etc. Frequency of the various laser beams used in our experiments is shown in Fig. 2.4. To generate various optical beams, we have used semiconductor based diode lasers. Now a days, these diode lasers are widely used for laser cooling experiments. These lasers provide a narrow line-width and wide tunability by varying the cavity length in external cavity mode [65–69]. Moreover, these systems are compact and easy to handle. We have used five external cavity diode lasers (ECDLs) designed to operate at a wavelength of 780.2 nm, which is resonant to the D₂-line of ⁸⁷Rb atom. Out of these, three lasers are from Toptica (100 mW power DL 100 model) and two are from Sacher (one is 1 W Tiger series and the other is of 100 mW TEC series). The 1 W model was used as a master laser to generate the cooling beams for VC-MOT and UHV-MOT. Due to some technical problem with the 1 W laser system, it was replaced by a 1 W-Tapered amplifier (BOOSTA, Toptica, Germany) system. This amplifier system was seeded by taking a part of the laser output from the 100 mW DL 100 model. The ECDL system consists of a mounting base serving as a heat sink, a Peltier cooler, a base plate for a laser diode holder and a collimator, a grating mount with a piezoelectric transducer (PZT), and a beam steering mirror to direct the output beam. The grating provides optical feedback for single-mode operation and tunability to the laser system. The cavity length in a ECDL can be tuned by applying

voltage to the PZT. Due to the external mechanical vibrations, fluctuations in the diode injection current, and temperature, the cavity length changes over the time and results in a drift in the output frequency of a diode laser [70]. Hence, the frequency stabilization of these laser systems over a time are necessary.

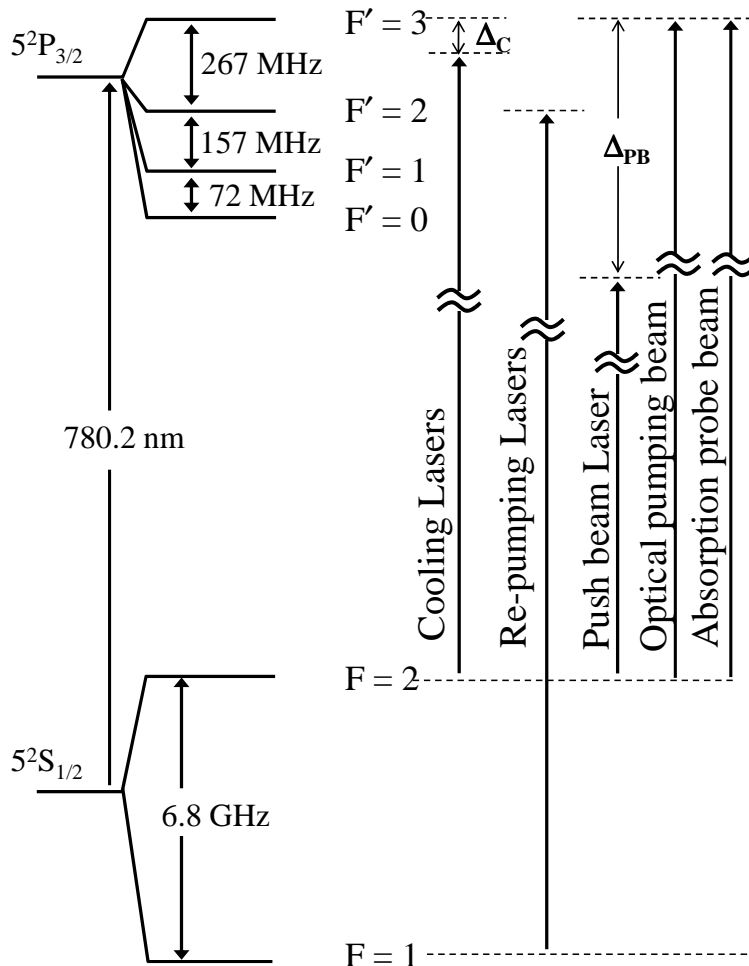


Figure 2.4: The schematic of the frequency detuning of various lasers used in the experiments with respect to the hyperfine atomic transitions of ^{87}Rb atom. Δ_C is the set detuning of the cooling laser, and Δ_{PB} is the detuning of the push beam laser. Δ_{PB} is set to zero for resonant push beam experiments, whereas, it is varied from 0 to -1.2 GHz for red-detuned experiments. Both the transitions ($5S_{1/2} F=2 \rightarrow 5P_{3/2} F'=3$) and ($5S_{1/2} F=1 \rightarrow 5P_{3/2} F'=2$) have the natural line-width of ~ 6 MHz. Diagram not to scale.

2.3.1 Frequency stabilization of ECDL systems

For laser cooling of atoms, the light incident on the atoms should have an accurate detuning with respect to the transition frequency. Therefore a good stabilization of the

laser frequency is essential for the operation of MOT. This can be achieved by active feedback control of the laser frequency. The feedback control monitors the deviation of the laser frequency from a suitable reference and generates a correction mechanism. It is normally an error signal sent to the PZT, that makes the correction to the laser frequency. The frequency reference should be such that, it provides a definite signal on frequency change of the laser. Commonly used frequency references are the resonances of atomic/molecular transitions and modes of a stable cavity/interferometer (e.g. Fabry-Perot etalon). It is convenient to employ a spectral feature corresponding to the atom to be cooled as the frequency reference. A relatively common laser frequency locking method is the side-lock, in which the side of a narrow peak in a saturated absorption spectroscopy (SAS) signal is used to stabilize the lasers.

Saturated Absorption Spectroscopy

To get the spectral features of an atom, generally a laser beam is passed through a cell containing the atomic vapor and then detecting the absorption on a photodiode. But the features which are of interest in laser cooling techniques (i.e. hyperfine transitions) are unresolvable due to the Doppler broadening. Saturation absorption spectroscopy (SAS) [27, 66, 67, 71–73] is a technique which eliminates the Doppler broadening and allows to resolve the hyperfine transitions. The schematic of the experimental setup used for SAS is shown in Fig. 2.5. In SAS two beams, a strong pump beam and a weak probe beam, propagate through a rubidium vapour cell (the atom need to be cooled in our experiment) in opposite directions. As both the beams are derived from the same ECDL system having a narrow line width, at the transition frequency, the pump beam (which is strong) saturates the hyperfine transition and depletes the population in ground state leaving very few atoms for the probe beam to interact with. As a result, the probe beam transmission increases. This happens when both the beam interacts with the zero velocity group of atoms (other velocity group see both the beam Doppler shifted to different frequency). This generates a peak in the transmission spectra. As the excited state and the ground states are multi level, a situation arises for a velocity group, for

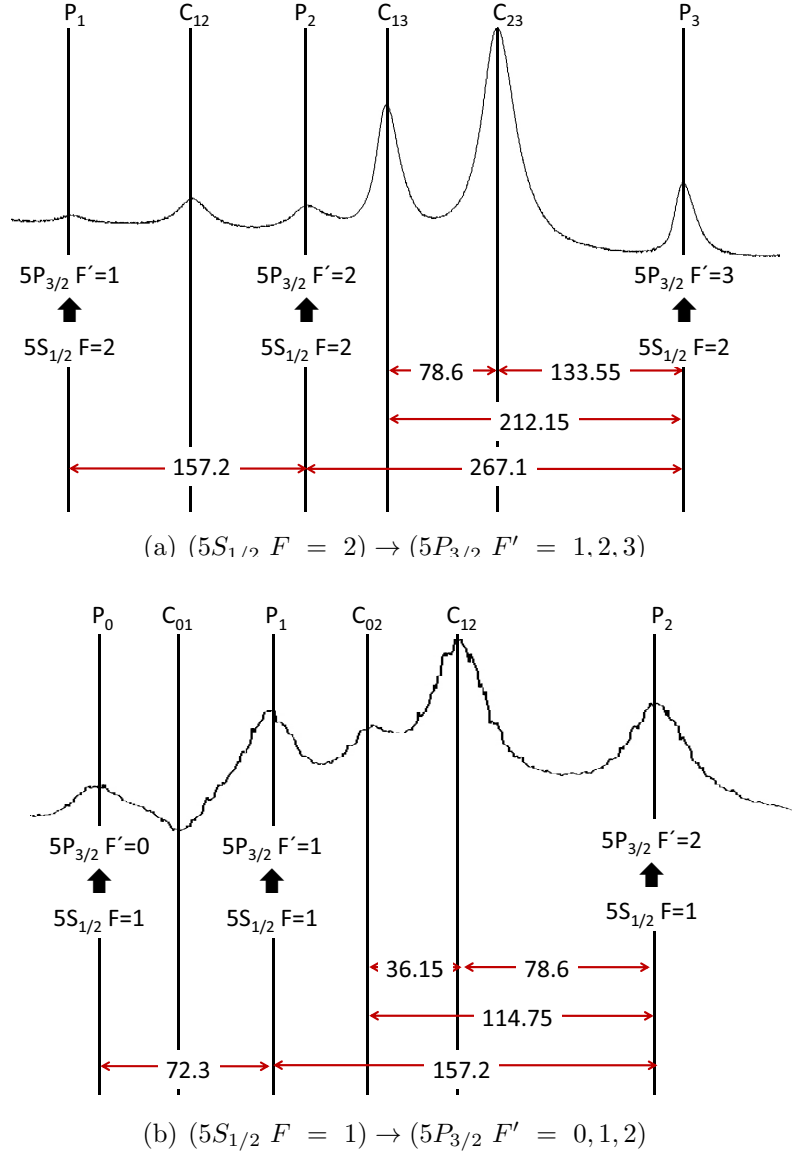


Figure 2.6: Saturated absorption signals generated in a SAS setup. The transitions for the corresponding peaks and cross-overs are shown in the figure. (a) and (b) corresponds to the spectrum for transitions $(5S_{1/2} F = 2) \rightarrow (5P_{3/2} F')$ and $(5S_{1/2} F = 1) \rightarrow (5P_{3/2} F')$ respectively.

2.3.2 Generation of various optical beams

For the operation of the setup, a number of laser beams are needed. Those are VC-MOT cooling and re-pumping beams, UHV-MOT cooling and re-pumping beams, the pushing laser beam, the optical pumping beam and the absorption probe beam. The path of the various laser beams are shown in Fig. 2.7 and their generation is described as follows.



Figure 2.7: A photograph of the table. The lines shows the path of the various generated optical beams. The lines with double arrows represents the AOMs in double-pass configuration. The Splitting of VC-MOT beams and UHV-MOT beams are not shown here. Refer to the text for more details.

- (i). *VC-MOT beams*: The master laser output beam was split to obtain a power of ~ 250 mW for generation of the cooling laser beams for VC-MOT. This beam was first passed through an AOM in double-pass geometry, and the output served as VC-MOT cooling beam. The AOM used here is to control the frequency and the duration of switching-ON of the VC-MOT beams as required by the experiments. The re-pumping laser beam was generated by an ECDL (*TEC series Sacher, Germany*) which was mixed with the above VC-MOT cooling beam. This mixed beam was subsequently expanded (to $1/e^2$ radius of ~ 6 mm) and split into three VC-MOT beams. These three beams had nearly equal cooling laser power of ~ 19 mW in each beam, but different re-pumping laser powers with total of ~ 23 mW in three beams. This unequal division of re-pumping laser power among three beams occurred due to different polarizations of the cooling and re-pumping parts in the mixed beam before the splitting. The desired six VC-MOT beams were obtained by using these three beams in retro-reflection geometry.
- (ii). *UHV-MOT beams*: For the UHV-MOT, another part (~ 230 mW) of the master laser output beam was used for cooling laser beams. This beam was first passed through an AOM in double-pass geometry and then expanded to $1/e^2$ radius ~ 8 mm. Similarly, the re-pumping laser beam (output of another ECDL, *DL 100, Topica, Germany*) for UHV-MOT was first passed through another AOM in double-pass geometry, and then expanded to $1/e^2$ radius of ~ 6 mm (power ~ 28 mW). The two independent AOMs used for cooling and re-pumping beams can independently control the frequency and power of the cooling and re-pumping beams. After the above expansion of the output after AOMs, the cooling and re-pumping beams were combined. The combined beam was then split into six beams which were used as independent UHV-MOT beams. All these six UHV-MOT beams contained nearly equal cooling laser power of ~ 10 mW in each beam, but unequal re-pumping power. Here also, the unequal re-pumping power among six beams were due to different polarizations of cooling and re-pumping parts in the combined beam before the splitting.

- (iii). *Push beam*: The push beam was obtained from a grating controlled ECDL (*DL 100, Toptica, Germany*). The frequency of the push beam was varied by adjusting the piezo voltage supplied to the grating in the laser to obtain the desired value of its detuning $\delta/2\pi$ with respect to $(5S_{1/2} F = 2) \rightarrow (5P_{3/2} F' = 3)$ transition of ^{87}Rb . It was first passed through an AOM and then expanded to $1/e^2$ radius of ~ 2 mm. The maximum power at the entrance of the vacuum chamber was ~ 25 mW. It was then focused on the VC-MOT using a lens of focal length ~ 300 mm (mounted on a vertical translational stage outside the VC-MOT chamber) to a spot radius ($1/e^2$ radius) of $\sim 35 \mu\text{m}$ to eject a flux of atoms from VC-MOT cloud to load UHV-MOT. The spot-size at VC-MOT can be varied by translating the position of the focusing lens. The optimization of the spot-size for loading of UHV-MOT is presented in section 4.3 [74].
- (iv). *Optical pumping beam*: To perform the optical pumping of atoms to $5S_{1/2} |F = 2, m_F = 2\rangle$ state, small parts of the cooling (master laser) and re-pumping (*DL 100, Toptica, Germany*) lasers (~ 2 mW power in each) were mixed and passed through an AOM in double pass configuration. The output of this AOM ($\sim 500 \mu\text{W}$) was then expanded to $1/e^2$ radius of ~ 3 mm, and was aligned to one of the UHV-MOT beam (z-direction) in such a way that, the helicity of the light was σ^+ polarized.
- (v). *Absorption probe beam*: A part of the laser (used for seeding of the amplifier, *DL 100, Toptica, Germany*) was used as a probe beam for characterization of the cloud. For that a small part of the laser beam ~ 2 mW was passed through an AOM in double pass mode and then the output was expanded to $1/e^2$ radius of ~ 6 mm using a lens combination. An aperture of $100 \mu\text{m}$ was used at the focal position for spatial filtering of the probe beam so that a good quality beam could be obtained for imaging. This beam was mixed with the z-direction beam using a PBS.

2.4 MOT coils

This section describes about the coils, which were used for generating the magnetic fields required for the operation of magneto-optical trap.

Coils for VC-MOT: Two identical coils, each of 150 number of turns with internal diameter (ID) 57 mm, external diameter (ED) 66 mm and height 38 mm, were used to generate the quadrupole field. The coils provide a field gradient of ~ 10 G/cm in the axial direction for a separation of 5.5 cm, when a DC current of 3 A is supplied in each coil in opposite direction.

Coils for UHV-MOT: A pair of coils, for generating quadrupole field for the operation of UHV-MOT was designed. Each of these coils are having 230 number of turns with dimension as: ID = 34 mm, ED = 70 mm, height = 35 mm. These coils generate a field gradient of ~ 10 G/cm for a current of 1 A. The same coils were used to form the quadrupole trap by flowing a higher current, and subsequently, by adding a third conical coil (Ioffe coil), we were able to form the quadrupole-Ioffe configuration trap (details of QUIC trap is discussed in magnetic trap section). To dissipate the heat generated by flowing a higher current through the coils, these coils were kept inside a water cooling jacket, which allows in removing the heat by flowing water.

2.5 Formation of MOTs

The three VC-MOT beams were passed through three mutually perpendicular ports of the VC-MOT chamber and were retro-reflected to generate the six beams required for MOT operation. A DC current of ~ 3 A was passed through the VC-MOT coils to generate the required magnetic field gradient. The polarization of the VC-MOT beams were set using quarter-wave retardation plates before the entrance of the VC-MOT beams to the vacuum chamber. The Rb-vapor was injected in the octagonal VC-MOT chamber by passing a DC current of ~ 2.7 A in the Rb-getter source to form the VC-MOT. This VC-MOT acts as a source of atoms for loading of the UHV-MOT. The push laser beam was aligned in such a way that, it ejects a flux of atoms from the VC-MOT in the

vertically downward direction for loading of the UHV-MOT, which was formed in the glass cell (in UHV environment) at 360 mm below the VC-MOT position. The six UHV-MOT beams were aligned in three mutually perpendicular directions. The UHV-MOT quadrupole coils generate the necessary field gradient for the formation of UHV-MOT. In our experiments, the UHV-MOT was loaded for 40 s duration over which push beam was kept on. After choosing the parameters appropriately, we could obtain $\sim 1 \times 10^8$ atoms in the VC-MOT and $\sim 2 - 3 \times 10^8$ atoms in the UHV-MOT in our setup. The temperature of atom cloud in UHV-MOT ranges from $50 \mu K$ to $500 \mu K$. This number of atoms and temperature are dependent on various parameters, like Rb vapor pressure, background pressure, beam power and detuning, field gradient and also on the alignment of the beams.

2.6 Characterization of cold atoms in MOTs

To characterize an atom cloud, the number of atoms, size of the atom cloud, and its temperature are the important parameters which needs to be deduced.

2.6.1 Measurement of number of atoms in MOT

The fluorescence emitted by the trapped atoms due to scattering by a resonant beam can be used to calculate the number of atoms in a MOT. The fluorescence, imaged on a CCD camera is a relatively easy technique to measure the number of atoms [75]. In this method, the size of the cloud is also deduced from the same image. The schematic of the fluorescence imaging technique is shown in the Fig. 2.8.

An atom cloud with N number of atoms, when shined with a light of intensity I_0 and detuning Δ , it scatter photons isotropically with a rate γ_{sc} given by equation (1.3). The number of photons N_p collected in a solid angle $d\Omega$ subtended on the collecting lens used to image on the CCD camera with an exposure time (t_{exp}) is given by,

$$N_p = N \cdot \gamma_{sc} \cdot \frac{d\Omega}{4\pi} \cdot t_{exp} \quad (2.3)$$

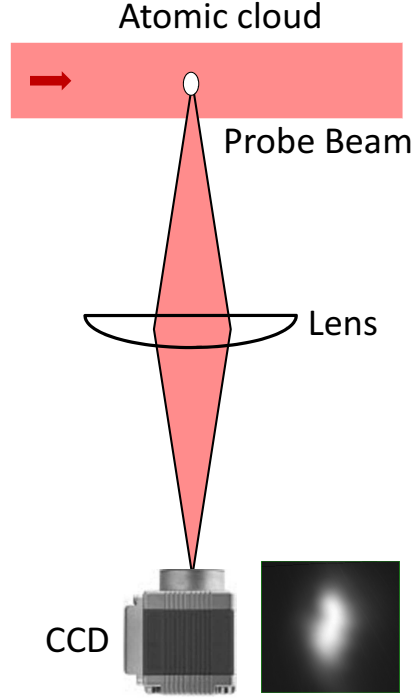


Figure 2.8: Schematic of the fluorescence imaging technique. A typical fluorescence image of a MOT is also shown.

If η is the quantum efficiency of the CCD camera, then N_p number of photons give a CCD count N_c ,

$$N_c = N_p \cdot \eta \quad (2.4)$$

For example, if N_c is the count obtained from a MOT image then the number of atoms may be inferred as,

$$N = \frac{8\pi \left[1 + 4 \left(\frac{\Delta_C}{\Gamma} \right)^2 + \left(6 \frac{I_0}{I_{sat}} \right) \right]}{\Gamma \left(6 \frac{I_0}{I_{sat}} \right) t_{exp} \eta d\Omega} N_c \quad (2.5)$$

where I_{sat} is the saturation intensity, I_0 is the intensity of each cooling beam in the MOT, $\Gamma = 2\pi \times 6$ MHz is the Rb⁸⁷ natural line-width, Δ_C is detuning of cooling beam and $d\Omega$ is solid angle for collection of fluorescence by the CCD. We estimated the number of atoms in the MOTs by analyzing fluorescence images obtained with a CCD camera (pixelfly QE).

2.6.2 Measurement of atom cloud temperature

The concept of temperature in laser cooling is totally different from the conventional thermodynamic concept of temperature. Here it is mainly inferred from the spread in velocity distribution of the atom cloud. Several methods have been proposed and demonstrated for its measurement [76]. Time of flight method, which is based on measuring the signal from a ballistically expanding cloud is one of the most extensively used technique [77–82]. Among others, the release-recapture technique [29], forced-oscillation of atom cloud [83], MOT fluorescence spectrum analysis [84], transient four-wave mixing [85], single parameter transient absorption [86], one dimensional expansion method [87], vacuum Rabi splitting [88] were also used for measuring the temperature of an atom cloud.

We have implemented a method, which is an extension of the time-of-flight technique known as free-expansion method, developed by Myrskog et al. [89]. In this technique the rate of expansion of atom cloud after removing the trapping forces is measured, which gives an estimate of the initial velocity/temperature of the cloud [90, 91]. To measure the temperature, we loaded the MOT for a finite duration by applying a voltage pulse to the AOM (which controls the cooling beams), and subsequently a probe pulse of duration $100 \mu\text{s}$ was shined on the expanding cloud after a finite interval (t), and the image of the expanding cloud was captured on a CCD. The procedure was repeated by gradually increasing the interval and from these images we find out the r.m.s. size of the cloud ($\sigma(t)$). From these expanding cloud images we estimate the temperature as follows,

$$\sigma(t)^2 = \sigma(0)^2 + (k_B T/m)t^2, \quad (2.6)$$

where $\sigma(0)$ is the initial root mean square (r.m.s.) width of the cloud, and $\sigma(t)$ is the r.m.s. width at time t , T is the temperature of the cloud, k_B is the Boltzmann's constant, and m is the mass of the atom. Using this method, the cloud of the atoms in a VC-MOT was measured to be $\sim 300\mu\text{K}$. This temperature changes with changing the MOT parameters.

2.7 Design of magnetic trap

The simplest magnetic trap for atoms is a quadrupole trap [92], but it has high loss rate due to Majorana spin flips occurring at trap center because of zero magnetic field at the centre [40]. Due to this reason, a quadrupole trap is usually not suitable to perform evaporative cooling to achieve BEC. Among the other popular magnetic trap designs [43] used to achieve BEC, a quadrupole-Ioffe configuration (QUIC) trap [48] is convenient and operates at low current as compared to other traps. A QUIC trap is formed when a third coil (called Ioffe coil) is added to quadrupole trap having two identical coils carrying current in anti-Helmholtz type of configuration. The Ioffe coil is kept at 90 degree to the quadrupole coils such that its axis is perpendicular to the quadrupole coils axis and passes through the quadrupole trap centre. When there is no current in the Ioffe coil, a QUIC trap has the field distribution that of a quadrupole trap. When Ioffe coil current is increased, the resultant field distribution is modified from that of the quadrupole trap. At certain value of Ioffe coil current, a quadratic field distribution with non-zero offset field is obtained, which is known as Ioffe configuration of QUIC trap. The magnetic trapping of atoms around this minimum is free from Majorana spin flips, hence suitable for evaporative cooling to achieve BEC.

The schematic of the QUIC trap, which was developed for our setup is shown in Fig. 2.9. The coil dimensions were fixed by the simulations of the magnetic field suitable for our geometry. The coils, which were used to generate the quadrupole field for UHV-MOT are used here in conjunction with a third coil to form the QUIC trap. The third coil is a conical coil with conical section (with 78 number of turns) of 16 mm with minimum diameter (inner) 6 mm and maximum diameter (outer) 35 mm, and the straight section has length 18 mm (with 160 number of turns). We have measured the magnetic field, when the separation between the quadrupole coils was set to 50 mm and the Ioffe coil position is at 24.5 mm from the centre of the quadrupole coils. The results for a particular set of current is shown in the Fig. 2.10. We have observed a good agreement between the experimental and simulated values. Later on as per our requirements, the separations between the coils were modified as shown in Fig. 2.9.

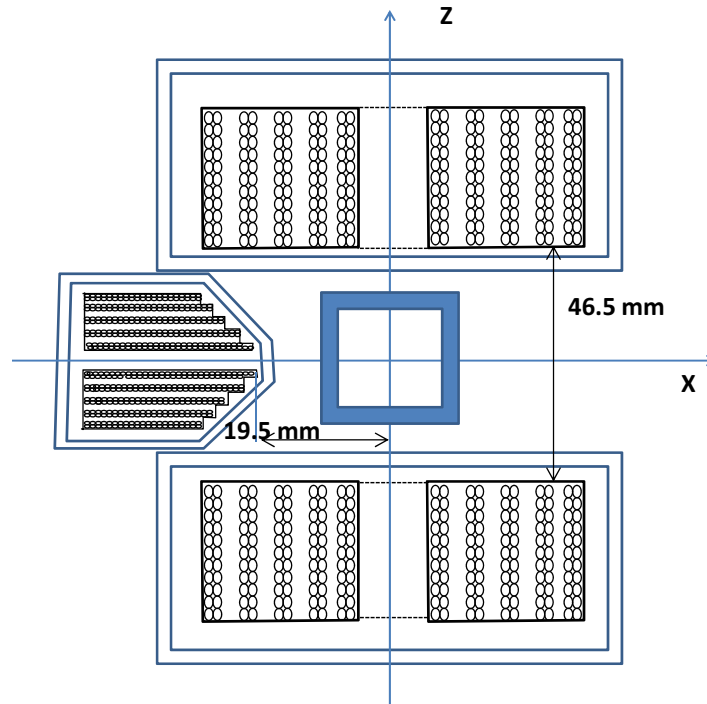


Figure 2.9: Schematic of the arrangement of the coils in QUIC trap for our setup.

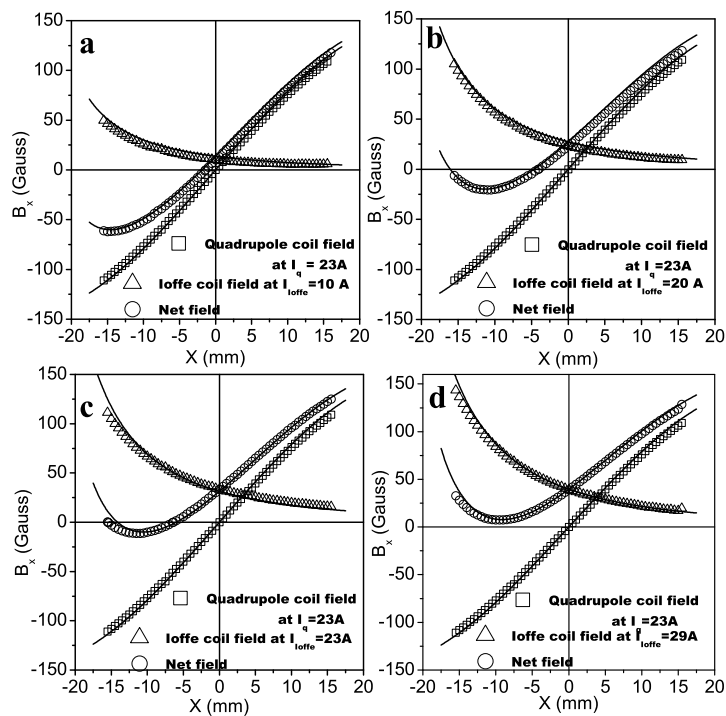


Figure 2.10: Variation in the magnetic field along the Ioffe coil axis with distance at quadrupole coil current 23 A and variable Ioffe current. The solid lines show the simulated magnetic field.

2.8 Loading of a magnetic trap

During loading of the QUIC trap from cold atoms in UHV-MOT is transformed in the following steps.

- *Compressed MOT:* We formed the compressed-MOT (for duration ~ 20 ms) by increasing the detuning of the cooling laser beams to further red side of ω_{Lock} and increasing the magnetic field gradient of the UHV-MOT coils.
- *Optical molasses:* Then atoms from UHV-MOT after the CMOT stage were stored in molasses for duration of ~ 5 ms (achieved by switching-off the magnetic field of the UHV-MOT).
- *Optical pumping:* Before transferring the atoms to the quadrupole trap, we performed optical pumping of atoms to $5S_{1/2} |F = 2, m_F = 2\rangle$ state. The optical pumping beam (described in 2.3.2 was passed for ~ 500 μ s in presence of a small bias field (~ 2 G, ~ 1.5 ms duration) to transfer the UHV-MOT atoms to the desired trappable state i.e. ($5S_{1/2} |F = 2, m_F = 2\rangle$).
- *Loading of the quadrupole trap:* The current in quadrupole coils was switched on at ~ 13 A in ~ 2.5 ms time and finally ramped-up to 23 A in 500 ms.
- *Formation of QUIC trap:* After quadrupole coils current reaches the final value (23 A), current in Ioffe coil was slowly ramped (in 500 ms) from 0 to 19.5 A to convert quadrupole trap configuration into QUIC trap configuration. As shown in Fig. 2.10, the minimum of resultant field (also of the potential energy) in our QUIC trap appears at a position $x \sim -8.9$ mm. To detect atoms in QUIC trap, we have shifted absorption probe and imaging optics (including CCD) according to this shift.

During the magnetic trapping of atoms, it is important that all kinds of residual/unwanted light going to magnetic trap area should be stopped, so that a complete dark background can be obtained during trapping. The solenoid actuator based mechanical shutters (described in electronics and controller section) were used at different places in the path of

the laser beams which were kept closed during the magnetic trapping to stop the light leaked from various AOMs used for the cooling, re-pumper, and push laser beams.

2.9 Evaporative cooling system

Evaporative cooling is a technique to further cool the atoms below the temperature achievable by laser cooling. The evaporative cooling performed in a magnetic trap is of forced type, where the high energy atoms are removed by applying radio frequency (RF) radiation. This process is a stimulated emission process, which can be initiated by RF field of appropriate frequency, such that photon energy ($h\omega_{RF}$) matches with the magnetic splitting between sublevels (as shown in Fig. 2.11).

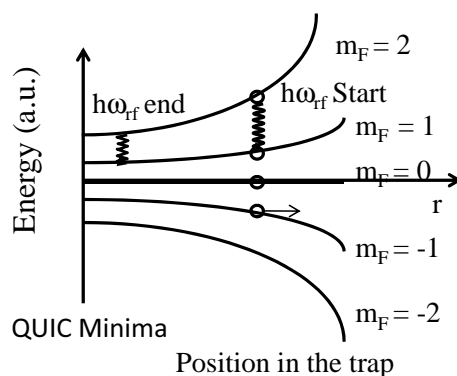


Figure 2.11: Schematic of the RF field stimulated transitions leading to ejection of an atom during RF-evaporation process.

For evaporative cooling of ^{87}Rb atoms trapped in our QUIC trap, we applied RF

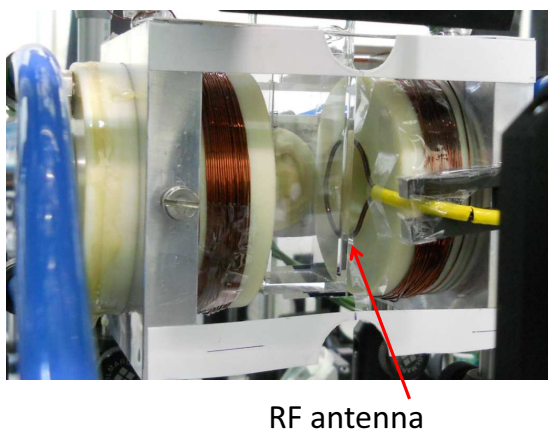


Figure 2.12: Image of the single loop antenna used for radiating the RF-field.

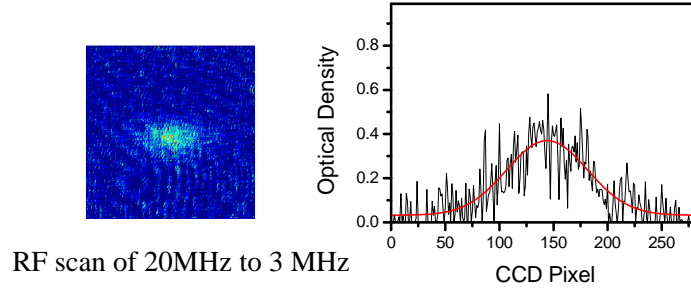


Figure 2.13: An image of the optical density of a cloud after RF evaporation. The profile along a horizontal line is shown in the graph.

radiation emitted from a single loop antenna kept at one side of the glass cell (shown in Fig. 2.12). The axis of this loop antenna was kept along the axis of quadrupole coils (z-axis). A logarithmic variation in frequency of RF emission with time (called RF scan), over a selected initial and final values of frequency (i.e. scan range), was implemented for efficient evaporative cooling of atoms in the trap.

RF evaporation is able to reduce the temperature of laser cooled atoms. In our experiments we could obtain a variable temperature in the range of few μK . Fig. 2.13 shows the image of cloud which correspond to the temperature of $14 \mu K$ after evaporative cooling of a cloud which was initially at temperature $100 \mu K$ in the QUIC trap. The image is obtained using the absorption probe technique described below.

2.10 Absorption probe imaging

Among the different techniques used to characterize cold atom cloud, absorption probe imaging is a widely used and sensitive technique [93–95]. In absorption probe technique, the atom cloud is illuminated by a low intensity resonant probe laser beam and the “shadow” left by the atomic absorption is imaged on a CCD camera (the schematic is shown in Fig. 2.14).

To implement the absorption probe imaging technique, we grabbed three images to get the required information; (i) image in absence of any probe beam (IBG), (ii) the probe beam image in absence of cold atom cloud (IP), and (iii) image of the probe beam after the beam was transmitted through the atom cloud (IT). From these three images

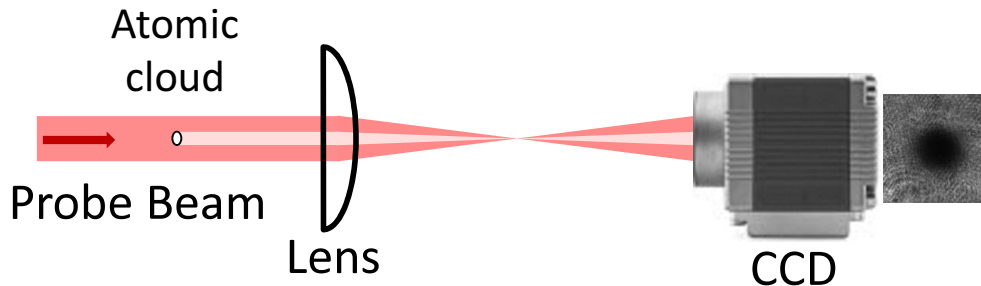


Figure 2.14: Schematic of the absorption probe technique. A typical CCD image of probe beam transmitted through ^{87}Rb atom cloud is also shown. The dark spot near the centre in the image shows the absorption of probe intensity by atom cloud.

using a Matlab based program, we extracted the optical density, which is given as,

$$OD(i, j) = \ln \left(\frac{IP(i, j) - IBG(i, j)}{IT(i, j) - IBG(i, j)} \right) \quad (2.7)$$

where $OD(i, j)$ is the optical density on (i, j) th pixel and $IBG(i, j)$, $IP(i, j)$ and $IT(i, j)$ are the intensity values for the (i, j) th pixel for IBG, IP and IT respectively. This optical density is directly proportional to the integrated column density of the cloud. The number of the atoms in the cold atom cloud is obtained from $OD(i, j)$ as,

$$N = \frac{1}{\sigma} A_{\text{pixel}} \sum_{i,j} OD(i, j) \quad (2.8)$$

where σ is the absorption cross section for atoms at probe laser wavelength, and A_{pixel} is the pixel area of the imaging CCD. Our camera is a digital CCD camera (*Pixelfly, PCO, Germany*) having 1392×1024 pixels (pixel-size $6.45 \mu\text{m} \times 6.45 \mu\text{m}$) which is used in conjunction with a PCI-interface-board on a computer to record the absorption images. The intensity of the absorption probe beam was adjusted appropriately, to get a good signal to noise ratio during the absorption probe imaging.

2.11 Controller system

For generation, manipulation of ultra cold atoms, and finally achievement of BEC, requires execution of different events in a synchronous manner, which requires high precision

electronic controller system. The different events which are described above involve loading of magneto-optical traps, transfer of atoms to magnetic traps, and then doing RF evaporation and finally detection of the BEC atom cloud. In order to accomplish the above events in a precise sequence, we need to activate and control several instruments within a short duration. The time scale involved in the process ranges from micro-second to few second order. For this purpose, a PC based automation system was developed to generate the control signals with a defined sequence and timing precision. In order to meet the demand for very short time interval (few micro-second) for some of the signals and tight synchronization among them, a dedicated micro-controller based slave controller was developed. The control program at PC was developed in LabView which provides a graphic user interface (GUI) to configure the various timing as per the experimental requirement. The GUI is shown in Fig. 2.15. These time interval settings were transferred to the slave controller through RS-232 serial interface for execution. The higher level communication protocol with GPIB bus was handled by the PC itself. An eight channel 8-bit DAC card was developed to provide (0-5 V) analog control signals. This DAC add-on card sits on the slave micro-controller backplane bus. Various devices controlled in the experiments were AOMs for switching the laser beams, power supplies for current in coils, function generator for RF radiation, CCD camera for detection, mechanical shutters etc. These devices were controlled to execute the sequences of MOT formation \rightarrow magnetic trap loading \rightarrow RF evaporation \rightarrow imaging.

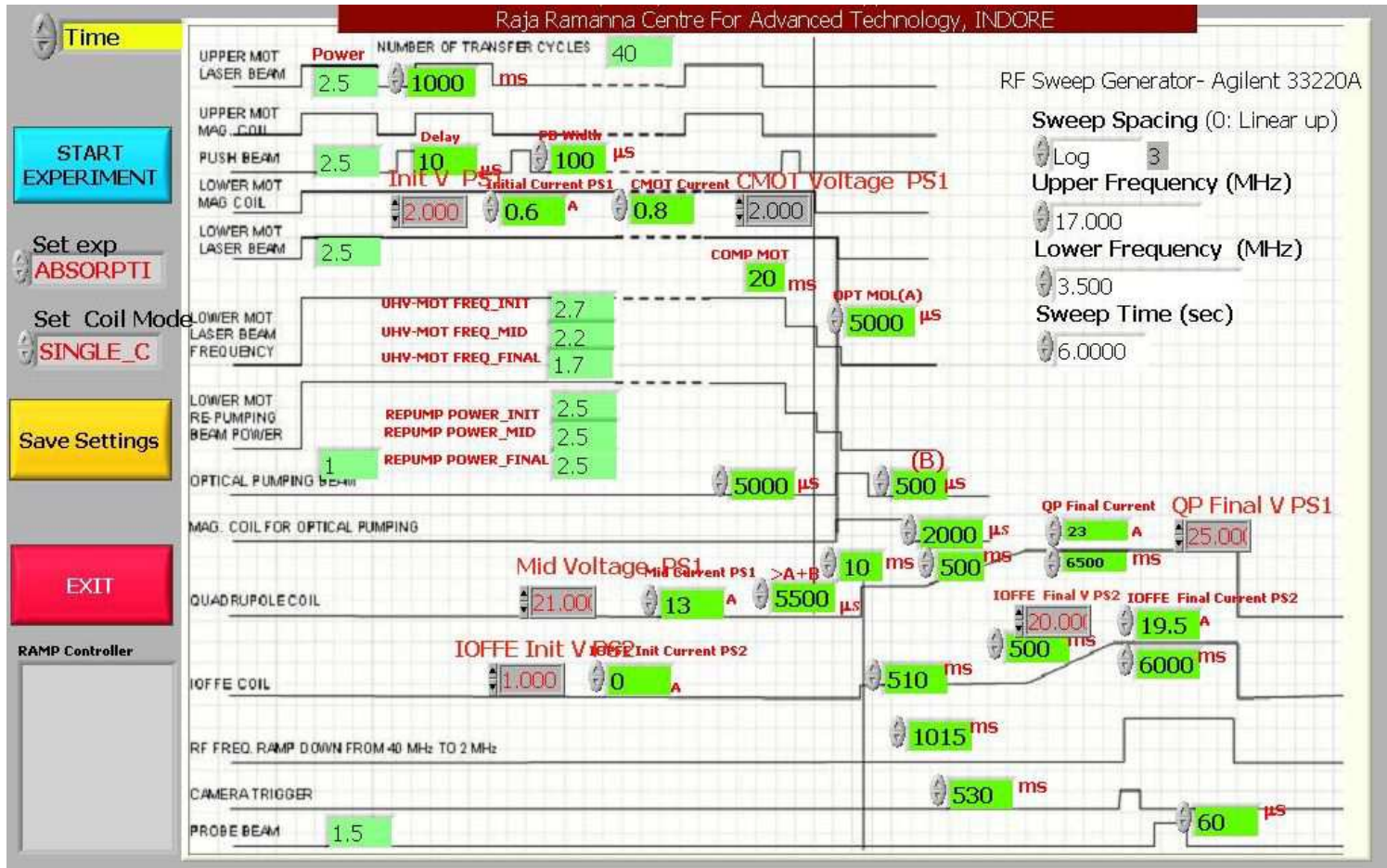


Figure 2.15: An image of the graphical user interface used for entry of various parameters for execution of the different events.

Controls for AOMs

The AOM driver has two independent controls for controlling the amplitude modulation and frequency modulation of the RF-signal fed to the AOM which can be operated in external as well as internal mode. When control signals are applied at power input and frequency input of the AOM driver the power and frequency of the first order optical output of the AOM can be varied. the optical pulses of desired power and frequency can be generated. As the angular shift of the laser beams depends on the RF frequency fed to the AOM, hence, AOMs are usually used in double pass for compensating the angular shift while detuning the frequency.

Six number of AOMs were used to control (i) the VC-MOT cooling beam, (ii) the UHV-MOT cooling beam, (iii) the UHV-MOT re-pumper beam, (iv) the push beam, (v) the optical pumping beam and (vi) the probe beam.

Though the AOMs in double pass mode give a good extinction when used in pulsed mode, still some light reaches to the magnetic trapping region. These lights are harmful for the magnetic trapping. Therefore we have also used mechanical shutters in conjunction with the AOMs to switch ON and OFF all the optical beams reaching to the trapping region. For this a trigger pulse (5 V) was generated by the computer controller. The trigger pulse was used to control the driver circuit of a solenoid based actuator (*Lucas Ledex, 9136A-35 USA*), which derives a knife-edge (a razor blade is soldered on the axis of the actuator) to switch ON/OFF the laser pulse. The driver circuit provides the required voltage (12 V to 18 V) for operation of the actuators. We have observed that the rise-time and fall-time of the shutters were improved by keeping them at the focal position of a beam.

Controls for power supplies

DC power supplies (Xantrex make) were employed for magnetic field generation. Operating current and voltage of two power supplies were controlled. These power supplies were used in MOT. Other two power supplies driving quadrupole and Ioffe coils; need ramping control of the output current (i.e. resulting magnetic field) which was implemented by

providing the ramping voltage control input from the slave microcontroller. In order to obtain faster switching (ON/OFF) speed for the magnetic field, external IGBT switches have been added to each power supply. The slave micro-controller unit provides the TTL ON/OFF control signal for the magnetic field.

PC controls a function generator (*Agilent 33220A*) using GPIB bus and generates a predefined frequency sweep for RF evaporation.

2.12 Summary

In this chapter, a brief description of the experimental apparatus used in this thesis work is provided. In the double-MOT setup of ^{87}Rb atoms, we have used various laser systems, vacuum system, controller system and various optical components to manipulate and steer the laser beams. For magnetic trapping, we have used quadrupole and QUIC traps, whose configuration have been discussed. Then the loading of QUIC trap starting from UHV-MOT is also presented. Finally, the evaporative cooling to cool UHV-MOT atoms in QUIC trap is discussed, which typically results in temperature that is lower than the temperature of atom in the UHV-MOT.

Chapter 3

Atom transfer with resonant push beam in the double-MOT setup

3.1 Introduction

The collection of a large number of atoms in UHV-MOT in the double-MOT setup [60, 96] is quite important. Various methods are employed for transfer of atoms from a VC-MOT to UHV-MOT. Among them, the simplest is free fall of atoms where atoms released from the VC-MOT are allowed to fall under gravity and then recaptured in the UHV-MOT [97]. Though the method is simple, the loading rate is rather poor ($\sim 20\%$). Gibble et al. [96] have used a moving molasses technique [98] in which the atoms are launched upward from the VC-MOT to load the UHV-MOT. The low velocity intense source (LVIS) of atoms scheme [99] employed for loading of a second MOT [100, 101] relies on creation of a hole on one of the mirror used for the VC-MOT. The hole creates an imbalance in trapping forces and allows atom flux to pass through it for loading of the second MOT. A pyramidal MOT [102, 103] with a small hole at the vortex is also used to generate a source of cold atoms for loading of an UHV-MOT. Moving magnetic coils [104, 105] are also used by a few groups for loading of the UHV-MOT. Several groups [60, 106–108] have used a push beam to eject the flux of atoms from the VC-MOT for loading of the UHV-MOT. Technical complications associated with the other methods [96, 100–105] described before

arise either due to setting up of optical components inside the vacuum chamber or due to precise movement of components outside the chamber. This makes the implementation of these schemes challenging. The use of push beam is simple and convenient. To enhance the transfer efficiency in the push beam transfer method, auxiliary techniques like use of two-dimensional cooling [106], and guiding magnetic fields [60] have also been reported, but there are other design considerations associated with these schemes.

We have chosen to investigate the transfer of atoms from VC-MOT to UHV-MOT using a resonant push beam. This chapter describes our work on use of a push beam which is resonant to $(5S_{1/2} F = 2) \rightarrow (5P_{3/2} F' = 3)$ transition of ^{87}Rb for transfer of atoms from VC-MOT to UHV-MOT. We have used the push beam in different schemes. First, we have studied the effect of using an auxiliary hollow beam in conjunction to a low power resonant push beam and then we have made a comparative study of the transfer process in various geometries such as pulsed and continuous mode.

3.2 Use of resonant push beam in presence of a hollow beam for atom transfer

In this section, we discuss about our work on use of a hollow laser beam in conjunction with the resonant push beam to enhance the atom transfer between VC-MOT and UHV-MOT. The experimental layout uses a weakly focused hollow laser beam aligned to propagate opposite to the direction of the push beam and atomic flux ejected from VC-MOT such that both the MOTs were in the dark region of the hollow beam. The experimental results have shown a significant enhancement in the number of atoms in the UHV-MOT in the presence of the hollow beam when it was tuned appropriately. The observed enhancement in number of atoms in the UHV-MOT has been attributed to the cooling and transverse guiding of flux of atoms reaching the UHV-MOT due to interaction of atoms in the flux with the hollow beam.

3.2.1 Description of the setup with hollow beam

Figure 3.1 shows a schematic of the experimental setup used for studying the atom transfer from VC-MOT to UHV-MOT in presence of a hollow beam. In the setup used for the experiments, the upper MOT was the VC-MOT formed in an octagonal stainless steel chamber and the lower MOT was the UHV-MOT formed inside a quartz glass cell (polished but uncoated). Both the chambers were connected using a tapered tube (DPT: inner diameters of 5.0 mm at upper end and 12.0 mm at lower end) which allowed differential pumping and provided convenient passage for the converging hollow beam propagating in upward direction. The VC-MOT and the UHV-MOT positions were vertically separated by ~ 340 mm. With above differential tube (DPT) and suitable vacuum pumps, base pressure of $\sim 1 \times 10^{-8}$ Torr and $\sim 1.2 \times 10^{-9}$ Torr were respectively obtained in the the upper and the lower chambers. On heating a Rb getter in the upper chamber, Rb-vapor was generated and the pressure in the chamber was increased to $\sim 2 \times 10^{-8}$ Torr.

The cooling laser beams for the two MOTs were obtained from two separate grating controlled external cavity diode lasers and the re-pumping laser beams were obtained by dividing output from a single laser of similar configuration. For each MOT, the cooling beam and the re-pumping beam were first mixed, and the combined beam was then expanded and split into three MOT beams which entered the chamber. After retro-reflection of each of these three beams by a mirror at the exit of the chamber, the required six MOT beams were obtained. For the VC-MOT, total power in the three beams (each of diameter 10 mm) entering the chamber was ~ 26 mW (with ~ 17 mW in the cooling part and ~ 9 mW in the re-pumping part). For UHV-MOT, the total power in the three beams (each of diameter 7 mm) was ~ 27 mW (with ~ 18 mW in the cooling part and ~ 9 mW in the re-pumping part). All the lasers were locked using the hyperfine absorption signals generated by saturated absorption spectroscopy (SAS). The cooling laser was locked at the side of the hyperfine absorption peak at desired detuning using a suitable reference voltage. The repumper laser was stabilized at the peak using frequency modulation (FM) scheme to generate dispersive-like signal. The cooling lasers were locked at ~ 12 MHz

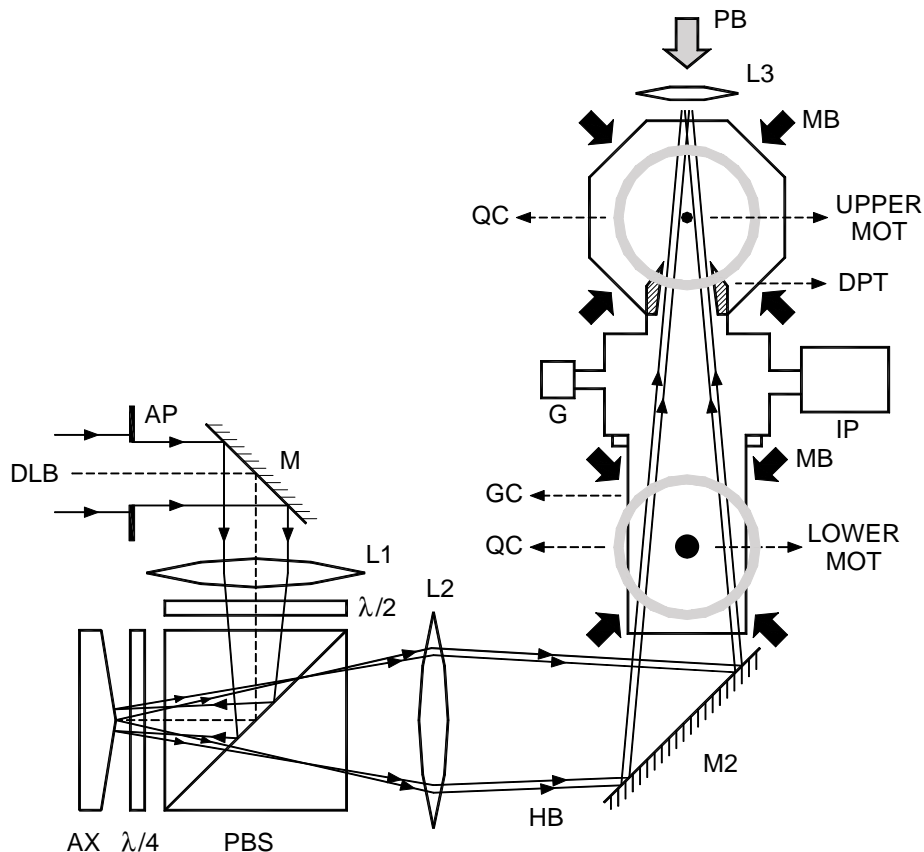


Figure 3.1: Schematic of the experimental setup. DLB: diode laser beam, AX: axicon mirror, $\lambda/2$: half wave plate, $\lambda/4$: quarter wave plate, PBS: polarizing beam splitter, L1, L2, L3: lenses of 80 mm, 250 mm, 300 mm focal length, HB: hollow beam, MB: MOT beams, PB: push beam, IP: sputter ion pump, G: vacuum gauge, GC: glass cell, QC: quadrupole coil, DPT: differential pumping tube, upper MOT:VC-MOT and lower MOT:UHV-MOT.

to the red of $(5S_{1/2} F = 2) \rightarrow (5P_{3/2} F' = 3)$ transition of ^{87}Rb , whereas re-pumper laser was locked at peak of its $(5S_{1/2} F = 1) \rightarrow (5P_{3/2} F' = 2)$ transition. The required polarizations of the MOT beams were set using the quarter wave-plates. The quadrupole coils (QCs) generated the axial magnetic field gradients of ~ 12 G/cm in the VC-MOT and ~ 10 G/cm in the UHV-MOT.

The push beam was a continuous wave Gaussian laser beam resonant with $(5S_{1/2} F = 2) \rightarrow (5P_{3/2} F' = 3)$ transition of ^{87}Rb . It was focused to $1/e^2$ size ~ 100 μm at the VC-MOT position, which corresponded to a push beam intensity at VC-MOT of $\sim 10^3$ mW/cm^2 and at UHV-MOT ~ 13 mW/cm^2 for a power of ~ 150 μW . Atoms ejected from the VC-MOT by the push beam were captured in the UHV-MOT. A weakly focused

hollow laser beam propagating vertically upwards was aligned such that both the MOTs were in its dark central region. The hollow beam was generated using a homemade metal axicon mirror (AX), reported in detail elsewhere [109]. As shown in Fig. 3.2, the peak to peak intensity diameter and ring-width (FWHM) of the hollow beam were, ~ 14.3 mm and ~ 1.4 mm at the UHV-MOT and ~ 3.2 mm and ~ 1.24 respectively mm, at the VC-MOT. This corresponds to peak intensities ~ 50 mW/cm² and ~ 230 mW/cm² at UHV-MOT and VC-MOT plane respectively, for a beam power of 30 mW.

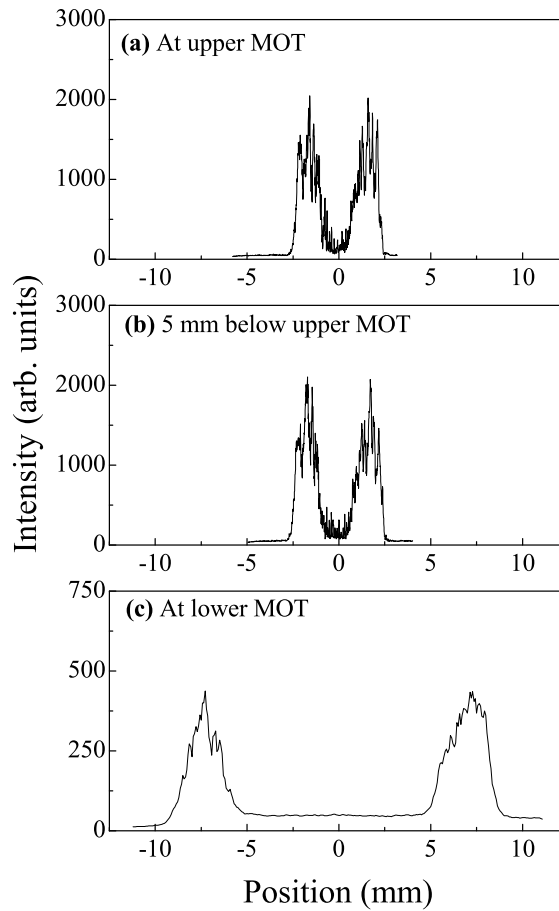


Figure 3.2: Intensity profiles of the hollow beam at different positions. (a): at VC-MOT, (b): at 5 mm below the VC-MOT, and (c): at UHV-MOT. The hollow beam images are shown in the right hand side of the figure.

We estimated the number of atoms in the two MOTs by analyzing fluorescence images (as described in the chapter 2) obtained with a digital CCD camera as reported earlier [75].

3.2.2 Result on atom transfer in presence of hollow beam

In the absence of the push beam and the hollow beam, the VC-MOT had $\sim 1.4 \times 10^6$ atoms in it at temperature $\sim 300 \mu\text{K}$ whereas UHV-MOT did not have a measurable number of atoms. After switching-ON the push beam, the atoms were ejected from the VC-MOT and trapped in the UHV-MOT. A focused push beam imbalances the trapping forces in a small region of the VC-MOT volume. It, thus, creates a small leak in the VC-MOT to give a continuous flux of atoms from the VC-MOT to the UHV-MOT. The number of atoms accumulated in the UHV-MOT depended on the power of the push beam. The number of atoms in the UHV-MOT varied with push beam power (ranging from $10 \mu\text{W}$ to $200 \mu\text{W}$) and the maximum trapped number of atoms ($\sim 1 \times 10^6$) was achieved for the push beam power of $\sim 160 \mu\text{W}$. This relatively low number in both the MOTs, as compared to the number of atoms that was achievable at that time world-wide, was due to the limited power ($\sim 100 \text{mW}$) available in our cooling laser system.

When hollow beam was also switched-ON, the number of atoms in the UHV-MOT changed significantly and this change was dependent on the power as well as the frequency of the hollow beam. Fig. 3.3 (a) and (b) show the observed variation in the number of atoms in the UHV-MOT with hollow beam frequency detuning (δ) from the cooling transition ($(5S_{1/2} F = 2) \rightarrow (5P_{3/2} F' = 3)$ of ^{87}Rb atom) for two values of powers of the hollow beam, at push beam power of $160 \mu\text{W}$. The horizontal lines in the figure show the atom number in the UHV-MOT in the absence of the hollow beam. As can be seen from Fig. 3.3, significant enhancement in the number of atoms in UHV-MOT was observed for certain ranges of both positive and negative detunings of hollow beam frequency. The cold atom cloud in the lower MOT (UHV-MOT) was destroyed when the frequency of the hollow beam was resonant with $(5S_{1/2} F = 2) \rightarrow (5P_{3/2} F' = 2, 3)$ transitions of ^{87}Rb . To know whether the hollow beam had any effect on the VC-MOT (upper MOT), we also measured the number of atoms in the VC-MOT in the presence of the hollow beam after blocking the push beam. The observed variation of number of atoms in the VC-MOT with detuning of the hollow beam (for a power $\sim 28 \text{mW}$) is shown in Fig. 3.4.

The experimental results thus showed enhancement in the number of trapped atoms

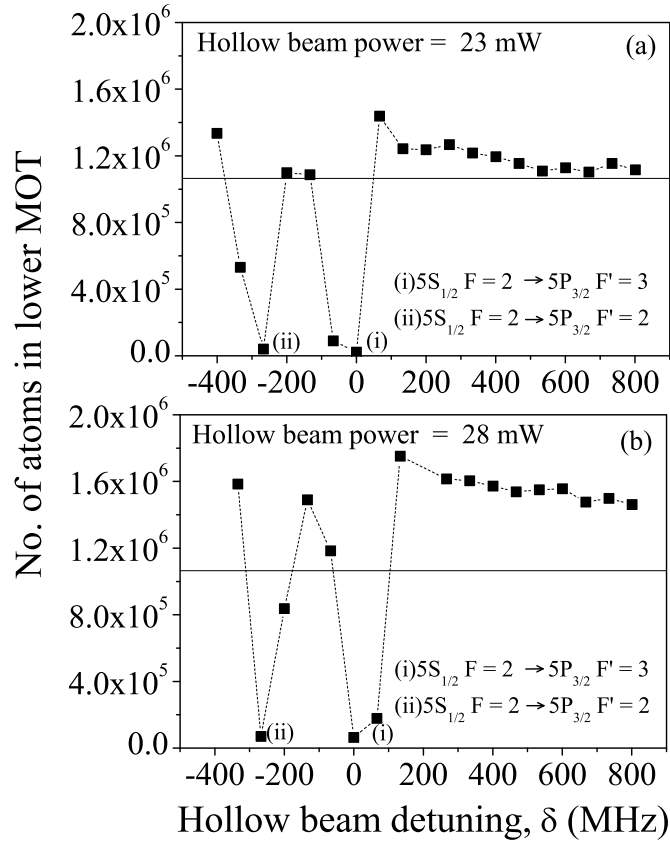


Figure 3.3: Measured variation of number of atoms in UHV-MOT (lower MOT) with detuning of hollow beam frequency; (a) at hollow beam power of 23 mW and (b) at hollow beam power of 28 mW. The squares show the measured values and dashed curves are for guiding the eye to the measured data. The horizontal lines show the number in the absence of hollow beam.

in both the MOTs in the presence of the hollow beam. In an earlier work on Cs-MOT [110], the increase in number of trapped atoms in the MOT due to presence of an auxiliary control beam aligned within the capture volume was reported. In this work, it was suggested that the enhancement was due to optical pumping by control beam among Zeeman sub-levels, which removed inaccessibility of atoms to the trapping beams occurring due to large Zeeman shifts at positions away from the MOT center. As the hollow beam diameter at VC-MOT was smaller (~ 3.2 mm) than the size of trapping region (~ 10 mm), we believe that similar optical pumping mechanism could be responsible for the increased number of atoms in the VC-MOT. In contrast to the results in [110], we observed the destruction of the atom cloud with very small number of atoms remaining there (see Fig. 3.4) when the hollow beam was resonant to the atomic transitions.

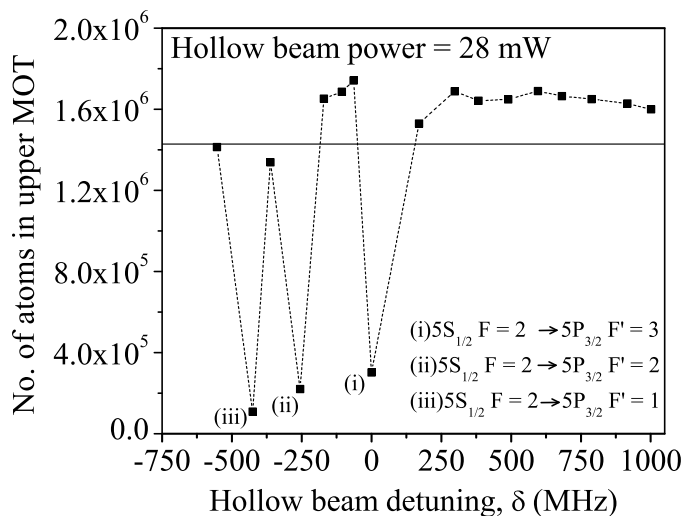


Figure 3.4: Variation of number of atoms in VC-MOT (upper MOT) with detuning of hollow beam frequency. The squares show the measured values and dashed curve is to guide eye to the measured data. The horizontal line shows the number in the absence of hollow beam.

The observed enhancement in the number of trapped atoms in the UHV-MOT could be partly a result of more trapped atoms in the VC-MOT but cannot be fully explained by this alone. Comparison of Fig. 3.3 and 3.4 shows that while the maximum enhancement for the VC-MOT was $\sim 28\%$, that for the UHV-MOT was $\sim 71\%$. Also, a mechanism similar to that responsible for more atoms in the VC-MOT is unlikely to be important for the UHV-MOT as the size of the hollow beam at the UHV-MOT (~ 14.3 mm diameter) was much larger than the trapping region diameter (~ 7 mm) of UHV-MOT. We believe that the observed additional enhancement for UHV-MOT could be a result of slowing down of atoms ejected from the VC-MOT by the counter-propagating hollow beam. A similar cooling mechanism was suggested to be responsible for the observed enhancement in a MOT loaded using a dark center slowing beam in a Zeeman slower setup by Miranda et al. [111]. We note that although the peak to peak intensity diameter (~ 3.2 mm) of the hollow beam at the VC-MOT position was much larger than the VC-MOT cloud size (~ 0.54 mm FWHM) there was finite intensity in the central region because of diffraction effects as can be seen from intensity profiles in Fig. 3.2. The destruction of VC-MOT by hollow beam resonant to atomic transition seems a result of this intensity profile. At the

push beam intensity of $\sim 10^3$ mW/cm² used in the experiments, the estimated scattering rate is $\sim 1.85 \times 10^7$ Hz and corresponding acceleration of atoms is $\sim 1.1 \times 10^5$ m/s². This acceleration is expected to act on atoms only up to a distance of 5 mm below the VC-MOT center because beyond this distance, the re-pumping beam ceases to exist so the atoms would be lost to the ($5S_{1/2} F = 1$) hyperfine ground state and would not scatter either the push beam or the hollow beam. Neglecting the VC-MOT trapping force, the action of above acceleration of push beam up to ~ 5 mm distance is expected to raise the speed of an atom to ~ 33 m/s, after ejection from VC-MOT. This speed is slightly higher than the estimated value of ~ 25 m/s for the capture velocity of the UHV-MOT [112]. Thus the atoms which have a speed greater than the capture velocity of UHV-MOT are unlikely to be trapped. In the presence of the hollow beam, however, these atoms can acquire a lower speed as a result of reduced net accelerating force due to presence of counter-propagating hollow beam. Hence the speed of ejected atoms from VC-MOT may reduce and atoms may be trapped in the UHV-MOT. It was also observed that for very low power of hollow beam (~ 0.6 mW), enhancement in the number of atoms in the UHV-MOT was observed only for some negative δ values which is consistent with the asymmetry of Doppler cooling process with respect to δ . This asymmetry was not evident from results shown in Fig. 3.3 for higher power in hollow beam. We believe that at higher powers in hollow beam, additional effects such as reduction in divergence of the atom flux because of finite transverse force associated with the converging hollow beam and transverse guiding of the ejected flux by hollow beam for positive detunings come into play, which enable more atoms to reach the capture volume of the UHV-MOT.

To summarize, a significant enhancement in the number of atoms in both the MOTs (VC-MOT and UHV-MOT) was observed for appropriate alignment of the hollow beam and for both negative and positive detunings of hollow beam frequency from the cooling transition of ⁸⁷Rb atoms. The observed enhancement in number of atoms was much larger for the UHV-MOT than that of VC-MOT, suggesting the increase in the transfer efficiency. The investigations have suggested that the increase was due to decrease in average speed of flux of atoms from VC-MOT as well as increase in number of atoms

reaching the capture volume of the UHV-MOT due to presence of hollow beam. The additional effect of the hollow beam on the atom flux from the VC-MOT could be the reduction in divergence of the flux because of transverse cooling and guiding effects of the beam.

3.3 Continuous versus pulsed push beam for atom transfer

In this section, we discuss the work performed to study the transfer of atoms from the VC-MOT to the UHV-MOT using the pulsed push beam and compare the observed results with the results obtained with the continuous push beam. We used a resonant push beam in four different forms (namely, (i) CW focused, (ii) CW unfocused, (iii) pulsed focused, and (iv) pulsed unfocused) and compared the results in terms of the numbers of atoms accumulated in the UHV-MOT. In these experiments, the UHV-MOT was formed continuously whereas the VC-MOT was formed continuously only when a CW push beam was used. In the experiments with pulsed push beam transfer, the VC-MOT was first loaded for a finite duration; then, a pulse of the push beam was applied on the VC-MOT cloud. By repetition of this, we transferred atoms from the VC-MOT to accumulate them in the UHV-MOT. We observed that the use of a pulsed and unfocused push beam on this unsaturated VC-MOT cloud in repetitive cycles resulted in a much higher number of atoms accumulated in the UHV-MOT than the number obtained either with a CW focused/unfocused push beam or with a pulsed and focused push beam. In the experiments with a pulsed and unfocused push beam, we have observed that the VC-MOT duration and the push beam duration, both parameters, have the optimum values to get the maximum number of atoms in the UHV-MOT. It turns out the pulsed atom transfer, implemented by making pulsed loading of VC-MOT and using subsequently pulsed push beam to eject atoms from the VC-MOT, can result several times enhancement in the number of atoms accumulated in the UHV-MOT as compared to the number in UHV-MOT obtained with CW resonant push beam. The processes affecting the number of

atoms accumulated in the UHV-MOT have also been investigated and discussed in this section.

3.3.1 Experimental Description

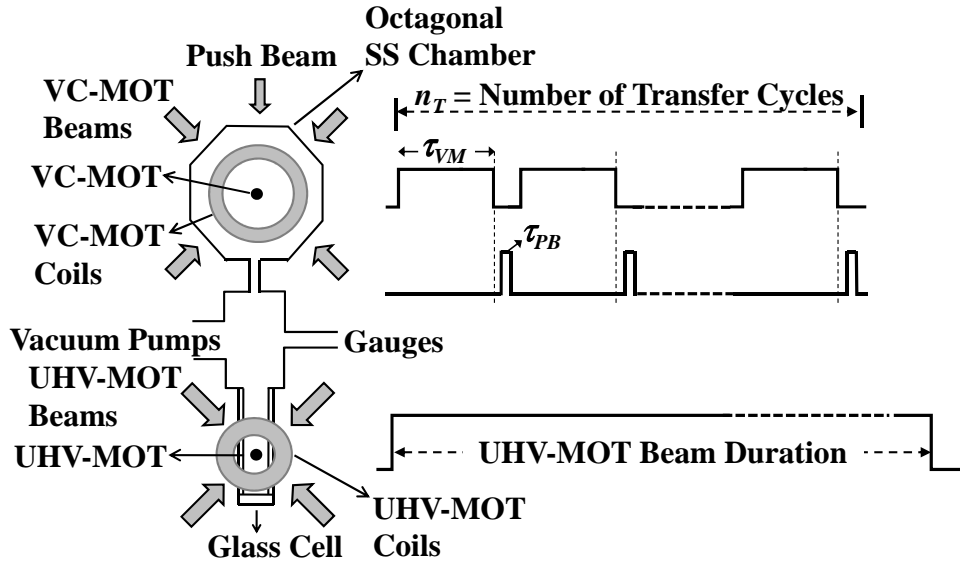


Figure 3.5: Schematic of the experimental setup and sequence of pulses for the pulsed push beam transfer scheme (τ_{VM} : duration of VC-MOT and τ_{PB} : push beam duration).

The experimental setup which has been used for these experiments is shown schematically in Fig. 3.5. In the experimental setup, the differential pumping tube (a narrow tube of 8 mm diameter and 70 mm length) was used in order to improve the differential vacuum between the chambers (10^{-8} in the VC-MOT chamber and 10^{-10} in the UHV-MOT chamber). Here also the cooling laser beams for both the MOTs were generated from two separate grating-controlled external cavity diode lasers whereas the re-pumping laser beams were obtained by dividing the output from a single laser of similar configuration. In order to make pulsed loading of VC-MOT, the VC-MOT cooling beam was first passed through two acousto-optic modulators (AOMs) to control its duration, then expanded and split into three beams (each having ~ 7 mW power and a $1/e^2$ radius of ~ 4 mm) that entered the chamber. After retro-reflection of each of these three beams, the desired six VC-MOT beams were obtained. The re-pumping laser beam for the VC-MOT (~ 9 mW power) was continuously ON and was mixed with one of the

three cooling beams entering the chamber. For the UHV-MOT, the cooling and the re-pumping beams were mixed and then the combined beam was passed through two AOMs to control the UHV-MOT duration. The output beam from the AOMs was expanded to a $1/e^2$ radius of ~ 5 mm and then divided into five UHV-MOT beams by using a sequence of half-wave plates and PBS elements. It was ascertained that all UHV-MOT beams had nearly the same power (~ 6 mW in each) in the cooling part. However, the powers in the re-pumping part in these beams could not be made equal due to different polarizations of the re-pumping and cooling laser beams required for mixing at the PBS. The total re-pumping power was ~ 12 mW in all the five beams. Four of these UHV-MOT beams were used as two pairs of counter-propagating beams incident at 45 degrees on the surface of the glass cell. This was done because a retro-reflection arrangement at this incidence angle would result in a large power difference between the forward propagating and the retro-reflected beams. The fifth beam, which was at normal incidence to the surface of the glass cell, was used in a retro-reflection arrangement to have the fifth and the sixth beams for the UHV-MOT. These vacuum and optical modifications in the setup as compared to the setup described in section 3.2.1 led to an improvement in the number of atoms in the VC-MOT as well as in the UHV-MOT.

Using SAS signals, the cooling lasers were locked at the side (~ 12 MHz to the red) of the $(5S_{1/2} F = 2) \rightarrow (5P_{3/2} F' = 3)$ transition of ^{87}Rb whereas the re-pumping laser was locked at the peak of the $(5S_{1/2} F = 1) \rightarrow (5P_{3/2} F' = 2)$ transition of ^{87}Rb . Appropriate polarizations of the beams were set by using quarter-wave retardation plates. Axial magnetic field gradients of ~ 12 G/cm and ~ 10 G/cm for the VC-MOT and the UHV-MOT were obtained using two separate pairs of quadrupole coils for both the MOTs. The push beam (maximum power ~ 4 mW) was obtained from a part of the VC-MOT cooling laser beam after shifting its frequency, by using two AOMs, to the peak of the $(5S_{1/2} F = 2) \rightarrow (5P_{3/2} F' = 3)$ transition of ^{87}Rb . The push beam was aligned vertically and propagated from the VC-MOT chamber to the UHV-MOT cell through differential pumping tube. By applying appropriate trigger pulses to these AOMs, the push beam could be made either pulsed or CW. In the experiments, we used a push

beam in four different forms, (i) CW focused, (ii) CW unfocused, (iii) pulsed focused, and (iv) pulsed unfocused to transfer atoms from the VC-MOT to the UHV-MOT. The maximum number of atoms that gets accumulated in the VC-MOT was $\sim 7 \times 10^7$ in ~ 1200 ms duration. This VC-MOT atom cloud was subjected to a push beam to eject the atoms to load the UHV-MOT. With the push beam switched-on, the VC-MOT cloud was deformed and the UHV-MOT cloud started growing. With the CW push beam at VC-MOT, the UHV-MOT attained saturation in ~ 30 seconds. With a pulsed push beam, the VC-MOT loading was done for a variable time duration τ_{VM} . Subsequent to VC-MOT loading, VC-MOT cooling beams were switched-off, and a pulsed push beam of duration τ_{PB} was applied to eject atoms from the VC-MOT cloud to load the UHV-MOT. This was repeated for a number of cycles (n_T) (as shown in Fig. 3.5) to accumulate atoms in the UHV-MOT which was continuously ON during n_T cycles of the atom transfer. We aligned the push beam in such a way that it was interacting with the VC-MOT cloud, but was leaving the UHV-MOT cloud aside.

3.3.2 Observation and results

First, we used a CW focused ($1/e^2$ radius $\sim 35 \mu\text{m}$ at VC-MOT cloud) push beam on the VC-MOT to transfer atoms to the UHV-MOT. The optimum power for this (CW focused) push beam was $\sim 150 \mu\text{W}$, and the corresponding number of atoms in the UHV-MOT is shown in Fig. 3.6 by a continuous horizontal line. This optimum power of the CW focused push beam is related to the velocity, as well as the magnitude, of the atom flux ejected by the push beam from the VC-MOT. At a power lower than the optimum value, the velocity is smaller, but less flux is ejected from the VC-MOT, which causes poor loading of the UHV-MOT. At a higher power, the flux may be more, but atoms are not captured in the UHV-MOT as the velocity exceeds the capture speed of the UHV-MOT.

When the push beam was CW and unfocused ($1/e^2$ radius of ~ 2.0 mm), the maximum number of atoms achievable in the UHV-MOT was very low compared to that obtained with CW focused push beam. This number, shown by the dashed horizontal line in Fig. 3.6, was obtained with $\sim 500 \mu\text{W}$ power of the push beam. At a higher power,

since an unfocused push beam covers a large VC-MOT volume, the atom cloud in the VC-MOT is not properly formed due to the presence of the push beam. At a lower power, an unfocused push beam is unable to eject a sufficient number of atoms from the VC-MOT, which results in a lower number being accumulated in the UHV-MOT. It may be important to mention here that a more collimated push beam imparts less transverse acceleration to atoms and that its use may result in more atoms taking trajectories straight downwards through the capture volume of UHV-MOT. Hence, a focused and collimated CW push beam should perform better than both the above forms of the push beam used here.

After these experiments with CW push beam, we employed the push beam in a pulsed and focused form with the pulse sequences as shown in Fig. 3.5. The number of atoms in UHV-MOT in this case was smaller than the maximum number of atoms observed with a CW focused push beam (shown by continuous horizontal line in Fig. 3.6). This was found to be valid for different combinations of the push beam intensity, pulse duration and number of transfer cycles (n_T) (for n_T up to 100). This observation is similar to the result of Cacciapuoti et al.[108] who observed a better loading of an UHV-MOT with a focused CW push beam than that observed with a focused pulsed push beam. With a pulsed push beam, it is desirable to switch-OFF the VC-MOT beams (to switch-OFF the trapping potential) so that trapped atoms can easily (at less intensity) escape the MOT volume. A focused push beam (due to its higher divergence) gives more transverse acceleration to VC-MOT atoms than an unfocused beam. Due to the absence of cooling MOT beams in the pulsed push beam case, this transverse acceleration remains with atoms and leads to a higher divergence of atom flux, resulting in less number of atoms reaching the UHV-MOT volume. Thus, a focused push beam in the pulse mode gives a lower number of atoms in the UHV-MOT than the number obtained with a focused CW push beam.

Finally, we used an unfocused ($1/e^2$ radius of ~ 2.0 mm) pulsed push beam with pulse sequences as shown in Fig. 3.5. We used the maximum available power of ~ 4 mW in the push beam (*i.e.*, maximum intensity of ~ 60 mW/cm²). The results of these

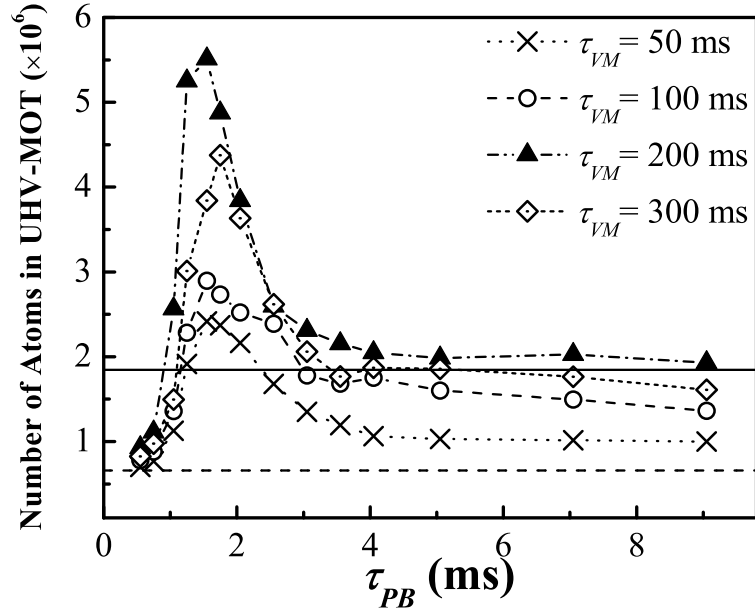


Figure 3.6: Variation in number of atoms in the UHV-MOT with τ_{PB} (duration of the unfocused push beam) for different VC-MOT loading durations τ_{VM} . The continuous horizontal line and dashed line show the numbers of atoms in the UHV-MOT for a focused CW push beam and an unfocused CW push beam, respectively, both with optimized powers.

measurements with an unfocused pulsed push beam are shown in Fig. 3.6, which shows that the maximum number of atoms achieved with this scheme was much higher than the number obtained with a CW focused push beam of optimum power. The data in Fig. 3.6 shows the number of atoms accumulated in the UHV-MOT as a function of the unfocused push beam pulse duration (τ_{PB}) for different values of the VC-MOT duration (τ_{VM}). For the data in Fig. 3.6, we kept $n_T = 100$ (number of transfer cycles) for each combination of τ_{PB} and τ_{VM} . As is evident from Fig. 3.6, the number of atoms in the UHV-MOT was dependent on the push beam duration (τ_{PB}) as well as on the VC-MOT duration (τ_{VM}). For certain optimum values of these parameters, the number of atoms in the UHV-MOT was enhanced up to ~ 3 times the number we obtained with the focused CW push beam of optimized power (refere Fig. 3.6).

This enhancement in the number of atoms in the UHV-MOT was achieved with a unfocused pulsed push beam (Fig. 3.6) can be understood to be a result of the following factors. First, a smaller divergence of the unfocused beam results in a more collimated atom flux, which results in a higher number of atoms reaching the UHV-MOT volume.

Second, the unfocused push beam interacts with nearly the entire VC-MOT cloud and pushes a larger number of atoms to the UHV-MOT than a focused push beam. Also, in the pulsed mode transfer, the VC-MOT loading is not hindered by the push beam.

The observed optimum for the push beam duration ($\tau_{PB} \sim 1.75$ ms for a peak intensity ~ 60 mW/cm²) in Fig. 3.6 can be correlated to the value of the velocity acquired by atoms (*i.e.* transfer velocity) due to the push beam impulse in comparison to the capture velocity of UHV-MOT. The optimum τ_{PB} corresponds a transfer velocity nearly equal to the capture velocity of the UHV-MOT [113]. For smaller τ_{PB} (or lower transfer velocity), a lower number reaches the capture volume of the UHV-MOT due to loss of atoms in the transverse direction during the transit. On the other hand, for larger τ_{PB} values, the transfer velocity becomes higher than the capture velocity of the UHV-MOT, and atoms are not captured in the UHV-MOT volume.

Another important parameter in these experiments with pulsed unfocused push beam transfer (results shown in Fig. 3.6) is the duration of the VC-MOT (τ_{VM}). The VC-MOT duration τ_{VM} also governs the number of atoms accumulated in the UHV-MOT. In the experiments, we obtained the largest number in the UHV-MOT for $\tau_{VM} = 200$ ms, as shown in Fig. 3.6. We have investigated this dependence of number of atoms in the UHV-MOT on τ_{VM} in more detail, as described below.

For a smaller value of τ_{VM} (< 200 ms), the relatively smaller number of atoms obtained in UHV-MOT seems to be due to the smaller number of atoms loaded in the VC-MOT over the duration τ_{VM} . But for larger values of τ_{VM} (> 200 ms), for which the number of atoms collected in VC-MOT is larger than that for $\tau_{VM} = 200$ ms, the observed smaller number in the UHV-MOT may be attributed to the higher temperature of the VC-MOT atoms. It has been reported earlier [79] that before the saturation of a VC-MOT cloud, the temperature of the atoms collected in the MOT increases with increasing loading duration. To reconfirm this, we have also measured the temperature of the VC-MOT atom cloud as function of its loading duration τ_{VM} , and the results are shown in Fig. 3.7. It is evident that a larger τ_{VM} (in the region 200 ms $< \tau_{VM} < 1000$ ms) in our experiments implies a higher temperature of the VC-MOT cloud. A higher temperature of the VC-

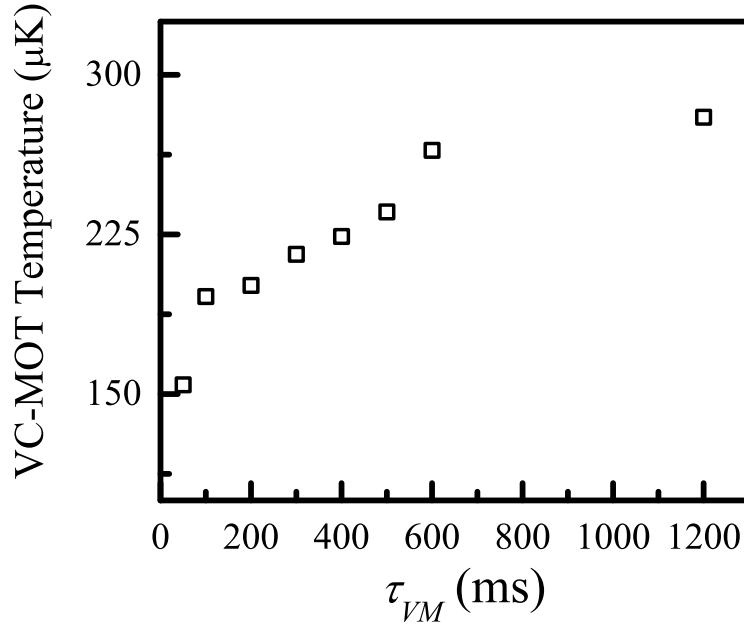


Figure 3.7: The measured variation in temperature of the VC-MOT cloud with VC-MOT loading duration (τ_{VM}).

MOT atoms would result in a larger transverse divergence of the atom flux and, hence, a smaller number of atoms captured in the UHV-MOT. Considering such a dependence of number and temperature in VC-MOT atom cloud on τ_{VM} , an optimum value of τ_{VM} would lead to the maximum number of atoms accumulated in UHV-MOT. This explains our experimental results in Fig. 3.6 qualitatively.

Further, due to the finite lifetime \sim few seconds at 10^{-10} Torr of the UHV-MOT, a larger τ_{VM} also results in a larger number of atoms lost from the UHV-MOT during two consecutive loadings of the UHV-MOT in the pulsed mode of atom transfer. This is in addition to the loss process associated with the VC-MOT-temperature dependent divergence of the atom flux. Thus, for larger values of τ_{VM} , a smaller saturated value of number of atoms in the UHV-MOT is expected.

To summarize; experiments have been performed using a push beam in different forms, (i) CW focused, (ii) CW unfocused, (iii) pulsed focused, and (iv) pulsed unfocused to transfer atoms from a VC-MOT to an UHV-MOT. It has been found that use of a pulsed and unfocused push beam on an unsaturated VC-MOT cloud results in a larger number of atoms accumulated in the UHV-MOT than the number obtained by using the push beam

in other forms. We have also investigated the dependence of the number of atoms in the UHV-MOT on parameters such as the push beam duration and the VC-MOT duration in the pulsed transfer scheme, and the observed results have been explained qualitatively.

3.4 Summary

This chapter describes our experiments and corresponding results on the use of a resonant push beam for the transfer of cold atoms between two MOTs. The results have shown that use of a counter-propagating hollow beam in conjunction with the push beam can result in higher number of atoms transferred from the VC-MOT to the UHV-MOT in the double-MOT setup. Also, using a resonant push beam in pulsed and unfocused form results in higher number of atoms transferred from one MOT to another MOT. For further details, our paper [\[62\]](#) and [\[63\]](#) can be referred.

Chapter 4

Atom transfer with red-detuned push beam

4.1 Introduction

The detuning of a laser beam with respect to the atomic resonance frequency governs, whether an atom will be pushed towards the higher intensity (for red-detuned) or towards the lower intensity (for blue-detuned). This behaviour arises due the dipole force [114, 115] experienced by the atoms. Several groups [116–124] have used this property for guiding of ultra-cold atoms. A far red-detuned laser (Nd:YAG laser) was employed [119, 120] for guiding of cold Rb atoms. The guiding improves the efficiency in decreasing the transverse temperature during transfer of atoms from one position to another position. Therefore it seems beneficial, if the guiding of atoms can be coupled with the atom transfer between two MOTs using a push beam [107, 108, 125]. Dimova et al. [126] has proposed and demonstrated a technique which used the pushing and guiding of atoms during the transfer of atoms from one MOT to another in a double-MOT setup.

We have proposed and demonstrated that a single beam of sufficiently high power (few tens of mW) and with detuning in the order of few GHz to the red of atomic resonance transition can be used not only for generating a leak in the VC-MOT for extraction of atoms for transfer to UHV-MOT but also for guiding the atoms to the trapping volume

of UHV-MOT to loaded UHV-MOT. In this chapter we discuss our studies on the atom transfer process using such a red-detuned push beam [63, 74]. Since guiding is intensity dependent process we have investigated the benefits of using a red-detuned push beam in retro-reflection geometry which enhances the guiding potential of the beam [63]. Further extension in the study of atom transfer with red-detuned push beam was made towards the investigation of the effect of variation in the push beam spot-size at VC-MOT on number of atoms accumulated in UHV-MOT [74]. The description of these studies is presented as follows.

4.2 Use of a red-detuned push beam in retro-reflection geometry

After getting motivation from work in ref [126, 127], we studied the use of a red-detuned push beam for atom transfer between two MOTs in a double MOT setup. We observed that a red-detuned push beam resulted in much higher number of atoms in UHV-MOT after the transfer of ^{87}Rb atoms from VC-MOT. Using this red-detuned push beam in the retro-reflection geometry, a further increase in number of atoms in UHV-MOT was observed.

4.2.1 Experimental setup for push beam in retro-reflection geometry

The experimental arrangement for use of push beam in retro-reflection geometry is shown schematically in Fig. 4.1. During these experiments, the differential pressure between two chambers were 1×10^{-8} and 6×10^{-11} Torr in VC-MOT and UHV-MOT chambers respectively. This pressure difference was maintained by using a differential pumping tube of length 122 mm (upperpart: length = 67 mm and diameter = 3.75 mm, lower part: length = 55 mm and diameter = 5 mm). The cooling beams for both the MOTs were generated from a ~ 1 W power, ECDL system (*Sacher, Tiger series*). With this

high power laser, the total power in VC-MOT beams and UHV-MOT beams could be boosted to ~ 60 mW and ~ 90 mW respectively.

We have generated the push beam from a separate grating controlled ECDL. In these experiments, the push beam was first expanded to $1/e^2$ radius of ~ 2 mm and then focused on the VC-MOT using a lens of focal length ~ 300 mm to a spot radius ($1/e^2$ radius) of ~ 35 μm to eject a flux of atoms from VC-MOT cloud to load UHV-MOT (formed at ~ 360 mm below the VC-MOT). The frequency of the push beam was varied by adjusting the piezo voltage supplied to the grating in the laser to obtain the desired value of push beam detuning ($\delta/2\pi$) with respect to $(5S_{1/2} F = 2) \rightarrow (5P_{3/2} F' = 3)$ transition of ^{87}Rb . We used a $\sim 100\%$ reflectivity mirror at a distance ‘ d ’ from the UHV-MOT center to retro-reflect the push beam as shown in Fig. 4.1. The number of atoms in the MOTs were estimated by the fluorescence imaging technique described in 2.6.1.

4.2.2 Results on atom transfer with push beam in retro-reflection geometry

During these experiments, we typically obtained $\sim 7 \times 10^7$ atoms in the VC-MOT with a loading time of ~ 1.2 s. This enhanced number in the VC-MOT as compared to our earlier experiments was due to increased power and area of VC-MOT beams. The UHV-MOT beams power and area were also increased in these experiments to allow a higher number captured in the UHV-MOT. To transfer atoms from VC-MOT to UHV-MOT, simultaneously the VC-MOT, the push beam and the UHV-MOT were kept alive for 60 s duration. The push beam was switched-off ~ 0.3 ms before flashing the probe beam pulse on UHV-MOT cloud for measurement of number of atoms by fluorescence method. With push beam resonant to $(5S_{1/2} F = 2) \rightarrow (5P_{3/2} F' = 3)$ transition of ^{87}Rb , the maximum number of ^{87}Rb atoms obtained in UHV-MOT was $\sim 3.5 \times 10^7$ for an optimum push beam power of ~ 500 μW . At push beam power lower or higher than this value, the number of atoms in UHV-MOT was smaller. At lower power (< 500 μW), the push beam force on VC-MOT atoms was smaller which results in lower speed and smaller magnitude of atom flux was ejected from VC-MOT. This consequently results in smaller number of

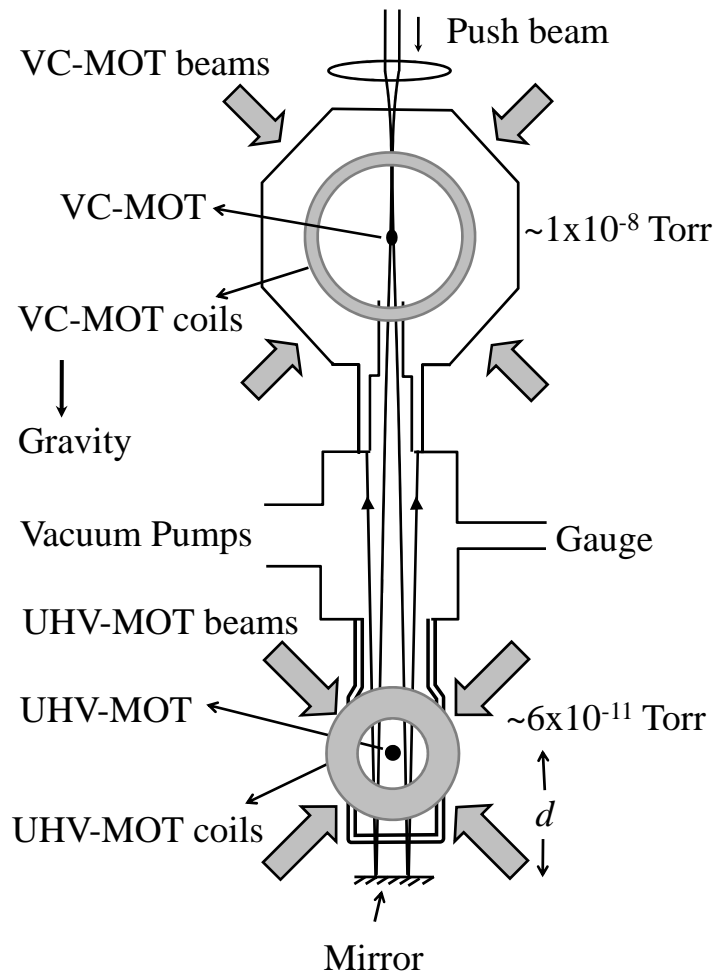


Figure 4.1: Schematic of the experimental setup. Here ‘ d ’ is the separation between UHV-MOT center and push beam retro-reflecting mirror.

atoms reached and captured in the UHV-MOT. At push beam power higher than the optimum value, the speed of atoms ejected from VC-MOT becomes comparable or higher than the capture speed of UHV-MOT, hence smaller number of atoms was captured in UHV-MOT.

When we used the push beam with its frequency red-detuned from the cooling transition of ^{87}Rb ($5S_{1/2} F = 2 \rightarrow 5P_{3/2} F' = 3$), we observed an increase in number of atoms in UHV-MOT with increasing push beam power. With maximum available power of ~ 21 mW of push beam at VC-MOT position and detuning of $\delta/2\pi \sim -1.1$ GHz, the number of atoms accumulated in UHV-MOT could be enhanced to ~ 4 times ($\sim 1.5 \times 10^8$ atoms) the number obtained ($\sim 3 \times 10^7$ atoms) with the resonant push beam of the optimum power. At this power of push beam, the measured variation in number

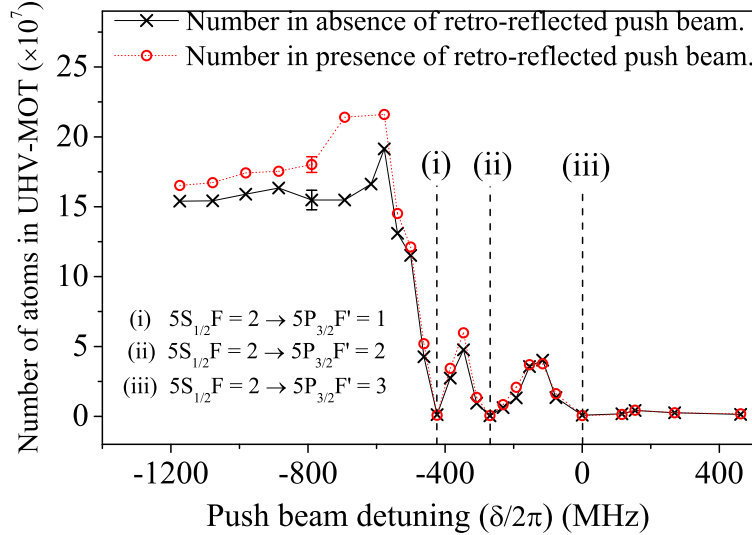


Figure 4.2: Observed variation in number of atoms in UHV-MOT with push beam frequency detuning $\delta/2\pi$ from $(5S_{1/2} F = 2) \rightarrow (5P_{3/2} F' = 3)$ transition of ^{87}Rb for push beam power of ~ 21 mW and $d = 135$ mm. Characteristic error bars determined from scatter in the values obtained in repeated measurements are shown for some data points.

of atoms in UHV-MOT with push beam detuning is shown in Fig. 4.2. At this level of push beam power, both the MOT clouds were completely destroyed when push beam frequency was resonant to atomic transition (which is also evident from data in Fig. 4.2). But when push beam frequency was detuned from transition frequency, the clouds in VC-MOT and UHV-MOT were revived. For push beam frequency detuned to far red from cooling transition ($\delta/2\pi < -400$ MHz), the number in UHV-MOT was increased rapidly (crosses in Fig. 4.2) and reached to a value $\sim 1.5 \times 10^8$ for $\delta/2\pi < -600$ MHz. We attribute this increased number in UHV-MOT with red-detuned push beam, as compared to number with resonant push beam, to transverse guiding of atoms by red-detuned push beam during the atom transfer from VC-MOT to UHV-MOT.

Since guiding dipole potential is intensity dependent, one can enhance the above guiding assisted transfer by using the push beam of a given power in retro-reflection geometry, where retro-reflected push beam potential was added (with appropriate sign) to the potential of the forward push beam to give the resultant higher guiding potential. At the same time, the destructive scattering force of forward push beam at UHV-MOT was balanced by that of the retro-reflected push beam. Therefore, we repeated the UHV-MOT number vs detuning measurements for push beam employed in retro-reflection geometry

by keeping a maximum reflectivity mirror in the push beam path. The observed results are shown by circles in Fig. 4.2 for $d \sim 135$ mm. As is evident from Fig. 4.2 that for large negative values of $\delta/2\pi$, the number in UHV-MOT (circles in Fig. 4.2) was always higher for push beam in retro-reflection geometry than the number obtained without retro-reflection of push beam (crosses in Fig. 4.2). In measurements of number of atoms in UHV-MOT by fluorescence method, we had switched-OFF push beam before the fluorescence excitation probe beam pulse to ascertain that push beam did not contribute to the fluorescence signal from the UHV-MOT atoms.

Here we note that during the transit from VC-MOT to UHV-MOT, atoms are likely to be pumped to lower hyperfine ground state ($5S_{1/2} F = 1$) because of interaction with the push beam in absence of re-pumping laser. Thus push beam, due to very large frequency detuning from ($5S_{1/2} F = 1$) ground state (> 6.8 GHz) could provide very weak transverse of guiding atoms for rest of the path from VC-MOT to UHV-MOT. As atoms reach the UHV-MOT volume, where re-pumping beams are present, atoms are pumped back to higher hyperfine ground state ($5S_{1/2} F = 2$) and guiding dipole potential and scattering force of push beam again become important. Thus we believe that guiding dipole potential and scattering force of retro-reflected push beam play an important role within the UHV-MOT volume only. At VC-MOT position, intensity of retro-reflected push beam is much smaller than that of forward push beam.

We have also estimated the modifications in the push beam dipole potential and scattering force on atoms at UHV-MOT position when push beam is used in retro-reflection geometry. For this we calculated dipole potential and scattering force [114, 115, 128] due to forward push beam and its retro-reflected beam separately, and obtained their resultant by adding those with appropriate sign.

The dipole potential was calculated using the expression,

$$U_d = \sum_{F=2}^{F'=1,2,3} \frac{\hbar\delta_{F'}}{2} \ln \left[1 + \frac{I/I_{FF'}}{1 + 4\delta_{F'}^2/\Gamma^2} \right], \quad (4.1)$$

where I is intensity of push beam, $I_{FF'} (= c\epsilon_0\Gamma^2\hbar^2/4|d_{FF'}|^2)$ is the saturation intensity, Γ is line-width of the transition and $d_{FF'}$ is the effective dipole moment and $\delta_{F'} = \omega_L - \omega_{FF'}$

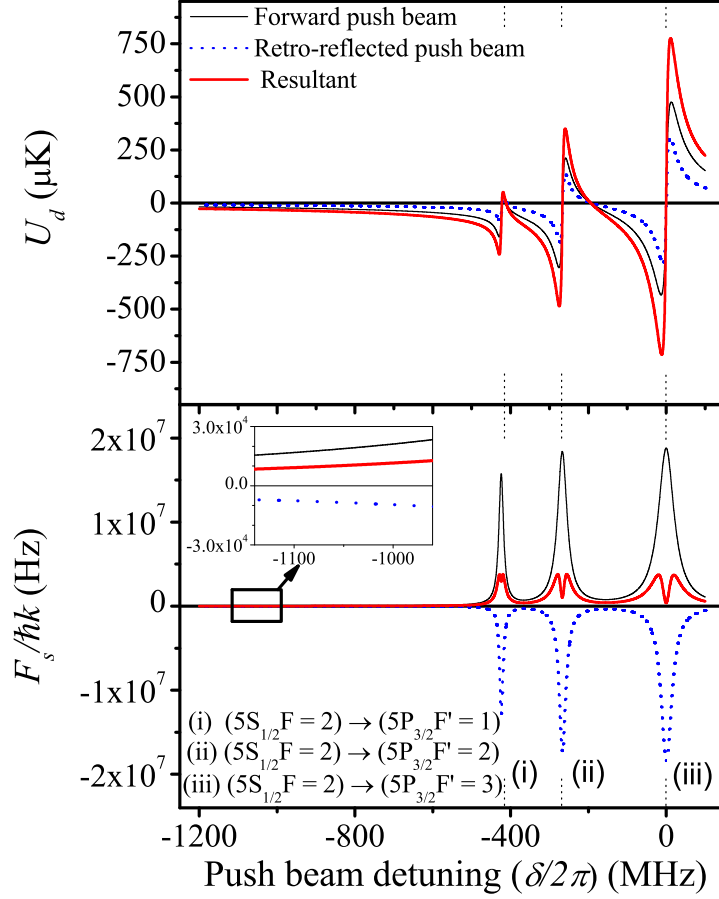


Figure 4.3: Calculated variation of dipole potential and scattering force at UHV-MOT centre with push beam frequency detuning ($\delta/2\pi$) (from cooling transition peak of ^{87}Rb) for a fixed push beam power of ~ 21 mW and $d = 135$ mm. Here resultant denotes the sum of dipole potentials (scattering forces) due to forward and retro-reflected beams with appropriate sign.

with ω_L being the push beam laser frequency and $\omega_{FF'}$ being the resonance frequency for $(5S_{1/2}, F = 2) \rightarrow 5P_{3/2}, F'$ transition of ^{87}Rb .

The scattering force (\vec{F}_s) was calculated using the expression,

$$\vec{F}_s = \hbar \vec{k} \frac{\Gamma}{2} \sum_{F=2}^{F'=1,2,3} \frac{I/I_{FF'}}{1 + I/I_{FF'} + 4\delta_{F'}^2/\Gamma^2}, \quad (4.2)$$

where \vec{k} is the wave vector of the beam.

Fig. 4.3 shows the calculated dipole potential (U_d , using equation (4.1)) and scattering force (F_s using equation (4.2)) for different detuning ($\delta/2\pi$) values of push beam frequency from the cooling transition of ^{87}Rb for a power of 21 mW and mirror position $d = 135$ mm. As expected, U_d was increased in the presence of retro-reflected push beam due to

increased total intensity. A detuning of $\sim 1\text{GHz}$, the value of U_d increases from $21\ \mu\text{K}$ to $33\ \mu\text{K}$. Thus it can target atoms with temperature upto $33\ \mu\text{K}$ to guide them from VC-MOT to UHV-MOT. Hence, the push beam can confine more atoms in the flux from the VC-MOT to the UHV-MOT in the presence of retro-reflected beam. On the other hand, the resultant scattering force in presence of retro-reflected push beam is reduced because of opposite directions of forces due to forward and retro-reflected components of push beam. This reduced scattering force and increased dipole potential due to push beam is likely the cause of observed higher number in UHV-MOT for push beam in retro-reflection geometry than the number observed without retro-reflection of push beam.

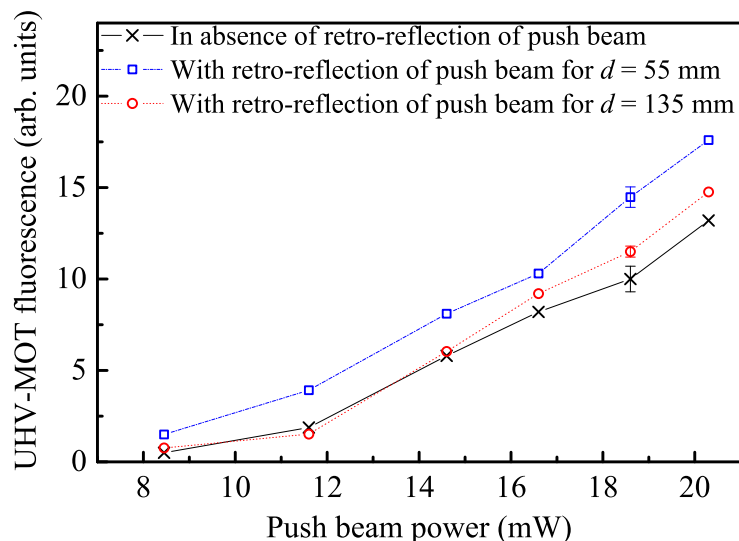


Figure 4.4: Measured variation in UHV-MOT fluorescence with input push beam power at fixed push beam frequency detuning of $\delta/2\pi = -1.1\text{ GHz}$ from the cooling transition of ^{87}Rb . Squares and circles show data obtained with retro-reflected push beam for $d = 55\text{ mm}$ and 135 mm respectively, whereas crosses show data without retro-reflection of push beam. Characteristic error bars determined from scatter in the values obtained in repeated measurements are shown for some data points.

To further investigate the effect of retro-reflection of push beam on UHV-MOT number, the distance d of retro-reflecting mirror was varied and variation in number of atoms in UHV-MOT in presence of retro-reflected push beam was observed. For these measurements fluorescence signal from UHV-MOT (proportional to number of atoms in UHV-MOT) was recorded for different values of push beam power for $d = 135\text{ mm}$ and $d = 55\text{ mm}$ (Fig. 4.4). In these measurements the push beam detuning was kept at $\delta/2\pi \sim -1.1\text{ GHz}$. As compared to without retro-reflection of push beam, the increase in num-

ber of atoms in UHV-MOT in presence of its retro-reflection is evident in Fig. 4.4. As expected, this increase in number was higher for smaller value of d (Fig. 4.4). Because of the divergence of push beam, a smaller value of d results into higher intensity of the retro-reflected beam at UHV-MOT position. The higher intensity of the retro-reflected beam provides a higher resultant dipole potential and lower resultant scattering force of the push beam at UHV-MOT atom cloud, both favorable for higher number of atoms in the UHV-MOT. As compared to without retro-reflected push beam, for push beam power of ~ 20 mW, ~ 30 % increase in number in UHV-MOT for $d = 55$ mm and ~ 10 % increase in number for $d = 135$ mm was observed in presence of retro-reflected push beam (Fig. 4.4).

At push beam power of 21 mW and detuning of $\delta/2\pi \sim -1.1$ GHz, the calculated speed of atom flux is comparable to the capture speed for our UHV-MOT (~ 28 m/s). Further, a red-detuned push beam in retro-reflected geometry has proved to be more advantageous due to increased transverse guiding potential and reduced scattering force at UHV-MOT due to retro-reflected part of the push beam.

In summary a red-detuned push beam has proved to be advantageous to accumulate a large number of atoms in the UHV-MOT as compared to a resonant push. The advantage with a red-detuned push beam is its ability to guide atom flux from VC-MOT to UHV-MOT and less destructive force on UHV-MOT.

4.3 Dependence of red-detuned push beam spot-size on atom transfer

In this work, the effect of push beam spot-size and power on the number of atoms accumulated in the UHV-MOT has been studied during the atom transfer from the VC-MOT to UHV-MOT. It has been observed that, at a given push beam power, the number of atoms collected in the UHV-MOT varies with the push beam spot-size at the VC-MOT and attains a maximum value at an optimum push beam spot-size. At a given push beam power, the number of atoms accumulated in the UHV-MOT and the optimum push beam

spot-size are dependent on the capture speed of the UHV-MOT.

4.3.1 The description of the experimental setup

For the studies on push beam spot-size dependent atom transfer, the experiments were performed using the setup as shown in Fig. 4.1 (without using retro-reflection mirror). Here for the cooling laser beams, we used a 1 W-Tapered-Amplifier (BOOSTA, Toptica, Germany) operated at ~ 750 mW power after seeding it with an ECDL. For the formation of VC-MOT, three beams (each of cooling power ~ 19 mW and size ~ 6 mm ($1/e^2$ radius)) were used in retro-reflection geometry. Whereas, for the formation of UHV-MOT, six independent beams (each of cooling power ~ 10 mW and size ~ 8 mm ($1/e^2$ radius)) were used. More details of the VC-MOT, UHV-MOT and their formation are described in Chapter 2.

The push beam was obtained from an independent ECDL system and its frequency was kept fixed and red-detuned by a value -1.0 GHz with respect to ($5S_{1/2} F = 2$) \rightarrow ($5P_{3/2} F' = 3$) transition frequency of ^{87}Rb atom. The push beam was first expanded to $1/e^2$ -radius of ~ 2 mm and then focused to a spot-size ~ 35 μm ($1/e^2$ radius) using a ~ 300 mm focal length lens kept outside the VC-MOT chamber. The push beam was focused before the VC-MOT position and its spot-size on the VC-MOT was varied by translating the focusing lens. The centre to centre separation between VC-MOT and UHV-MOT was ~ 360 mm. This resulted, typically, the push beam spot-size values 2.5-2.6 mm at the UHV-MOT, 570 -700 μm at the end of 2.25 mm diameter differential pumping and transfer tube, when the push beam spot-size values at VC-MOT were varied over the range 80-200 μm . In these experiments, the UHV-MOT was loaded for 60 s duration over which the push beam was kept on. After choosing the parameters appropriately in the setup, we could obtain $\sim 1 \times 10^8$ ^{87}Rb atoms in the VC-MOT and $\sim 1 - 2 \times 10^8$ atoms in the UHV-MOT.

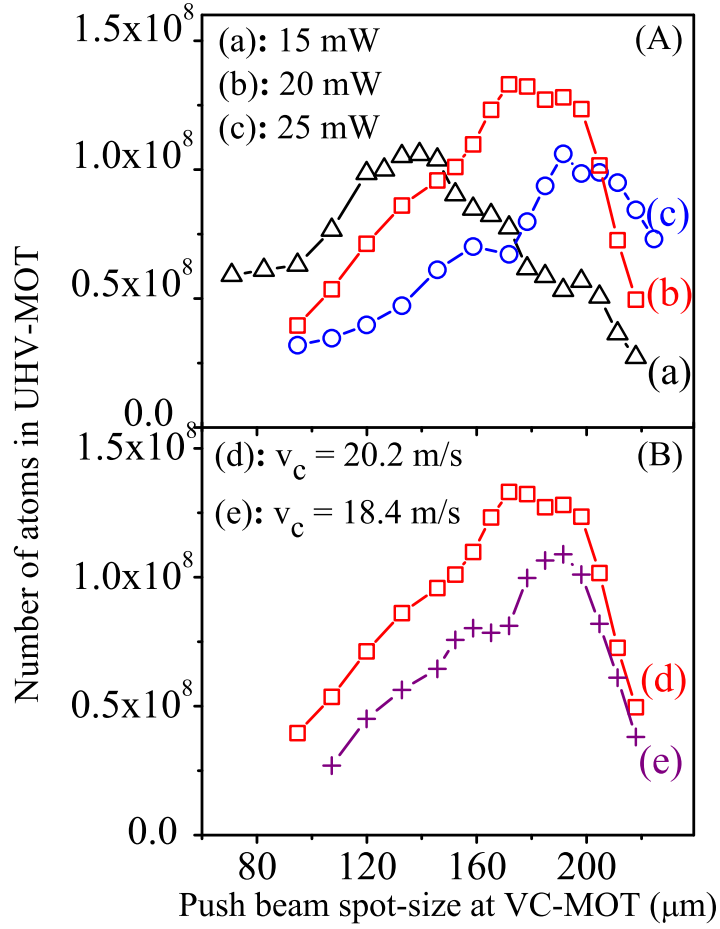


Figure 4.5: (A) Measured variation in number of atoms in UHV-MOT (capture speed $v_c = 20.2$ m/s) with push beam spot-size for different powers in push beam; (a): 15 mW, (b): 20 mW and (c): 25 mW. (B) Measured variation after modifying the v_c for UHV-MOT to 18.4 m/s (curve (e)), for a push beam power of 20 mW. For comparison, the data of curve (b) in (A) with higher v_c value ($= 20.2$ m/s) is replotted as curve (d) in (B).

4.3.2 Results on push beam spot-size dependent atom transfer

The results of measurement of the number of atoms accumulated in the UHV-MOT for different values of push beam power and spot-size at the VC-MOT are shown in Fig. 4.5(A). It is evident from Fig. 4.5(A) that at a given power in the push beam, the number of atoms accumulated in the UHV-MOT first increases with the push beam spot-size and then decreases with it, after attaining a maximum value. It is also evident from Fig. 4.5(A) that with a higher power in the push beam, the peak in the number of

atoms in the UHV-MOT appears at a larger value of push beam spot-size. The intensity values for the push beam at the VC-MOT corresponding to three peaks in Fig. 4.5(A) (for three different values of push beam power) are nearly equal. However, the height of peaks in Fig. 4.5(A) is different for different powers in the push beam. This suggests that, not alone the push beam intensity but also the push beam spot-size and power together govern the transfer of atoms from VC-MOT to UHV-MOT. The experimental observations shown in Fig. 4.5(A) can be explained by taking into account the effect of the push beam parameters (e.g. power, spot-size and intensity) on the speed of atoms ejected from the VC-MOT and on the rate of number of atoms reaching the UHV-MOT capture volume, as discussed in the following.

The scattering force on the VC-MOT atoms due to the push beam can be estimated from equation (4.2). Knowing the magnitude of scattering force (F_s), the speed of an atom in the flux ejected from the VC-MOT is given as $v = \sqrt{(2sF_s/m)}$, where m is the mass of ^{87}Rb atom and s is the distance over which the force given by equation (4.2) is effective on the VC-MOT atoms. It may be noted that atoms once ejected out of the VC-MOT volume were pumped to the lower hyperfine ground state ($5S_{1/2} F = 1$) due to scattering with the push beam in the absence of re-pumping laser beam. Thus force given by equation (4.2) will not remain effective on the ejected atom flux. For an atom with initial average position at the centre of VC-MOT, we can approximately take s as $1/e^2$ radius of the VC-MOT re-pumper beam. Using this value of s (~ 5 mm), and F_s as given by equation (4.2), the speed of an atom ejected from VC-MOT was estimated. The variation in this speed with the push beam spot-size is shown in Fig. 4.6. It can be noted here that atoms can have different initial positions with respect to the centre of VC-MOT, which results in a distribution in the values of distance s and finally in speed v . This was ignored in the calculations shown in Fig. 4.6. It was also checked that the VC-MOT trapping force and gravitational force (mg) make a negligible correction to the speed v shown in Fig. 4.6. It is also important to note that the longitudinal dipole force of the push beam due to intensity gradient along the beam axis is much smaller than the scattering force experienced by the atoms in ($5S_{1/2} F = 2$) or ($5S_{1/2} F = 1$) states, for

the detuning and intensity of push beam used in the experiments. The horizontal line in Fig. 4.6 shows the capture speed for UHV-MOT (v_c) which was estimated using the experimental parameters [112, 129]. This value of capture speed ($v_c = 20.2$ m/s) is for our regular UHV-MOT for which the measured number of atoms is shown in Fig. 4.5(A).

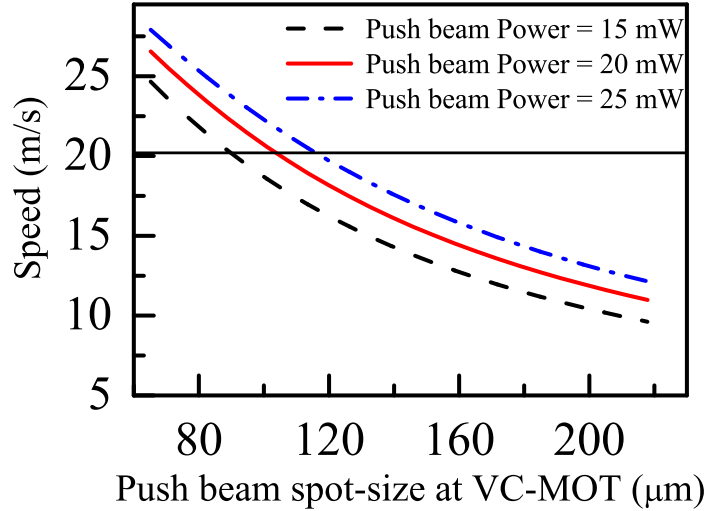


Figure 4.6: Calculated variation in speed of an atom ejected from the VC-MOT with push beam spot-size for different values of push beam power. The continuous horizontal line shows the estimated capture speed of UHV-MOT ($v_c = 20.2$ m/s).

At a given power of the push beam, a smaller spot-size corresponds to higher intensity and higher speed of atoms in the flux ejected from the VC-MOT (Fig. 4.6). When speed of an atom ejected from the VC-MOT becomes higher than the capture speed of UHV-MOT, it is not captured in the UHV-MOT. Hence the number of atoms accumulated in the UHV-MOT is sensitive to the speed of atoms ejected from VC-MOT (which is controlled by intensity of push beam at VC-MOT). Another parameter which governs the number of atoms accumulated in UHV-MOT is the rate of number of atoms reaching the UHV-MOT. This is governed by spot-size and power of push beam at VC-MOT and other effects such as guiding of atoms or losses due to transverse expansion of flux by push beam or VC-MOT temperature. Considering these two together, the rate of number of atoms reaching the UHV-MOT and having speed lower than the capture speed (v_c) governs the number of atoms accumulated in the UHV-MOT.

In the regime of very small push beam spot-size (spot-size < 140 μm in the measurements shown in Fig. 4.5(A)), the push beam intensity is high enough to provide the

VC-MOT atoms a speed comparable to (or higher than) the capture speed of UHV-MOT. Therefore, at these push beam intensities, only a fraction of the atom flux from VC-MOT may have the speed lower than the capture speed. This fraction decreases with decrease in the push beam spot-size, as decrease in the spot-size results in increase in speed of atoms at a given push beam power (Fig. 4.6). Thus the number of atoms accumulated in UHV-MOT is expected to decrease with the decrease in push beam spot-size at a given push beam power, as is observed experimentally (Fig. 4.5(A)). For the same reason, the number of atoms in UHV-MOT is expected to decrease with increase in push beam power at a given push beam spot-size, which is in agreement with the observed data shown in Fig. 4.5(A) for this regime of spot-size.

In order to establish that, the number of atoms accumulated in the UHV-MOT is indeed governed by the speed of atoms from VC-MOT relative to the capture speed of UHV-MOT, we changed the capture speed of UHV-MOT and repeated the measurements. The capture speed of the UHV-MOT was reduced by reducing the size of the cooling beams of UHV-MOT. With the reduced capture speed of UHV-MOT ($v_c = 18.4$ m/s), the observed variation in the number of atoms in the UHV-MOT with push beam spot-size at the VC-MOT is shown in Fig. 4.5(B) graph (e). We used 20 mW of power in the push beam in the data shown in Fig. 4.5(B) graph (e). For comparison purpose, the data of curve (b) in Fig. 4.5(A) for 20 mW push beam power with $v_c = 20.2$ m/s is replotted as curve (d) in Fig. 4.5(B). It is evident from Fig. 4.5(B) that for the lower value of v_c ($= 18.4$ m/s), the number of atoms in UHV-MOT was lower than that observed for higher value of v_c ($= 20.2$ m/s). Also, as is shown in Fig. 4.5(B), the peak in the number of atoms for the lower v_c of VC-MOT value was observed at a larger spot-size of the push beam (i. e. at a lower speed of atoms in the flux from VC-MOT). These observations clearly show that the number of atoms in the UHV-MOT is dependent on the UHV-MOT capture speed as well as on the speed of atoms in the flux from the VC-MOT.

Here we note that, when the size of UHV-MOT beams is reduced to reduce its capture speed, the capture volume of UHV-MOT is also reduced. This is expected to results in the lower number of atoms collected in the UHV-MOT, at the lower speed of atom flux

from the VC-MOT, which allows a large transverse expansion of the flux during transit from VC-MOT to UHV-MOT. The difference in the number of atoms in graphs (d) and (e) in Fig. 4.5(B) in the regime of very large spot-size (e.g. spot-size $> 200 \mu\text{m}$) is possibly due to this effect. The role of the capture speed of UHV-MOT seems to be negligible for this difference, as the capture speed in both the cases is much higher than the speed of atoms in the flux from the VC-MOT.

In the regime of very large spot-size of the push beam at the VC-MOT, which is the case of spot-size $> 200 \mu\text{m}$ in the data shown in Fig. 4.5(A), the push beam intensity at the VC-MOT is so low that the speed of atoms ejected from the VC-MOT remains much lower (Fig. 4.6) than the capture speed of UHV-MOT. In this spot-size regime, the number of atoms accumulated in UHV-MOT is mainly governed by the rate of number of atoms reaching the UHV-MOT volume. At a given spot-size, a higher power push beam is expected to result in a higher rate of number of atoms ejected from the VC-MOT. Thus a larger number of atoms in the UHV-MOT is expected with the higher power in the push beam, as was experimentally observed for this regime of the spot-size (refer Fig. 4.5(A)). A higher power push beam is also expected to result in a higher speed of atoms ejected from the VC-MOT and a shorter transit time between two MOTs. This provides a lower loss of atoms during the transit which can lead to a higher number of atoms reaching the UHV-MOT volume.

Further, a higher power push beam could also provide a stronger transverse guiding to the atoms during the transfer which would enable a higher number of atoms reaching the volume of UHV-MOT [126, 127]. This guiding effect would be more observable on the number of atoms in the UHV-MOT in the regime of large push beam spot-size ($> 200 \mu\text{m}$). This is because the loading of UHV-MOT in this regime is governed by the rate of number of atoms reaching the UHV-MOT volume, because speed of atoms in the flux from VC-MOT is much smaller than the capture speed of UHV-MOT. The estimated peak dipole potential [114, 115, 128] due to push beam as a function of distance from the VC-MOT for the push beam spot-size of $\sim 200 \mu\text{m}$ at the VC-MOT is shown in Fig. 4.7. Since ejected atoms from the VC-MOT are pumped to hyperfine state ($5S_{1/2} F = 1$) due

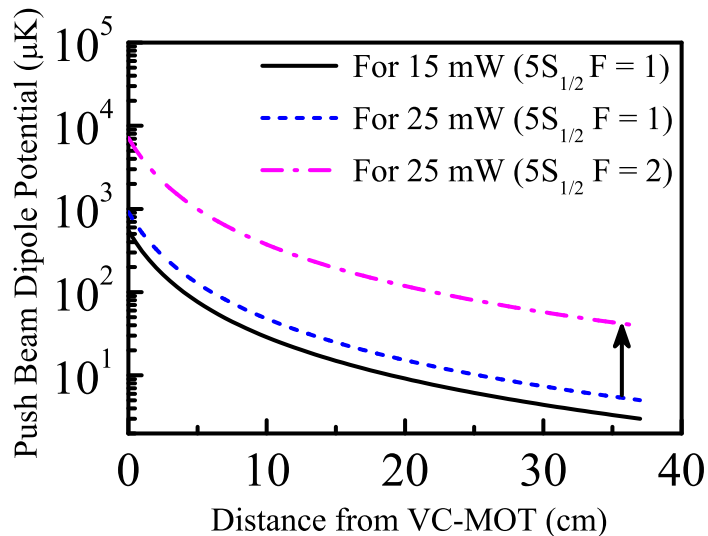


Figure 4.7: The calculated variation in the peak dipole potential of push beam with distance from VC-MOT along propagation direction, for the push beam spot-size of $200 \mu\text{m}$ at the VC-MOT position. Different curves show the potential for ^{87}Rb atoms in different hyperfine states at different push beam powers. The arrow indicates the position of UHV-MOT where atoms are pumped to $(5S_{1/2} F = 2)$ state due to presence of the UHV-MOT re-pumping beam.

to their interaction with the push beam in absence of the re-pumping laser beam. Fig. 4.7 shows the guiding potential of push beam for the two atomic states $(5S_{1/2} F = 1)$ and $(5S_{1/2} F = 2)$. This figure shows that for the atomic state $(5S_{1/2} F = 1)$, the push beam can provide transverse guiding effectively only upto a distance of few centimeters from the VC-MOT. This is because the dipole potential over this distance remains higher than (or comparable to) the transverse temperature ($\sim 300 \mu\text{K}$) of VC-MOT atoms. After this distance, the guiding due to push beam would become ineffective. The push beam guiding potential is expected to become high again to provide the effective transverse guiding when atoms enter the UHV-MOT volume, where (position shown by arrow in Fig. 4.7) they are pumped to the $(5S_{1/2} F = 2)$ hyperfine state due to presence of the UHV-MOT re-pumping laser beam.

For the push beam spot-size values in the intermediate range, which is from $140 \mu\text{m}$ to $200 \mu\text{m}$ in the measurements shown in Fig. 4.5(A), the speed of the atoms from the VC-MOT is comparable to (or lower than) the capture speed of UHV-MOT (refer Fig. 4.6). In this regime of push beam spot-size, both the parameters, the speed of atoms from the

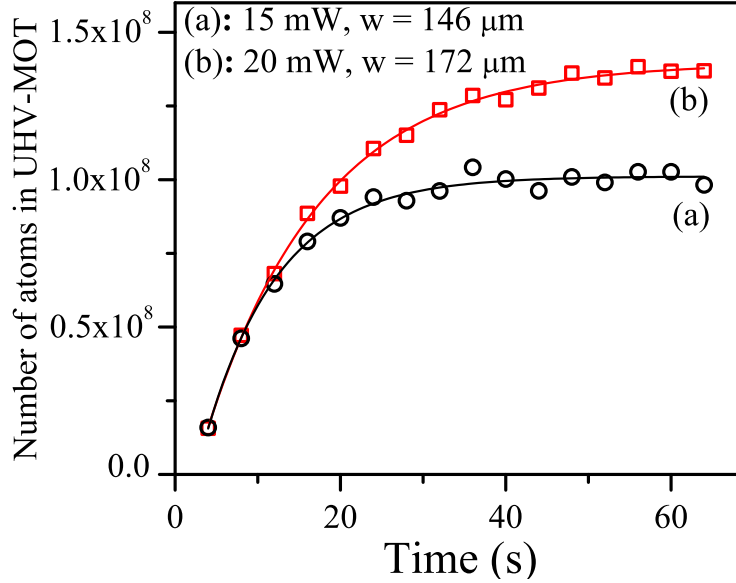


Figure 4.8: Loading graph of UHV-MOT for different values of push beam spot-size at the VC-MOT; (a) spot-size $146 \mu\text{m}$ (power 15 mW) and (b) spot-size $172 \mu\text{m}$ (power 20 mW). The continuous curves are for guiding eye to the measured data.

VC-MOT and the rate of number of atoms reaching the UHV-MOT volume are important which decide the number accumulated in the UHV-MOT. The direct measurement of rate of number of atoms reaching the UHV-MOT volume was difficult in our experiments due to presence of a narrow differential tube and lack of access to the flux from the VC-MOT to UHV-MOT. In order to establish that the rate of number of atoms reaching the UHV-MOT volume is dependent on the push beam spot-size at VC-MOT, we studied the loading of UHV-MOT for different spot-sizes of push beam at the VC-MOT. The intensity of push beam was kept nearly same for different spot-sizes by adjusting the push beam power. The measured loading graphs for the UHV-MOT are shown in Fig. 4.8 for two values of the push beam spot-size at the VC-MOT. In this figure, the graph (a) shows the temporal variation in the number of atoms in UHV-MOT for push beam power of 15 mW and spot-size $\sim 146 \mu\text{m}$, and the graph (b) shows this variation for push beam power of 20 mW and spot-size $\sim 172 \mu\text{m}$. These push beam parameters correspond to the peak number of atoms in UHV-MOT in graphs (a) and (b) in Fig. 4.5(A). Since the push beam intensity was nearly same for two graphs in Fig. 4.8, the observed difference in the loading rate of UHV-MOT shown in two graphs in this Fig. 4.8 is due to difference in the rate of number of atoms reaching the UHV-MOT for different spot-sizes (and powers)

of the push beam at VC-MOT. This established that at a given push beam intensity (i.e. at a given speed of atom flux from VC-MOT), the rate of number of atoms reaching the UHV-MOT volume was higher for larger spot-size of the push beam at the VC-MOT. Therefore, a proper combination of the push beam spot-size and power at the VC-MOT is important to obtain the maximum number of atoms accumulated in the UHV-MOT. As is evident from Fig. 4.5(A), in our experiments, we obtained the best results for the number of atoms in the UHV-MOT with the push beam power of 20 mW and spot-size of $\sim 172 \mu\text{m}$ at the VC-MOT position.

4.4 Summary

To summarize the results, the studies presented in this chapter show that a red-detuned push beam results in higher number of atoms transferred to UHV-MOT from the VC-MOT, as compared to the resonant push beam. This is achieved by exploiting the guiding capabilities of red-detuned beam to atoms under transform. The red-detuned beam is also less destructive to UHV-MOT as compared to the resonant beam. The above properties of red-detuned push beam can be further exploited by using it in retro-reflection geometry to enhance number of atoms in UHV-MOT.

The studies have been extended further to investigate the effect of spot-size of red-detuned push beam at VC-MOT on number of atoms transferred to UHV-MOT. It has been found that at a given power in push beam, number of atoms in UHV-MOT first increases with increasing spot-size and then decreases with it, after attaining a maximum value. The number finally achieved in UHV-MOT is sensitive to spot-size and power of push beam at VC-MOT and capture speed of UHV-MOT. The experimental observations on variation in number of atoms in UHV-MOT with push beam spot-size and power have been explained qualitatively and supported by additional experimental and simulated data.

Chapter 5

Magnetic trapping of laser cooled ^{87}Rb atoms and evaporative cooling in the magnetic trap

5.1 Introduction

The first demonstration of magnetic trapping of neutral atoms [92] proved to be an instrumental idea in achieving the Bose-Einstein condensation (BEC) of alkali atoms in a magnetic trap after evaporative cooling [13, 21–23]. For trapping of cold neutral atoms several designs of magnetic traps have been proposed and demonstrated [13, 43]. To further lower the temperature of atom clouds obtained by laser cooling, evaporative cooling of atoms in the magnetic trap is a very promising method. In this method, the higher energy atoms from the trap are ejected by the application of radio frequency radiation, leading to a decrease in the temperature. Using the evaporative cooling process, the temperature can be lowered to reach the critical temperature to achieve the BEC of atoms (i.e. achieve phase-space density ~ 2.612).

In this chapter, magnetic trapping of laser cooled ^{87}Rb atoms and evaporative cooling studies are described. The loading of a quadrupole magnetic trap is presented. In the quadrupole trap loading section, the results on optimization of state preparation stages

like compressed MOT, optical molasses and optical pumping are discussed. A study on the behaviour of temperature, number density and phase-space density in a quadrupole magnetic trap and their dependence on the initial cloud parameters are presented. In these studies we have shown that, there exists an optimum quadrupole field gradient for a given temperature and size of atom cloud, for which the phase-space density during transfer of atom cloud to a magnetic trap is maximum. The conversion of a quadrupole trap into a quadrupole-Ioffe configuration (QUIC) trap is also described in this chapter. The QUIC trap is suitable to perform evaporative cooling by preventing the Majorana losses in this trap. Finally, the implementation of RF-evaporative cooling in the QUIC trap is described.

5.2 Magnetic trapping of laser cooled atoms

As described in section 1.2, atoms having magnetic dipole moment ($\vec{\mu}$) can be trapped in a potential created by an inhomogeneous magnetic field. The trap depth of the potential generated by the magnetic field determines the kinetic energy of the atoms trappable in the trap. As the potential scales as $\mu_B B$, the trap depth has the order of B times the ratio of μ_B/k_B ($\sim 67\mu\text{K}/\text{G}$). It is important to note here that the wall of the UHV-MOT glass cell in our setup acts as a boundary of the trap, where the field is normally of the order of 200 G (assuming the field gradient in quadrupole trap ~ 155 G/cm in our setup), which results in a trap depth of ~ 13 mK. Therefore, pre-cooling of the atoms is a basic requirement for magnetic trapping. We have initially cooled the atoms in an UHV-MOT and then transferred these UHV-MOT atoms to a magnetic trap. The experimental procedure is described below.

5.3 Preparation of UHV-MOT atom cloud for magnetic trapping

The atom cloud obtained in an UHV-MOT, is not suitable for directly loading to a magnetic trap. Magnetic trapping needs all the atoms to be in the trappable state having appropriate hyperfine quantum number and a suitably lower temperature of the cloud. Therefore, before transferring the atoms from UHV-MOT to a magnetic trap, preparation of the atom cloud in trappable state is necessary.

To lower the temperature and increase the density of atoms in the UHV-MOT cloud, stages like compressed MOT and optical molasses are implemented. Subsequently, the optical pumping is implemented to accumulate most of the atoms in a suitable quantum hyperfine state (i. e. $5 S_{1/2} |F = 2, m_F = 2\rangle$ of ^{87}Rb atom in our case).

Compressed MOT

A smaller size and higher density cloud is beneficial for the magnetic trap loading. The compressed MOT (CMOT) stage [39] is a very widely used technique for this. This stage helps in compressing the cloud to a smaller size suitable for magnetic trapping. Experimentally, we have implemented the CMOT cooling by varying the frequency detuning of the cooling laser beams of UHV-MOT and observing the number of atoms trapped in the quadrupole magnetic trap (at a current 13 A with field gradient $b \sim 95$ G/cm) for a fixed setting of optical pumping parameters. Tentatively, the CMOT duration was set 20 ms which gave us the best results (Fig. 5.5). The variation in number of atoms trapped in magnetic trap with detuning of the cooling laser beams in CMOT stage is shown in Fig. 5.1. In this figure the ordinate axis shows the fluorescence counts which is proportional to the number of atoms in the magnetic trap. In these measurements, we recorded the image of the cloud in magnetic trap after 100 ms of switching-ON the current in the quadrupole trap. After this duration (as we observed experimentally), the untrappable atoms are removed from the magnetic trap and hence the number measured represents the true number of atoms trapped in the magnetic trap. The Fig. 5.1 shows

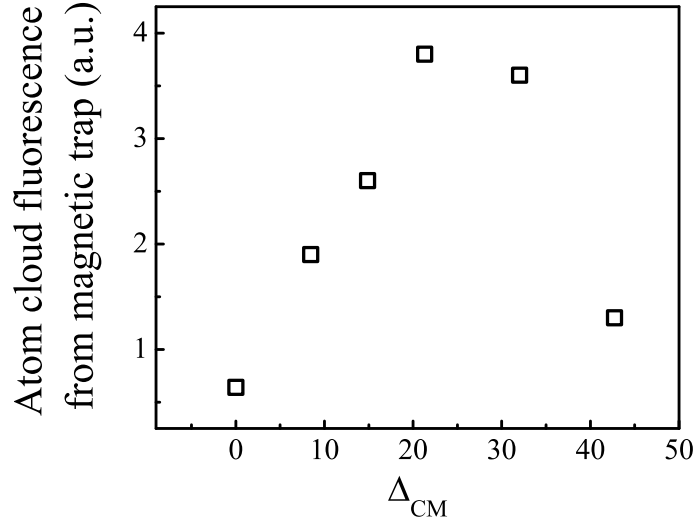


Figure 5.1: Variation in number of atoms collected in a quadrupole magnetic trap (having field gradient $b \sim 95 \text{ G/cm}$) with change in the cooling laser frequency detuning (Δ_{CM}) for compressed MOT.

the optimum value of detuning in CMOT. Typically in our experiments, the temperature of atom cloud obtained after CMOT stage is in the range of $150 - 200 \mu\text{K}$ and number in the range of $\sim 1 - 2 \times 10^8$. This number can be varied to even higher value by appropriately adjusting the current in the Rb getter and with appropriate alignment of the VC-MOT beams, UHV-MOT beams and push beam.

Optical molasses

It is known that during the loading of the atom cloud in the magnetic trap, the atoms gain energy from the trapping field which results in increase in the temperature of the atom cloud in the magnetic trap. Therefore, it is intuitive to lower the temperature of the cloud prior to loading the magnetic trap. This is achieved by cooling the UHV-MOT atoms in the optical molasses in absence of magnetic field [29].

In our setup, atom cloud from the compressed UHV-MOT (CMOT) was kept in optical molasses by switching-OFF the UHV-MOT field gradient and further increasing the detuning of the cooling laser beam. The time duration of optical molasses was in the range of $1 - 10 \text{ ms}$. It was observed that though the temperature was decreasing with molasses duration, but at the cost of decrease in number of atoms. After cooling in

optical molasses, we obtained the temperature in the range of 50-100 μK .

Optical pumping

It is known that only a few magnetic quantum number states ($5S_{1/2} |F = 2, m_F = 2\rangle$, $5S_{1/2} |F = 2, m_F = 1\rangle$ and $5S_{1/2} |F = 1, m_F = -1\rangle$) are trappable in case of ^{87}Rb . Therefore, optical pumping of atoms is performed to transfer the atoms from non-trapping states to a trapping state. In our setup, optical pumping of atoms to ($5S_{1/2} |F = 2, m_F = 2\rangle$)

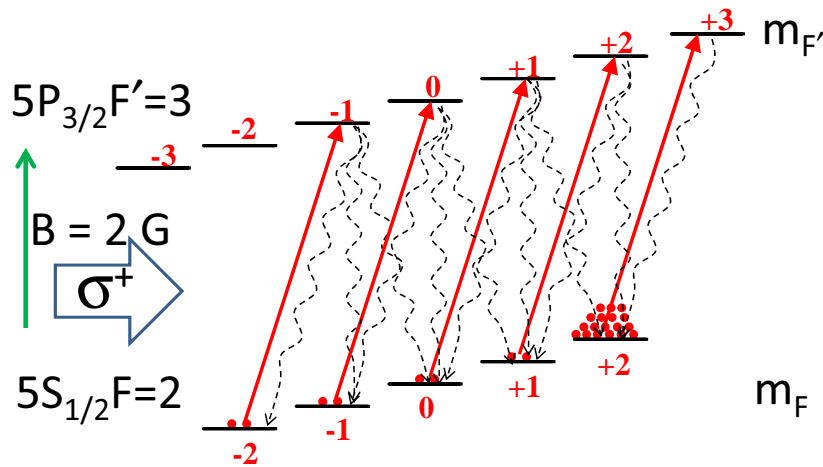


Figure 5.2: Schematic of the optical pumping method. The solid black lines represent the Zeeman states for the ($5S_{1/2} F = 2$) and ($5P_{3/2} F' = 3$) for ^{87}Rb atom in presence of a bias field. A σ^+ light resonant to ($5S_{1/2} F = 2$) \rightarrow ($5P_{3/2} F' = 3$) excite the transitions (shown by solid red arrow), followed by spontaneous emission (shown by dotted wavy arrow) cycle. Finally, the population from different Zeeman states optically pumped to ($5S_{1/2} |F = 2, m_F = 2\rangle$) state.

state was done. The ($5S_{1/2} |F = 2, m_F = 2\rangle$) state was selected, because at a certain field gradient of the trap, this state can provide a stronger confinement to the atoms due to its higher magnetic moment as compared to the other two states. To perform the optical pumping of atoms to ($5S_{1/2} |F = 2, m_F = 2\rangle$) state, the optical pumping beam (2.3.2) of power $\sim 500 \mu\text{W}$ (peak intensity of the beam is $\sim 1.6 \text{ mW}/\text{cm}^2$) was aligned with one of the UHV-MOT beam. A bias field of ~ 2 Gauss was generated by a pair of coils (wrapped on the water-cooling jacket of the quadrupole coil (UMQC)). The direction of UHV-MOT beam was chosen in such a way that the helicity of the beam was σ^+ with respect to the bias field (which provides the quantization axis to the atoms).

As illustrated in the schematic of the optical pumping scheme (Fig. 5.2) after multiple absorption and emission cycles, atoms were pumped to ($5S_{1/2} |F = 2, m_F = 2\rangle$). The re-pumping part of the optical pumping beams helped in transferring the atoms that have decayed to the ($5S_{1/2} F = 1$) state. The optical pumping beam duration and the

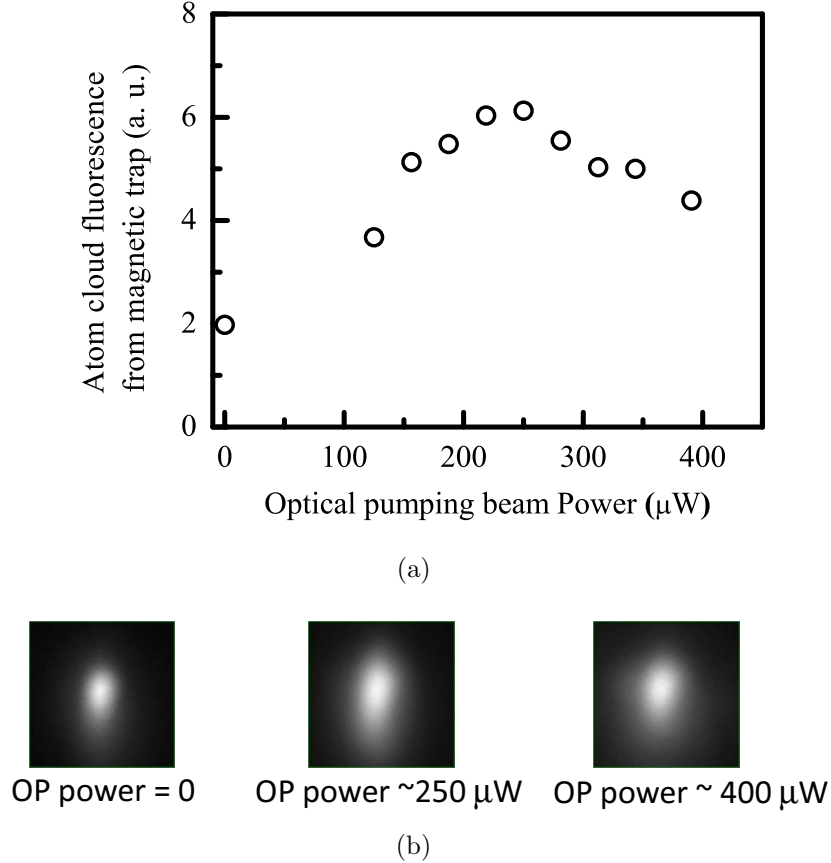


Figure 5.3: (a): The variation in fluorescence from the atom cloud in magnetic trap (proportional to number of atoms) with the power of the optical pumping beam for a duration of $500 \mu\text{s}$ and a bias field of $\sim 2 \text{ G}$.(b): Fluorescence images of cloud of ^{87}Rb atoms trapped in a quadrupole trap for different values of power in optical pumping (OP) beam.

bias field parameters (strength and duration) were varied and corresponding variation in number of atoms in the trap was recorded. These studies have guided us to set the optical pumping beam duration $500 \mu\text{s}$ and a bias field of $\sim 2 \text{ G}$. For these parameters, the variation in fluorescence from the atom cloud in magnetic trap (proportional to number of atoms) with optical pumping beam power is shown in Fig. 5.3(a). Fig. 5.3(b) shows the images of cloud in the quadrupole magnetic trap for different values of optical pumping beam power. In these measurements, the cloud images were recorded after 100

ms of magnetic trap loading. We have kept the bias field duration ($1500 \mu\text{s}$) higher than the optical pumping beam duration ($500 \mu\text{s}$), so that the alignment of the magnetic moment of the atom can be maintained during the switching-on of the quadrupole magnetic trap. Typically, with our optimized optical pumping process, we can transfer 30-40 % of atoms from UHV-MOT to quadrupole magnetic trap. This, however, can be improved with some modifications in optical pumping magnetic field pulse shape used by us.

5.4 Characterization of atom cloud in the quadrupole magnetic trap

The Fig. 5.4 and Fig. 5.5 show the schematic of experimental setup and sequence of various stages of cooling and magnetic trapping experiments performed on ^{87}Rb atoms. As described before in chapter 2, the VC-MOT was formed in a chamber at $\sim 1 \times 10^{-8}$ Torr pressure (with Rb-vapor), and the UHV-MOT was formed in a glass cell at $\sim 6 \times 10^{-11}$ Torr pressure. In these experiments, the UHV-MOT was loaded by transferring atoms from the VC-MOT using a red-detuned (detuning value $\delta/2\pi = -1.0 \text{ GHz}$ with respect to peak of $(5S_{1/2} F = 2) \rightarrow (5P_{3/2} F' = 3)$ transition of ^{87}Rb atom) push laser beam. The duration and sequence of various stages from VC-MOT formation to magnetic trapping and detection shown schematically in Fig. 5.5 was accomplished using a Controller system (described in section 2.11) operated by a PC and LabVIEW program.

A pair of water-cooled quadrupole coils (UMQC in Fig. 5.4) for UHV-MOT as well as for magnetic trapping has been used in the experiments. To switch-ON the current in these quadrupole coils, an IGBT (Insulated Gate Bipolar transistor) based switching circuitry has been used which results in the current rise-time in the coils $\sim 2.5 \text{ ms}$. The current switch-OFF time of this circuitry is much shorter ($\sim 100 \mu\text{s}$) than the rise-time. The switching circuit receives the trigger pulse from the Controller (shown in Fig. 5.5) to switch the current in the coils for UHV-MOT formation as well as for magnetic trapping. For magnetic trapping, a much higher value of current in these quadrupole coils was used in the experiments. The number of atoms in the magnetic trap was estimated using

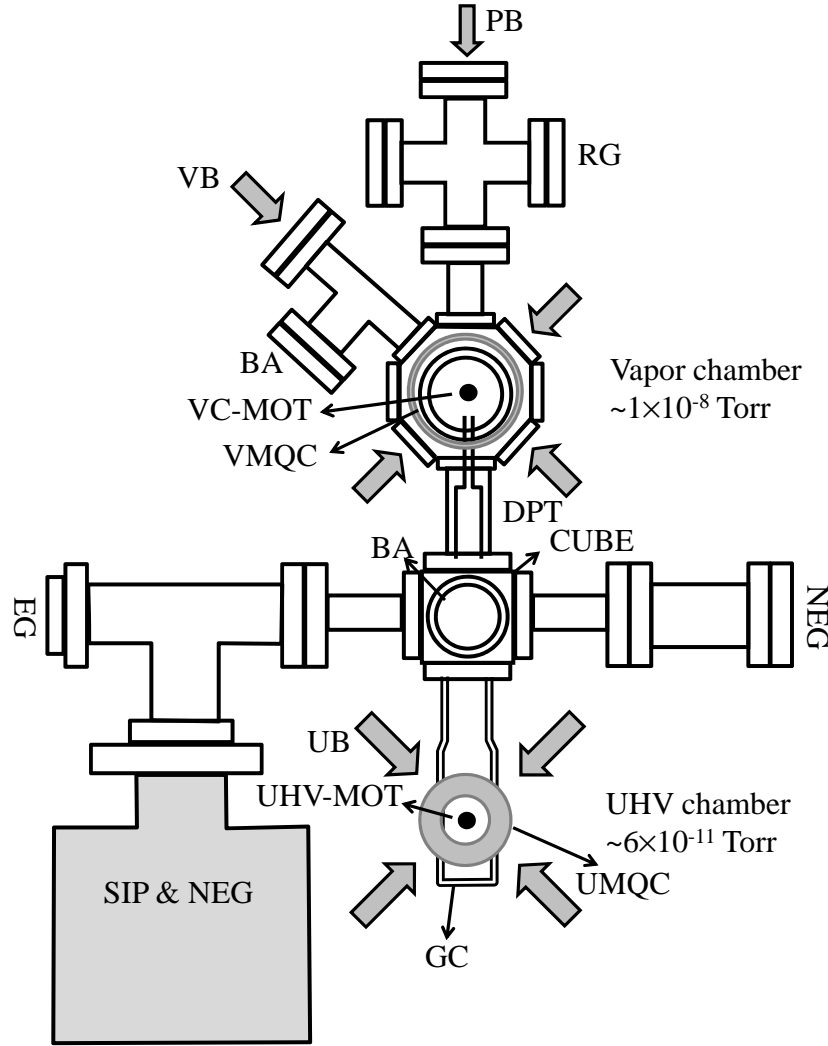


Figure 5.4: The schematic of the experimental setup. VB: VC-MOT beams, UB: UHV-MOT beams, PB: push beam, VMQC: VC-MOT quadrupole coil, UMQC: UHV-MOT quadrupole coil, RG: Rubidium getters, DPT: differential pumping tube, GC: glass cell, BA: Bayerd-Alpert Gauge, EG: extractor gauge, NEG: non-evaporable getter pump, SIP & NEG: combination pump.

the well known fluorescence imaging method which used a resonant probe laser pulse of short ($\sim 100 \mu\text{s}$) duration to shine the trapped atom cloud and collected the emitted fluorescence on a CCD camera [62].

After the preparation of UHV-MOT atoms for magnetic trapping the quadrupole coil (UMQC) current were increased to form the quadrupole trap. In the experimental studies, number of atoms in the atom cloud in the quadrupole magnetic trap and temperature have been estimated only when the atom cloud gets trapped in the quadrupole trap and reaches a nearly steady state equilibrium with the trap. The Fig. 5.6 shows the measured

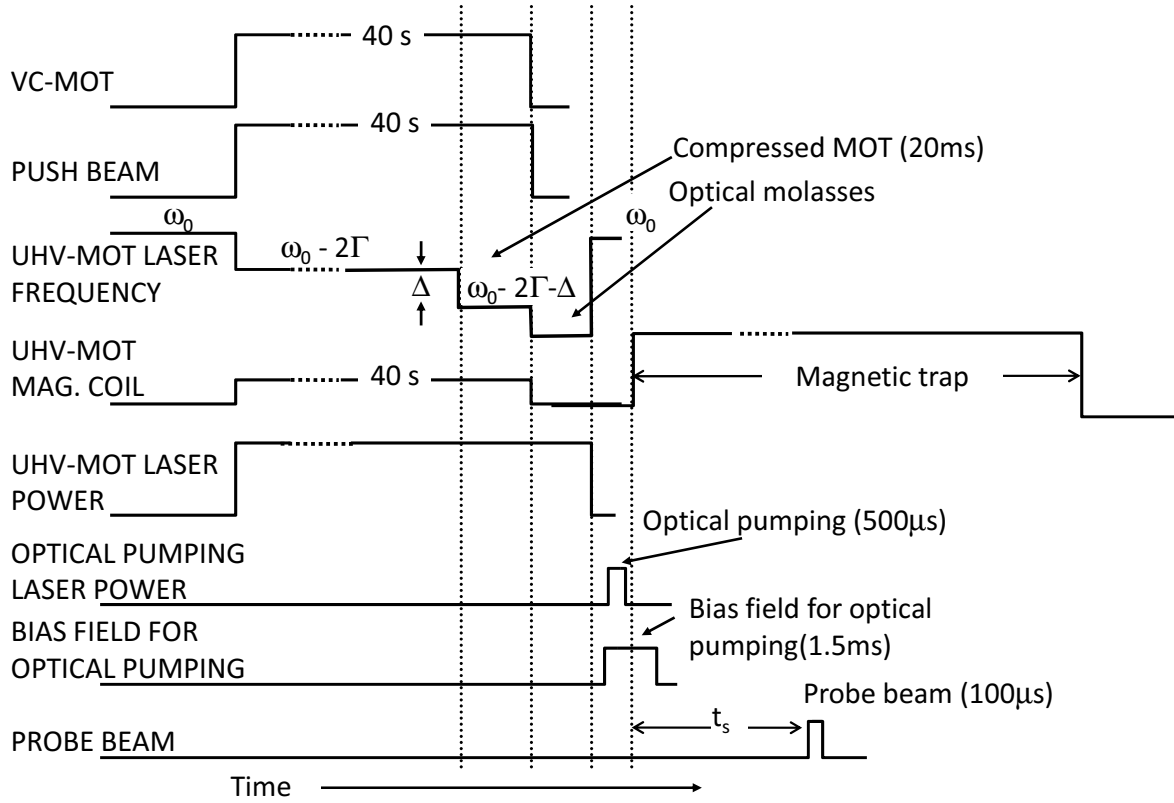


Figure 5.5: The sequence and durations of various stages from VC-MOT formation to magnetic trapping and detection of ^{87}Rb atoms in the experiments.

temporal variation in the fluorescence CCD counts (which is proportional to number of atoms) from the cloud in the magnetic trap. The time shown in the graph is the delay in recording the image of cloud after switching-on current in the quadrupole magnetic trap coils (current $\sim 13\text{ A}$). It is evident from the figure that, after an initial sharp fall in the counts, the CCD counts becomes nearly constant after $\sim 20\text{ ms}$ of time. Thus the number of atoms measured after $\sim 20\text{ ms}$ duration corresponds to the number actually trapped in the magnetic trap. The sharp initial fall in Fig. 5.6 is due to fast removal of un-trappable atoms from the trap. These results thus indicate that, if atoms have spent few hundred ms duration ($> 20\text{ ms}$) in the magnetic trap, the measured number and temperature of the cloud represent the correct values of these parameters in the magnetic trap.

For the temperature measurement of the atom cloud in the magnetic trap a similar fluorescence imaging method was used. In the free expansion method of temperature measurement [89], the imaging was done during the free expansion of the cloud after its

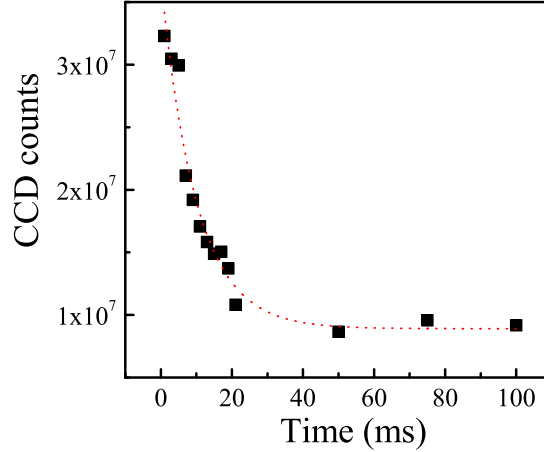


Figure 5.6: The variation in the CCD counts due to fluorescence from atoms trapped in the quadrupole magnetic trap with time for $\sim 13 \text{ A}$ ($b = 95 \text{ G/cm}$) of current in the quadrupole coils. The dotted curve is a guide to the eye.

release from the magnetic trap. The temperature of the atom cloud was estimated from the rate of expansion of the size of the cloud. The temperature in the magnetic trap was also estimated by measuring the size of the cloud in the trap. In the size method the temperature in the magnetic trap can be related to the full width at half maximum (FWHM) size (R_{FWHM}) of the atom cloud in the magnetic trap for a given field gradient b which is given as [104, 130],

$$T_{MT}^S = \frac{2}{5} \frac{\mu_B}{k_B} b R_{FWHM}. \quad (5.1)$$

where, T_{MT}^S denotes the temperature of atom cloud in the magnetic trap measured by the size of the cloud.

5.5 Studies on phase-space density in the quadrupole magnetic trap

In this section, we discuss the studies on changes that occur in temperature, number density and phase-space density (ρ) when a laser cooled atom cloud from the molasses is instantaneously trapped in the quadrupole magnetic trap. The phase-space density (ρ) of atoms in the magnetic trap is of significant importance from the point of view of achieving

BEC (which occurs at $\rho > 2.62$), whereas number density governs the thermalization rate for the evaporative cooling. It is shown here that, the maximum value of ρ in the magnetic trap, after the atom cloud is transferred from molasses to the magnetic trap, depends upon the values of parameters such as temperature and size of the atom cloud in the molasses and the magnetic field gradient of the magnetic trap.

Theory:

We have calculated the temperature, number density and phase-space density of the atom cloud (^{87}Rb atoms) after it is transferred from the molasses to a quadrupole magnetic trap. For this, the atom cloud in the molasses is assumed to have N number of atoms at a temperature T_i and size σ_i (i.e. root mean square (r.m.s.) radius of the number density profile of the cloud). The phase-space density of this initial cloud after molasses is given as [13],

$$\rho_i = n_i \left[\frac{h^2}{2\pi m k_B T_i} \right]^{3/2} \quad (5.2)$$

where n_i is the number density in the molasses, m is the mass of the atom, h is the Planck's constant and k_B is the Boltzmann's constant. The number density of atoms in the atom cloud in the molasses is assumed to be as,

$$n_i(x, y, z) = n_i(0) \exp\left(-\frac{(x^2 + y^2 + z^2)}{2\sigma_i^2}\right), \quad (5.3)$$

which results in relation between the total number of atoms N and and peak number density $n_i(0)$ in the molasses as,

$$N = \int_{-\infty}^{+\infty} \int_{-\infty}^{+\infty} \int_{-\infty}^{+\infty} n_i(x, y, z). dx dy dz = n_i(0)(2\pi\sigma_i^2)^{3/2}. \quad (5.4)$$

It is assumed that during the optical pumping, the rise in the temperature of cloud is negligible. But, when the atom cloud is captured in the quadrupole magnetic trap, both, temperature and number density in the trapped cloud get modified due to interaction of atoms with the field of the trap. This finally leads to the modified temperature, number

density and phase-space density (ρ) of the cloud in the magnetic trap as compared to that in the initial cloud obtained from the molasses. These modified values of the atom cloud parameters in the magnetic trap can be calculated as follows.

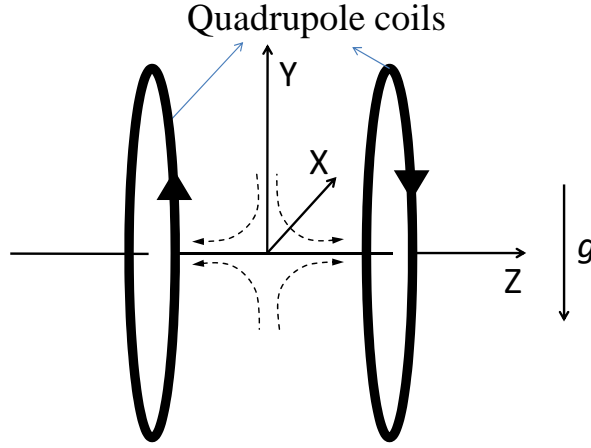


Figure 5.7: Schematic of the arrangement of the coils for quadrupole magnetic trap and axes of the coordinate system.

We consider a quadrupole magnetic trap whose configuration is as shown in Fig. 5.7, where gravitational field direction is along the opposite direction of y-axis. The magnetic field near the center of this magnetic trap can be approximately written as $B = b[-x/2, -y/2, z]$ (as per current direction in Fig. 5.7), where b is the field gradient in axial direction (z - direction). When this magnetic trap is switched-on instantaneously, the atom cloud from molasses (which is assumed to be in the trappable state ($|F, m_F\rangle$)) gains a potential energy from the magnetic trap which is given as [131, 132],

$$\begin{aligned}
 PE &= \langle -\vec{\mu} \cdot \vec{B} \rangle \\
 &= g_F m_F \mu_B b \int_{-\infty}^{+\infty} \int_{-\infty}^{+\infty} \int_{-\infty}^{+\infty} \left(\sqrt{\frac{x^2 + y^2}{4} + z^2} \right) n_i(x, y, z) dx dy dz, \quad (5.5)
 \end{aligned}$$

where m_F is magnetic hyperfine angular momentum quantum number, g_F is Landé g -factor and μ_B is Bohr magneton. On using n_i from equation (5.3) in equation (5.5) and integrating over variables (x, y, z) , we can find the potential energy as

$$PE = 17.34 \frac{N g_F m_F \mu_B b \sigma_i}{(2\pi)^{3/2}}. \quad (5.6)$$

Once cold atom cloud is trapped in the magnetic trap after switching-off molasses and it has reached in equilibrium with the magnetic trap, the total energy of the atoms in the magnetic trap is the sum of the initial kinetic energy and the potential energy gained from the magnetic trap as expressed in equations (5.5) and (5.6). To reach this equilibrium, atoms should have spent sufficient time (τ_M) in the quadrupole trap which scales as $\tau_M \gg 1/\nu_{trap}$, where ν_{trap} is the trap frequency. In such an equilibrium state formed in the trap, the kinetic energy of the atoms is one third of the total energy of the atom cloud in quadrupole trap, as predicted by virial theorem [133]. This gives the temperature (T_f) of the atom cloud in the trap as,

$$\frac{3}{2}Nk_B T_f = \frac{1}{3} \left[\frac{3}{2}Nk_B T_i + PE \right], \quad (5.7)$$

which gives

$$T_f = \frac{T_i}{3} + \kappa \frac{\mu_B b \sigma_i}{k_B}, \quad (5.8)$$

where $\kappa = 0.24$, which is obtained after using $g_F m_F = 1$ for state $|F = 2, m_F = 2\rangle$ of ^{87}Rb atoms. Assuming that all the atoms in molasses are captured in the magnetic trap, the final peak number density $n_f(0)$ in the magnetic trap can be related to the number of atoms in the magnetic trap as,

$$N = n_f(0) \int_{-\infty}^{+\infty} \int_{-\infty}^{+\infty} \int_{-\infty}^{+\infty} \exp \left(- \frac{g_F m_F \mu_B b \left(\sqrt{\frac{x^2+y^2}{4} + z^2} \right) + mgy}{k_B T_f} \right) dx dy dz. \quad (5.9)$$

This gives the final number density at the trap center for state $|F = 2, m_F = 2\rangle$ of ^{87}Rb atoms as,

$$n_f(0) = \frac{N}{32\pi} \left(\frac{\mu_B b}{\frac{k_B T_i}{3} + \kappa \mu_B b \sigma_i} \right)^3 \left[\left(\frac{2mg}{\mu_B b} \right)^2 - 1 \right]^2. \quad (5.10)$$

During the actual experiments, due to finite switching-ON time of current in magnetic trap coils, a fraction of number of atoms in the cloud from the molasses may be lost due

to fall under gravity as well as due to expansion of the cloud. The inefficient optical pumping also contributes to the reduction in number of atoms in the magnetic trap. Thus the number of atoms actually trapped in the magnetic trap (N') is always less than the number of atoms in the molasses (N). Considering all the loss processes and defining 'ε' as overall efficiency for the transfer of atoms from molasses to the magnetic trap, one can relate N' and N as $N' = \varepsilon N$. The peak number density in the magnetic trap can, then, be re-written as,

$$n'_f(0) = \frac{N'}{32\pi} \left(\frac{\mu_B b}{\frac{k_B T_i}{3} + \kappa \mu_B b \sigma_i} \right)^3 \left[\left(\frac{2mg}{\mu_B b} \right)^2 - 1 \right]^2. \quad (5.11)$$

It is important to note here that the above expression is meaningful for $b > 31 \text{ G/cm}$ which is the field gradient required to hold the atoms in the trap against gravity. Using the final peak density given by equation (5.11) and the final temperature T_f in the magnetic trap given by equation (5.8), we can find the final peak phase-space density as,

$$\rho_f(0) = n'_f(0) \left[\frac{h^2}{2\pi m k_B T_f} \right]^{3/2} = \frac{N' (\mu_B b h)^3}{64 \sqrt{2} \pi^{5/2} m^{3/2}} \frac{\left[\left(\frac{2mg}{\mu_B b} \right)^2 - 1 \right]^2}{\left(\frac{k_B T_i}{3} + \kappa \mu_B b \sigma_i \right)^{9/2}}. \quad (5.12)$$

The aim of these calculations is to find the value of $\rho_f(0)$ in the quadrupole magnetic trap and the value of field gradient b which results in maximum value of $\rho_f(0)$ when the quadrupole magnetic field is switched-on to trap the atom cloud of initial temperature T_i and size σ_i . Fig. 5.8 shows the calculated variation in temperature T_f (given by equation (5.8)), the final peak number density $n'_f(0)$ (given by equation (5.11)) and the final peak phase-space density $\rho_f(0)$ (given by equation (5.12)) in the magnetic trap with quadrupole field gradient b , for different values of temperature T_i and size σ_i of the atom cloud in the molasses.

With increase in the b , $\rho_f(0)$ first increases and then decreases after attaining a maximum value at a certain field gradient b . The reduction in $\rho_f(0)$ after the maximum value is due to increase in the temperature of cloud in the magnetic trap and saturation in number density with b . The temperature (T_f) increases with b due to increase in poten-

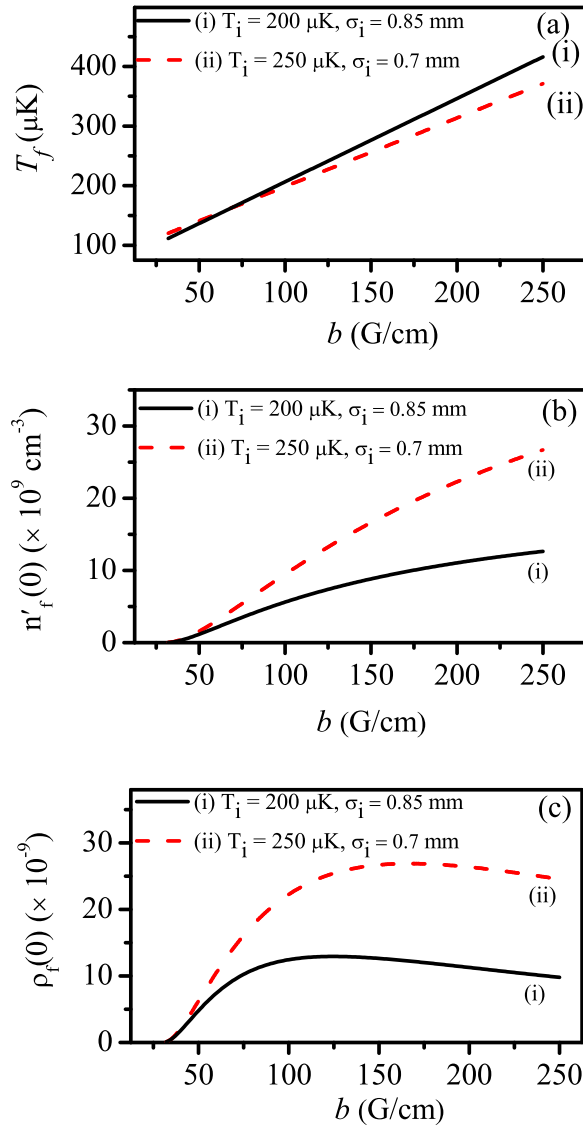


Figure 5.8: The calculated variation in final temperature T_f (figure (a)), final peak density $n'_f(0)$ (figure (b)) and final phase-space density $\rho_f(0)$ (figure (c)) in the quadrupole magnetic trap with field gradient b for the different temperatures and sizes of cloud in molasses. For graphs (i) and (ii) (in figures (b) and (c)), $N' = 2.0 \times 10^7$ and 2.9×10^7 has been used respectively, which are close to the experimentally observed values.

tial energy gained by the cloud from the trap. For lower values of b , the number density in the magnetic trap is low which results in lower values of $\rho_f(0)$. Therefore a maximum for $\rho_f(0)$ is obtained in its variation with the field gradient b .

Experimental results and discussion:

In these experiments, we have first trapped and kept atom cloud in the quadrupole trap for $\sim 500 \text{ ms}$ before recording the cloud images for measurements of number and

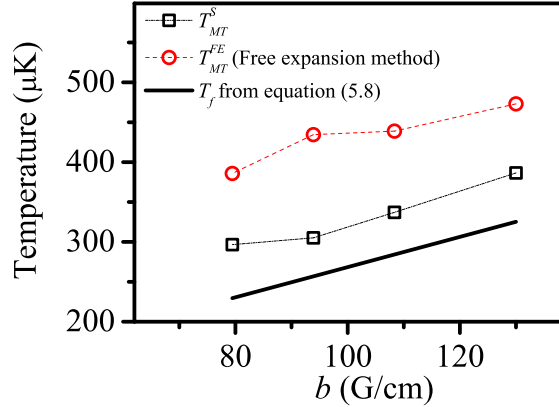


Figure 5.9: Measured variation in the temperature of atoms in the magnetic trap with the field gradient b . Squares show the temperature measured from the size of the cloud in magnetic trap, and circles show the temperature measured by free expansion method. The cloud temperature and size in the molasses were $T_i = 235 \mu\text{K}$ and $\sigma_i = 0.8 \text{ mm}$ respectively.

temperature. The temperature measured by the size (T_{MT}^S) method is shown by squares and temperature measured by free expansion method (T_{MT}^{FE}) is shown by circles in Fig. 5.9 for different values of b . Both these temperature measurement methods were tested on a cloud having the same initial temperature and size values in molasses ($T_i = 235 \mu\text{K}$ and $\sigma_i = 0.8 \text{ mm}$). The data in the figure shows that temperature obtained from the two methods have similar trend in variation with with field gradient b , but the values obtained by free expansion method are slightly higher than those obtained by the cloud size method. But measured temperature was always higher than the theoretically predicted temperature (equation (5.8)) shown by a straight line in the Fig. 5.9.

The Fig. 5.10 shows the measured variation in the number density and phase-space density of the atom cloud in the magnetic trap with the quadrupole field gradient b , for different values of initial temperature (T_i) and size (σ_i) of the cloud in the molasses. Here peak number density has been estimated by measuring the number of atoms and size of atom cloud in the magnetic trap. These data were obtained from the fluorescence image of the trapped cloud. The temperature was obtained from the size of the cloud to know the peak phase-space density of the trapped cloud shown in Fig. 5.10. It was evident from these results that measured values of ρ in the magnetic trap also first increased with b and then decreased with it, after attaining a maximum value at an optimum b .

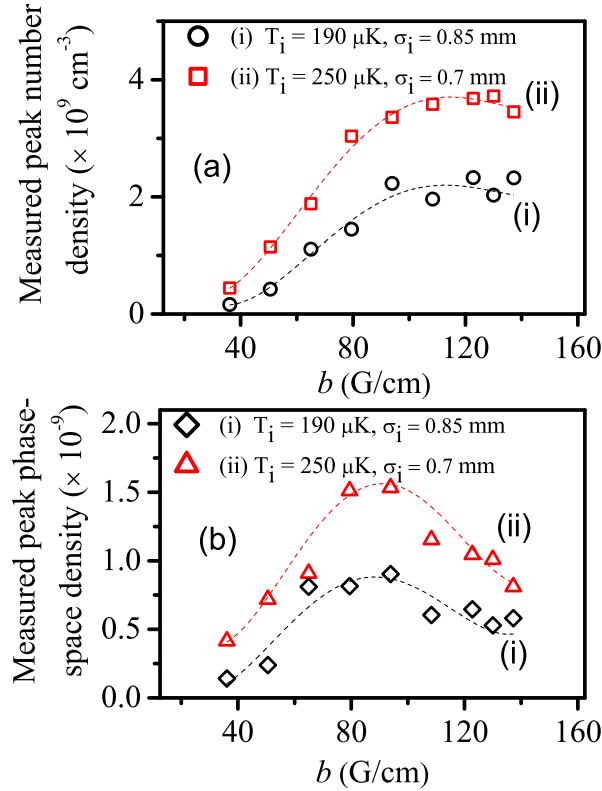


Figure 5.10: Measured variation in peak number density and phase-space density in the magnetic trap with the quadrupole field gradient b , for two sets of temperature and r.m.s size of the cloud in the molasses. The maximum number of atoms in the magnetic trap is $N' = 2.9 \times 10^7$ and 2.0×10^7 for curve (i) and (ii), but N' has varied with the field gradient b . The dashed curves are guide to the eye.

Thus measured number density and phase-space density have shown the similar trend in variation with b as predicted by theory (Fig. 5.8). However, as one can note from the data in Fig. 5.8 and Fig. 5.10, the measured values of number density and phase-space density in the magnetic trap were significantly lower than their theoretically predicted values. We attribute this difference between measured and theoretical values of both the parameters (n and ρ) to the higher value of the measured temperature than the theoretically predicted temperature. Nevertheless, experimentally it has been verified that there exists an optimum field gradient at which the phase-space density in the magnetic trap is maximum.

In the theory, equations (5.11) and (5.12), we had assumed that number actually trapped in the magnetic trap N' was independent of field gradient b . But actually N' changed with b , since ε depends upon the gradient b and switching time of the magnetic trap to reach the set b value. This has been observed experimentally during the measure-

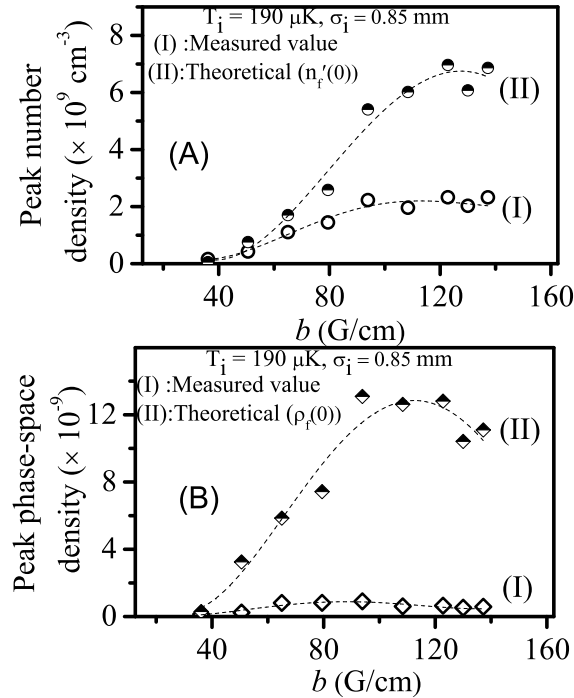


Figure 5.11: A comparison of experimentally measured values and theoretically estimated values of number density (A) and phase-space density (B). In graph (I) (in (A) and (B)) the data for $T_i = 190 \mu\text{K}$ and $\sigma_i = 0.85 \text{ mm}$ from Fig. 5.10 are replotted here. In graph (II) (in (A) and (B)) the measured values of N' (which are dependent on b) have been used in equation (5.11) and (5.12) to estimate the theoretical values. The dashed curves are guide to the eye.

ments. Taking this gradient dependent values of N' , we replotted the theoretical values of $n'_f(0)$ and $\rho_f(0)$ as shown by graphs (II) in Fig. 5.11. For comparison, the experimental values shown in Fig. 5.10 are also replotted in the Fig. 5.11. In this figure also theoretical values are much higher than the experimentally measured values. This shows that variation of N' with b is not the prime reason for difference between theoretical and experimental values of number density and phase-space density parameters. Thus we believe that this observed pronounced difference between theoretical and experimental values of number density and phase-space density is due to the difference in the theoretical and experimentally measured temperature of atom cloud in the magnetic trap (Fig. 5.9). This is because, both, number density and phase-space density, are highly non-linear functions of the temperature.

The difference in the theoretical and experimentally measured temperature was also reported by Stuhler et al. [133]. This difference between experimentally measured and

theoretically expected values of temperature could be due to several reasons. One of these could be the mismatch between centers of magnetic trap and molasses and other could be the heating of the atom cloud during the optical pumping. Both these have not been considered in the theory.

These results described in this section have been communicated to a journal for publication.

5.6 Formation of QUIC trap

After the initial switching-on of the quadrupole trap fields, the current in the quadrupole coils (UMQC) was slowly ramped to 23 A in 500 ms to form the quadrupole trap fully. After quadrupole coils current reaches the maximum value, current in Ioffe coil was slowly ramped from 0 to 19.5 A to convert quadrupole trap configuration into the QUIC trap configuration. The Fig. 5.13(a) shows the oscilloscope traces of the current varied in the quadrupole and Ioffe coils during the formation of QUIC trap. The minimum of resultant field (also of the potential energy) in our QUIC trap appears at a position $x \sim -8.5$ mm which was shifted towards the Ioffe coil as compared to position of the minimum in the

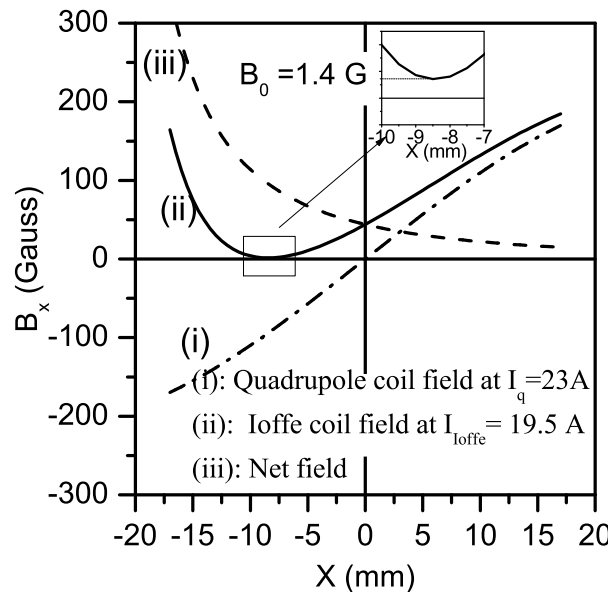
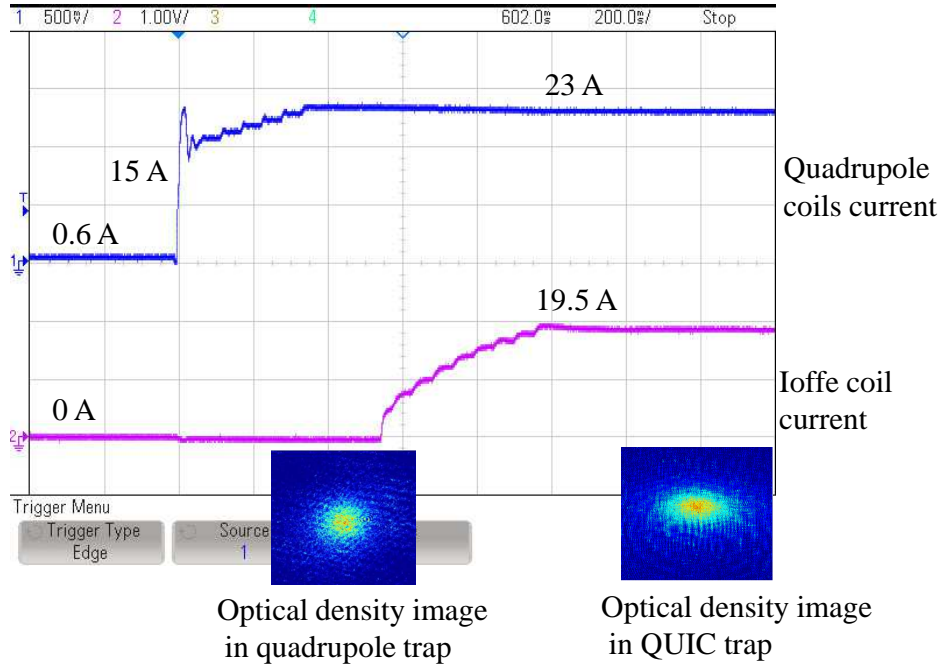
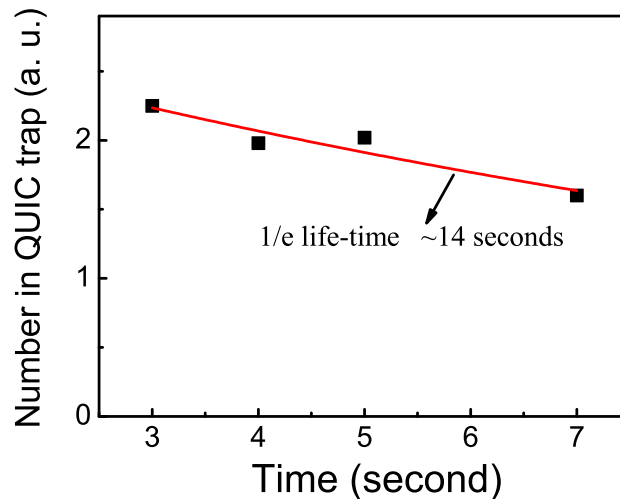


Figure 5.12: Magnetic field distribution along Ioffe coil axis. The Inset shows the non-zero offset of the QUIC trap.



(a)



(b)

Figure 5.13: (a): The oscilloscope traces showing variation in current in the quadrupole coils and Ioffe coil with time. Absorption images of cloud (i.e. the optical density) trapped in the quadrupole trap and the QUIC trap are also shown. (b): Measured life-time of atoms in the QUIC trap obtained from variation in number of atoms in it with time.

quadrupole occurring at $x = 0$ (Fig. 5.12). The same shift in the position of atom cloud took place during the conversion of quadrupole trap into QUIC trap. Since we used absorption probe imaging technique to characterize the atom cloud in the QUIC trap and in evaporative cooling this lateral shift in the position of atom cloud in the QUIC trap forced us to laterally translate the absorption probe beam and adjust the CCD

camera and imaging optics to keep the atom cloud in the field of view of imaging system. The (Fig. 5.13(a)) shows the modification in the shape of cloud images (optical density obtained from absorption probe method) when the quadrupole trap was converted to QUIC trap. The elongated cloud shape in QUIC trap is due to the slow variation in the trapping potential (low value of trap frequency) along the Ioffe axis.

The current values discussed above were obtained from the simulations and experimentally measured data generated for formation of QUIC trap configuration. The ramping durations were set to maximize the life-time of the atoms in the QUIC trap. During the magnetic trapping of atoms, it was important that all kinds of background light going to magnetic trap area should be stopped. Thus magnetic trapping should be performed in a completely dark environment. The solenoid actuator based mechanical shutters were used at different places in the path of the laser beams which were kept closed during the magnetic trapping to stop the light leaked from various AOMs used as switch for the MOT laser beams. With nearly complete darkness in the magnetic trap region and appropriate UHV maintained in the glass cell, we get a life-time (> 10 seconds) of atoms in the QUIC trap (Fig. 5.13(b)), which is necessary for evaporative cooling experiments.

5.7 Evaporative cooling in the magnetic trap

For evaporative cooling of ^{87}Rb atoms trapped in our QUIC trap, we apply radio frequency (RF) radiation emitted from a single loop antenna kept at one side of the glass cell with loop axis along the axis of quadrupole trap axis (z-axis). To scan the frequency of RF radiation, we used a logarithmic variation in frequency with time to achieve efficient evaporative cooling. We have run a number of RF-evaporation cycles with different ranges of frequency scan and with different powers of RF source.

After each run of RF-evaporation, the atom cloud was imaged by absorption probe imaging method and optical density image of the cloud was generated after processing of the absorption image of the cloud. Fig. 5.14 shows the optical density image and the corresponding profile of the atom cloud cooled by different RF frequency scans. The

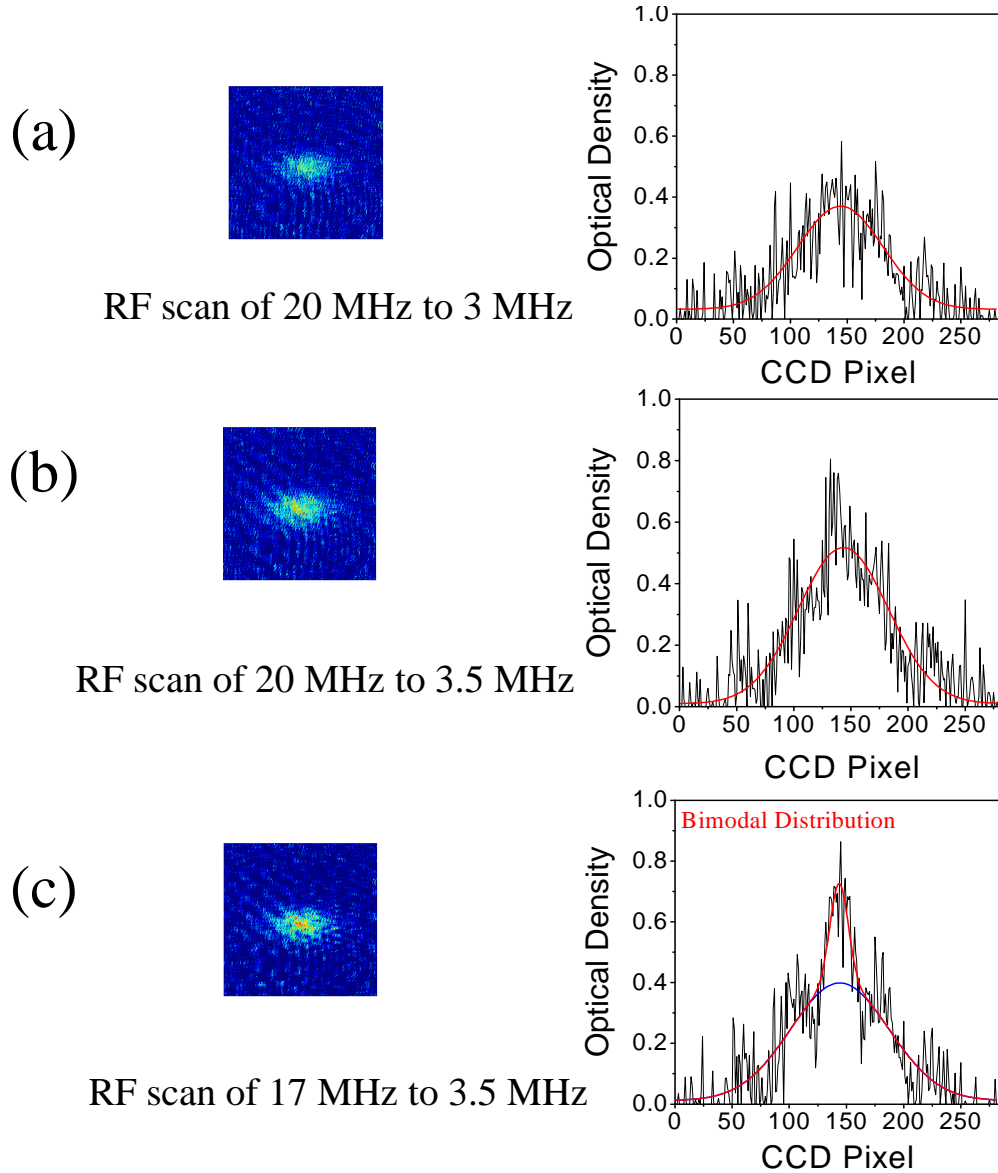


Figure 5.14: Optical density images obtained from absorption probe images and its profile along the central line of atom cloud after RF evaporation in the QUIC trap. The bimodal distribution observed in the profile (c) is an indication of onset of Bose-Einstein condensation of atoms in the cloud.

estimated temperature and number of atoms in the cloud in Fig. 5.14(c) was $\sim 1\mu\text{K}$ and $\sim 10^6$. The (Fig. 5.14(c)) shows the optical density image and its profile for RF scan from 17 MHz to 3.5 MHz (at RF power in this frequency range 6-8 W). Fig. 5.15 shows the 3D plot of optical density of image shown in Fig. 5.14(c). In these figures, a bimodal distribution with a sharp peak at the center against the broad Gaussian distribution at the skirts is an indication of onset of BEC in the cloud. In future, our endeavor will be to improve the signal to noise ratio in the data to obtain a nearly pure Bose condensate.

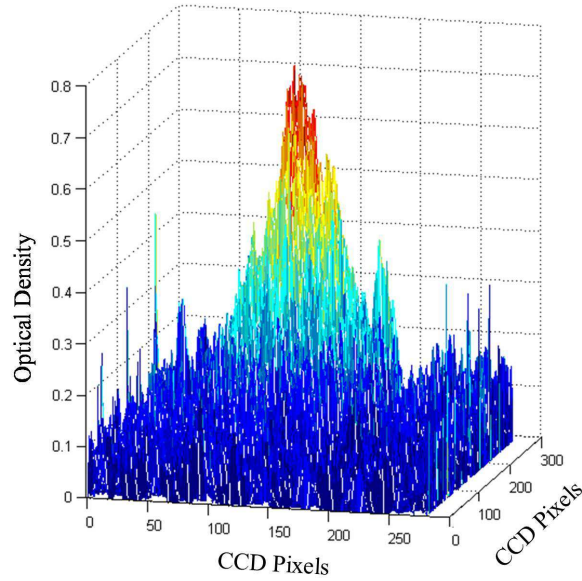


Figure 5.15: A 3D plot of optical density of the absorption image shown in Fig. 5.14(c) after three-point averaging. Sharp peak in the center depicts the bimodal distribution in the cloud.

5.8 Summary

To summarize, in this chapter we have discussed about magnetic trapping of laser cooled ^{87}Rb atoms and evaporative cooling in the magnetic trap. Different stages required for magnetic trapping have been discussed. It was shown theoretically and experimentally that, for a given temperature and size of cloud in optical molasses, there exists an optimum quadrupole field gradient for which the phase-space density of atoms is maximum in magnetic trap. The loading and formation of the QUIC trap has been discussed. Further lowering of the temperature of the atom cloud in the QUIC trap by employing RF-induced evaporation has been discussed.

Chapter 6

Conclusions

The generation of samples of ultracold atoms is of prime importance in the field of atomic physics for basic research experiments as well as for developing state-of-art devices for precision measurements and other applications [3–6, 8, 56]. During this thesis work, generation and manipulation of samples of cold ^{87}Rb atoms in the temperature range of few hundred micro-Kelvin to few micro-Kelvin has been studied. A double-MOT experimental setup for ^{87}Rb atoms has been developed in-house which served as the main apparatus for these studies. In this double-MOT setup, the cooling of ^{87}Rb atoms begins with the loading of VC-MOT. The laser cooled atoms in VC-MOT are then transferred to the UHV-MOT using a push laser beam. The efficiency of transfer of atoms from VC-MOT governs the number of atoms accumulated in the UHV-MOT which is important for further use of cold atoms in the UHV-MOT for magnetic trapping and evaporative cooling. In this thesis work, various techniques for the atoms transfer have been investigated to increase the number of atoms accumulated in the UHV-MOT. Among these, the use of a resonant push beam is the first which is investigated in detail. It has been demonstrated that use of a continuous wave (CW) resonant push beam in presence of a hollow beam results in a higher number of atoms accumulated in the UHV-MOT than the number obtained without hollow beam [62]. It has been further observed that a pulsed and unfocused push beam results in higher number of atoms in the UHV-MOT than the number obtained with a CW push beam. The durations of push beam and the VC-MOT

loading are important parameters to maximize the number of atoms accumulated in the UHV-MOT [63].

Further investigations on atom transfer from VC-MOT to UHV-MOT have revealed that use of a red-detuned continuous wave (CW) push beam focused on the VC-MOT results in much higher number of atoms in the UHV-MOT than that obtained using a resonant push beam. This is due to pushing-cum-guiding capacity of red-detuned push which facilitates a higher number of atoms reaching the capture volume of UHV-MOT. It has also been demonstrated during this thesis work that use of the red-detuned push beam in retro-reflection geometry can further improve the number of atoms accumulated in the UHV-MOT [64]. In the subsequent studies on atom transfer with red-detuned push beam, it has been found that spot-size of push beam on VC-MOT plays an important role in the transfer of atoms between two MOTs. There is an optimum value of push beam spot-size at which number of atoms accumulated in the UHV-MOT is maximum, for a given power in the push beam [74]. This optimum value of push beam spot-size depends upon power in push beam as well as on the capture speed of UHV-MOT. The processes responsible to lead these results and observations have been investigated during the course of this thesis work and are presented in the thesis. The results obtained during this work are useful in the understanding the atom transfer process in general, and, in maximizing the number of atoms in the UHV-MOT in particular.

The magnetic trapping and evaporative cooling is another dimension of the work presented in this thesis. In the studies presented in the thesis, it has been shown that the temperature, number density and phase-space density of atom cloud in the quadrupole magnetic trap depend upon the value of magnetic field gradient switched on instantaneously for trapping the laser cooled atom cloud in the quadrupole trap. The phase-space density in the magnetic trap attains a maximum value at an optimum value of magnetic field gradient in the magnetic trap [134]. These results can be used to set a higher value of initial phase-space density of the atom cloud to begin evaporative cooling of the cloud. The higher phase-space density in the magnetic trap is desirable, when aim of evaporative cooling is to achieve BEC.

In the experiments, the laser cooled ^{87}Rb atoms in the UHV-MOT were first trapped in the quadrupole trap which was then converted into a QUIC trap for evaporative cooling of the trapped atom cloud. In the RF evaporative cooling experiments, the different power and different values of initial and final frequency of RF field were chosen during the scan of RF frequency. This resulted in different values of temperature of atom cloud after evaporative cooling for different ranges of RF scan. For a particular range of RF scan (17 to 3.5 MHz and 6-8 W power), a bimodal distribution in the optical density profile of the cold atom cloud was observed which is indicative of onset of BEC in the cloud. These results have shown that using our setup, a cold atom cloud of ^{87}Rb atoms can be generated with temperature variable in the range of few hundred micro-Kelvin to few micro-Kelvin.

In future, our aim is to use these ultra-cold atoms /Bose condensate samples to study the transport, guiding and splitting of atom cloud using dipole potentials of far detuned laser beams. This is with aim to demonstrate the improvised atom-optic devices. It would also be interesting to perform experiments to investigate in detail the nucleation (i.e. initiation) of BEC in the QUIC trap and its dependence on RF scan and the trap parameters.

Bibliography

- [1] C. Cohen-Tannoudji and D. Guéry-Odelin, *Advances in atomic physics: an overview* (World Scientific Publishing Co. Pte. Ltd., Singapore, 2011). [1](#), [3](#), [16](#)
- [2] V. S. Letokhov, *Laser control of atoms and molecules* (Oxford University Press Inc. New York, 2007). [1](#), [3](#)
- [3] C. J. Bordé, “Atomic interferometry and laser spectroscopy,” in “Laser Spectroscopy X: Proceedings of the 10th International Conference,” , M. Ducloy, E. Giacobino, and G. Camy, eds. (World Scientific Publishing Co Pte Ltd, Font-Romeu, France,, 1991). [1](#), [17](#), [109](#)
- [4] C. J. Bordé, “Matter wave interferometers: a synthetic approach,” in “Atom Interferometry,” , P. R. Berman, ed. (Academic Press Inc., CA, 1997), pp. 257–292.
- [5] A. Peters, K. Y. Chung, and S. Chu, “High-precision gravity measurements using atom interferometry,” *Metrologia* **38**, 25–61 (2001).
- [6] H. Perrin, P. Lemonde, F. P. dos Santos, V. Josse, B. L. Tolra, F. Chevy, and D. Comparat, “Application of lasers to ultra-cold atoms and molecules,” *Comptes Rendus Physique* **12**, 417 – 432 (2011). [1](#), [17](#), [109](#)
- [7] J. Weiner, V. S. Bagnato, S. Zilio, and P. S. Julienne, “Experiments and theory in cold and ultracold collisions,” *Rev. Mod. Phys.* **71**, 1–85 (1999). [1](#)
- [8] J. J. García-Ripoll, P. Zoller, and J. I. Cirac, “Quantum information processing with cold atoms and trapped ions,” *Journal of Physics B: Atomic, Molecular and Optical Physics* **38**, S567 (2005). [1](#), [17](#), [109](#)
- [9] G. Gilbert, A. Aspect, and C. Fabre, *Introduction to Quantum Optics* (Cambridge University Press, 2010). [1](#)
- [10] R. Krems, B. Friedrich, and W. C. Stwalley, eds., *Cold Molecules: Theory, Experiment, Applications* (CRC Press, Taylor and Francis Group, 2009). [1](#)
- [11] P. Meystre, *Atom Optics* (Springer, 2001). [1](#)
- [12] S. L. Rolston, “Ultracold neutral plasmas,” *Physics* **1**, 2 (2008). [1](#)
- [13] “Bose Einstein condensation in dilute gases,” in “Proceedings of the International School of Physics, Enrico Fermi Course CXL,” , M. Inguscio, S. Stringari, and C. E. Wieman, eds. (IOS Press, Amsterdam, 1999). [1](#), [17](#), [85](#), [95](#)
- [14] C. J. Pethick and H. Smith, *Bose-Einstein condensation in dilute gases* (Cambridge University Press, 2008), 2nd ed. [1](#), [16](#)

- [15] W. D. Phillips and H. Metcalf, “Laser deceleration of an atomic beam,” *Phys. Rev. Lett.* **48**, 596–599 (1982). [1](#)
- [16] S. Chu, L. Hollberg, J. E. Bjorkholm, A. Cable, and A. Ashkin, “Three-dimensional viscous confinement and cooling of atoms by resonance radiation pressure,” *Phys. Rev. Lett.* **55**, 48 (1985). [1](#), [7](#), [10](#)
- [17] E. L. Raab, M. Prentiss, A. Cable, S. Chu, and D. E. Pritchard, “Trapping of neutral sodium atoms with radiation pressure,” *Phys. Rev. Lett.* **59**, 2631 (1987). [1](#), [7](#)
- [18] S. Bose, “Plancks Gesetz und Lichtquantenhypothese,” *Z. Phys.* **26**, 178 (1924). [1](#)
- [19] A. Einstein, “Quantentheorie des einatomigen idealen Gases. Zweite Abhandlung,” *Sitzungber. Preuss. Akad. Wiss.* **1925**, 3 (1925). [1](#)
- [20] R. K. Pathria, *Statistical Mechanics* (Butterworth-Heinemann, Oxford, 1996), 2nd ed. [2](#)
- [21] M. H. Anderson, J. R. Ensher, M. R. Matthews, C. E. Wieman, and E. A. Cornell, “Observation of Bose-Einstein condensation in a dilute atomic vapor,” *Science* **269**, 198–201 (1995). [2](#), [13](#), [14](#), [85](#)
- [22] C. C. Bradley, C. A. Sackett, J. J. Tollett, and R. G. Hulet, “Evidence of Bose-Einstein condensation in an atomic gas with attractive interactions,” *Phys. Rev. Lett.* **75**, 1687 (1995). *ibid.* **79**, 1170 (1997).
- [23] K. B. Davis, M.-O. Mewes, M. R. Andrews, N. J. van Druten, D. S. Durfee, D. M. Kurn, and W. Ketterle, “Bose-Einstein condensation in a gas of sodium atoms,” *Phys. Rev. Lett.* **75**, 3969–3973 (1995). [2](#), [13](#), [85](#)
- [24] C. Adams and E. Riis, “Laser cooling and trapping of neutral atoms,” *Prog. Quant. Electr.* **21**, 1 – 79 (1997). [3](#)
- [25] C. Cohen-Tannoudji, J. Dupont-Roc, and G. Grynberg, *Atom-Photon Interactions: Basic Processes and Applications*, (Wiley-VCH, 1998).
- [26] H. J. Metcalf and P. van der Straten, *Laser Cooling and Trapping* (Springer-Verlag New York Inc., 1999).
- [27] C. J. Foot, *Atomic Physics* (Oxford University Press Inc. New York, 2005). [3](#), [29](#)
- [28] T. W. Hänsch and A. L. Schawlow, “Cooling of gases by laser radiation,” *Opt. Commun.* **13**, 68 (1975). [6](#)
- [29] P. D. Lett, W. D. Phillips, S. L. Rolston, C. E. Tanner, R. N. Watts, and C. I. Westbrook, “Optical molasses,” *J. Opt. Soc. Am. B* **6**, 2084–2107 (1989). [6](#), [38](#), [88](#)
- [30] C. Monroe, W. Swann, H. Robinson, and C. Wieman, “Very cold trapped atoms in a vapor cell,” *Phys. Rev. Lett.* **65**, 1571–1574 (1990). [7](#)
- [31] C. E. Wieman, S. Chu, and Eds., “(Special issue on laser cooling and trapping of atoms: ”Optical Molasses” section),” *J. Opt. Soc. Am. B* **6** (1989). [9](#)

-
- [32] D. Sesko, T. Walker, C. Monroe, A. Gallagher, and C. Wieman, “Collisional losses from a light-force atom trap,” *Phys. Rev. Lett.* **63**, 961 (1989).
- [33] T. Walker, D. Sesko, and C. Wieman, “Collective behavior of optically trapped neutral atoms,” *Phys. Rev. Lett.* **64**, 408–411 (1990).
- [34] D. W. Sesko, T. G. Walker, and C. E. Wieman, “Behavior of neutral atoms in a spontaneous force trap,” *J. Opt. Soc. Am. B* **8**, 946–958 (1991). [9](#)
- [35] W. Petrich, M. H. Anderson, J. R. Ensher, and E. A. Cornell, “Behavior of atoms in a compressed magneto-optical trap,” *J. Opt. Soc. Am. B* **11**, 1332 (1994). [9](#)
- [36] P. D. Lett, R. N. Watts, C. I. Westbrook, W. D. Phillips, P. L. Gould, and H. J. Metcalf, “Observation of atoms laser cooled below the Doppler limit,” *Phys. Rev. Lett.* **61**, 169 (1988). [10](#)
- [37] J. Dalibard and C. Cohen-Tannoudji, “Laser cooling below the Doppler limit by polarization gradients: simple theoretical-models,” *J. Opt. Soc. Am. B* **6**, 2023 (1989). [10](#)
- [38] P. J. Ungar, D. S. Weiss, E. Riis, and S. Chu, “Optical molasses and multilevel atoms: theory,” *J. Opt. Soc. Am. B* **6**, 2058–2071 (1989). [10](#)
- [39] W. Petrich, M. H. Anderson, J. R. Ensher, and E. A. Cornell, “Evaporative cooling of rubidium atoms in a magnetic trap,” in “Fourteenth International Conference on Atomic Physics (ICAP XIV),” (Boulder, Colorado (USA), 1994), p. 7. [11](#), [87](#)
- [40] W. Petrich, M. H. Anderson, J. R. Ensher, and E. A. Cornell, “Stable, tightly confining magnetic trap for evaporative cooling of neutral atoms,” *Phys. Rev. Lett.* **74**, 3352–3355 (1995). [11](#), [12](#), [13](#), [39](#)
- [41] M. D. Barrett, J. A. Sauer, and M. S. Chapman, “All-optical formation of an atomic Bose-Einstein condensate,” *Phys. Rev. Lett.* **87**, 010404 (2001). [11](#)
- [42] Y.-J. Lin, A. R. Perry, R. L. Compton, I. B. Spielman, and J. V. Porto, “Rapid production of ^{87}Rb Bose-Einstein condensates in a combined magnetic and optical potential,” *Phys. Rev. A* **79**, 063631 (2009). [11](#)
- [43] T. Bergeman, G. Erez, and H. Metcalf, “Magnetostatic trapping fields for neutral atoms,” *Phys. Rev. A* **35**, 1535 (1987). [11](#), [12](#), [39](#), [85](#)
- [44] D. E. Pritchard, “Cooling neutral atoms in a magnetic trap for precision spectroscopy,” *Phys. Rev. Lett.* **51**, 1336 (1983). [13](#)
- [45] V. S. Bagnato, G. P. Lafyatis, A. G. Martin, E. L. Raab, R. N. Ahmad-Bitar, and D. E. Pritchard, “Continuous stopping and trapping of neutral atoms,” *Phys. Rev. Lett.* **58**, 2194–2197 (1987). [13](#)
- [46] M.-O. Mewes, M. R. Andrews, N. J. van Druten, D. M. Kurn, D. S. Durfee, and W. Ketterle, “Bose-Einstein condensation in a tightly confining dc magnetic trap,” *Phys. Rev. Lett.* **77**, 416–419 (1996). [13](#)

- [47] C. J. Myatt, E. A. Burt, R. W. Ghrist, E. A. Cornell, and C. E. Wieman, “Production of two overlapping Bose-Einstein condensates by sympathetic cooling,” *Phys. Rev. Lett.* **78**, 586–589 (1997). [13](#)
- [48] T. Esslinger, I. Bloch, and T. W. Hänsch, “Bose-Einstein condensation in a quadrupole-Ioffe-configuration trap,” *Phys. Rev. A* **58**, R2664 (1998). [13](#), [39](#)
- [49] J.-F. Schaff, P. Capuzzi, G. Labeyrie, and P. Vignolo, “Shortcuts to adiabaticity for trapped ultracold gases,” *New Journal of Physics* **13**, 113017 (2011). [14](#)
- [50] T. P. Meyrath, “Experiments with Bose-Einstein condensation in an optical box,” Ph.D. thesis, University of Texas at Austin (2005).
- [51] M. S. Yoon, “Experiments on magnetic transport, magnetic trapping, and Bose-Einstein condensation,” Ph.D. thesis, University of Oxford (2009). [14](#)
- [52] H. F. Hess, “Evaporative cooling of magnetically trapped and compressed spin-polarized hydrogen,” *Phys. Rev. B* **34**, 3476 (1986). [14](#)
- [53] W. Ketterle and N. J. van Druten, “Evaporative cooling of trapped atoms,” *Adv. At. Mol. Opt. Phys.* **37**, 181 (1996). [14](#)
- [54] V. Bagnato, D. E. Pritchard, and D. Kleppner, “Bose-Einstein condensation in an external potential,” *Phys. Rev. A* **35**, 4354–4358 (1987). [16](#)
- [55] F. Dalfovo, S. Giorgini, L. P. Pitaevskii, and S. Stringari, “Theory of Bose-Einstein condensation in trapped gases,” *Rev. Mod. Phys.* **71**, 463 (1999). [16](#)
- [56] E. Arimondo, “Laser controlled nanodeposition of neutral atoms,” *Applied Surface Science* **248**, 167 – 171 (2005). [17](#), [109](#)
- [57] W. Hänsel, P. Hommelhoff, T. Hänsch, and J. Reichel, “Bose-Einstein condensation on a microelectronic chip,” *Nature* **413**, 498–501 (2001). [17](#)
- [58] J. Reichel and V. Vuletic, eds., *Atom Chips* (Wiley-VCH, Weinheim, Germany, 2011).
- [59] J. Reichel, W. Hänsel, and T. W. Hänsch, “Atomic micromanipulation with magnetic surface traps,” *Phys. Rev. Lett.* **83**, 3398–3401 (1999). [17](#)
- [60] C. J. Myatt, N. R. Newbury, R. W. Ghrist, S. Loutzenhiser, and C. E. Wieman, “Multiply loaded magneto-optical trap,” *Opt. Lett.* **21**, 290 (1996). [19](#), [49](#), [50](#)
- [61] A. Chambers, R. K. Fitch, and B. S. Halliday, *Basic Vacuum Technology* (Institute of Physics Publishing, 1998). [23](#)
- [62] S. R. Mishra, S. P. Ram, S. K. Tiwari, and S. C. Mehendale, “Enhanced atom transfer in a double magneto-optical trap setup,” *Phys. Rev. A* **77**, 065402 (2008). [24](#), [66](#), [92](#), [109](#)
- [63] S. P. Ram, S. K. Tiwari, and S. R. Mishra, “A comparison of pulsed and continuous atom transfer between two magneto-optical traps.” *J. Korean Phys. Soc.* **57**, 1303–1307 (2010). [24](#), [66](#), [68](#), [110](#)

-
- [64] S. P. Ram, S. R. Mishra, S. K. Tiwari, and S. C. Mehendale, “Note: Investigation of atom transfer using a red-detuned push beam in a double magneto-optical trap setup,” *Rev. Sci. Instrum.* **82**, 126108 (2011). [24](#), [110](#)
- [65] C. E. Wieman and L. Hollberg, “Using diode lasers for atomic physics,” *Rev. Sci. Instrum.* **62**, 1 (1991). [27](#)
- [66] K. B. MacAdam, A. Steinbach, and C. Wieman, “A narrow band tunable diode laser system with grating feedback and a saturated absorption spectrometer for Cs and Rb,” *Am. J. Phys.* **60**, 1098 (1992). [29](#)
- [67] T. Ikegami, S. Sudo, and Y. Sakai, *Frequency Stabilization of Semiconductor Laser Diodes* (Artech House, Boston, 1995). [29](#)
- [68] L. Ricci, M. Weidemüller, T. Esslinger, A. Hemmerich, C. Zimmermann, V. Vuletic, W. König, and T. Hänsch, “A compact grating-stabilized diode laser system for atomic physics,” *Opt. Commun.* **117**, 541 – 549 (1995).
- [69] C. Ye, *Tunable External Cavity Diode Lasers* (World Scientific Publishing Co. Pte. Ltd., Singapore, 2004). [27](#)
- [70] H. Talvitie, A. Pietilainen, H. Ludvigsen, and E. Ikonen, “Passive frequency and intensity stabilization of extended-cavity diode lasers,” *Review of Scientific Instruments* **68**, 1–7 (1997). [28](#)
- [71] T. W. Hänsch, I. S. Shahin, and A. L. Schawlow, “High-Resolution Saturation Spectroscopy of the Sodium D Lines with a Pulsed Tunable Dye Laser,” *Phys. Rev. Lett.* **27**, 707 (1971). [29](#)
- [72] A. L. Schawlow, “Spectroscopy in a new light,” *Rev. Mod. Phys.* **54**, 697–707 (1982).
- [73] W. Demtröder, *Laser Spectroscopy* (Springer-Verlag, Berlin, 1982). [29](#)
- [74] S. P. Ram, S. K. Tiwari, S. R. Mishra, and H. S. Rawat, “Push beam spot-size dependence of atom transfer in a double magneto-optical trap setup,” *Rev. Sci. Instrum.* **84**, 073102 (2013). [34](#), [68](#), [110](#)
- [75] C. G. Townsend, N. H. Edwards, C. J. Cooper, K. P. Zetie, C. J. Foot, A. M. Steane, P. Szriftgiser, H. Perrin, and J. Dalibard, “Phase-space density in the magneto-optical trap,” *Phys. Rev. A* **52**, 1423–1440 (1995). [36](#), [53](#)
- [76] H. Ramchandran, “Temperature measurement of the cold cloud of atoms,” *Curr. Sci.* **76**, 213 (1999). [38](#)
- [77] D. S. Weiss, E. Riis, Y. Shevy, P. J. Ungar, and S. Chu, “Optical molasses and multilevel atoms: experiment,” *J. Opt. Soc. Am. B* **6**, 2072–2083 (1989). [38](#)
- [78] C. Salomon, J. Dalibard, W. D. Phillips, A. Clairon, and S. Guellati, “Laser cooling of cesium atoms below 3 micro K,” *Europhys. Lett.* **12**, 683 (1990).
- [79] C. J. Cooper, G. Hillenbrand, J. Rink, C. G. Townsend, K. Zetie, and C. J. Foot, “The temperature of atoms in a magneto-optical trap,” *Europhys. Lett.* **28**, 397–402 (1994). [64](#)

- [80] T. M. Brzozowski, M. Maczynska, M. Zawada, J. Zachorowski, and W. Gawlik, “Time-of-flight measurement of the temperature of cold atoms for short trap-probe beam distances,” *Journal of Optics B: Quantum and Semiclassical Optics* **4**, 62 (2002).
- [81] A. Mohapatra and C. Unnikrishnan, “High sensitivity probe absorption technique for time-of-flight measurements on cold atoms,” *Pramana* **66**, 1027–1035 (2006).
- [82] H. chao Zhang, P. fei Zhang, X. ping Xu, F. Cheng, and Y. zhu Wang, “Optimized temperature measurement with time-of-flight method,” *Optics Communications* **282**, 3278 – 3281 (2009). 38
- [83] P. Kohns, P. Buch, W. Sptitz, C. Csambal, and W. Ertmer, “On-line measurement of sub-Doppler temperatures in a Rb magneto-optical trap-by-trap centre oscillations,” *Europhys. Lett.* **22**, 517 (1993). 38
- [84] C. I. Westbrook, R. N. Watts, C. E. Tanner, S. L. Rolston, W. D. Phillips, P. D. Lett, and P. L. Gould, “Localization of atoms in a three-dimensional standing wave,” *Phys. Rev. Lett.* **65**, 33–36 (1990). 38
- [85] M. Mitsunaga, M. Yamashita, M. Koashi, and N. Imoto, “Temperature diagnostics for cold sodium atoms by transient four-wave mixing,” *Opt. Lett.* **23**, 840–842 (1998). 38
- [86] R. Silva, K. M. F. Magalhães, E. Henn, L. Marcassa, and V. Bagnato, “Temperature determination for magneto optical trapped atoms using a single parameter transient absorption,” *Opt. Commun.* **265**, 526 – 531 (2006). 38
- [87] S. Pradhan and B. N. Jagatap, “Measurement of temperature of laser cooled atoms by one-dimensional expansion in a magneto-optical trap,” *Review of Scientific Instruments* **79**, 013101 (2008). 38
- [88] T. Ray, A. Sharma, S. Jyothi, and S. A. Rangwala, “Temperature measurement of laser-cooled atoms using vacuum Rabi splitting,” *Phys. Rev. A* **87**, 033832 (2013). 38
- [89] S. H. Myrskog, J. K. Fox, H. S. Moon, J. B. Kim, and A. M. Steinberg, “Modified “ δ -kick cooling” using magnetic field gradients,” *Phys. Rev. A* **61**, 053412 (2000). 38, 93
- [90] V. B. Tiwari, S. R. Mishra, H. S. Rawat, S. Singh, S. P. Ram, and S. C. Mehendale, “Laser frequency stabilization and large detuning by doppler-free dichroic lock technique: Application to atom cooling,” *Pramana J. Phys.* **65**, 403–411 (2005). 38
- [91] V. B. Tiwari, “Studies with laser cooled and trapped Rb atoms,” Ph.D. thesis, Devi Ahilya Vishwavidyalaya, Indore (2009). 38
- [92] A. L. Migdall, J. V. Prodan, W. D. Phillips, T. H. Bergeman, and H. J. Metcalf, “First observation of magnetically trapped neutral atoms,” *Phys. Rev. Lett.* **54**, 2596–2599 (1985). 39, 85

-
- [93] W. Ketterle, D. S. Durfee, and D. M. Stamper-Kurn, “Making, probing and understanding Bose-Einstein condensates,” in “Proceedings of the International School of Physics - Enrico Fermi,” , M. Inguscio, S. Stringari, and C. E. Wieman, eds. (IOS Press, 1999), p. 67. 43
- [94] J. E. Lye, C. S. Fletcher, U. Kallmann, H.-A. Bachor, and J. D. Close, “Images of evaporative cooling to Bose-Einstein condensation,” *Journal of Optics B: Quantum and Semiclassical Optics* **4**, 57 (2002).
- [95] W. Yu-Zhu, Z. Shu-Yu, L. Quan, Z. Shan-Yu, and F. Hai-Xiang, “Evidence for a Bose-Einstein condensate in dilute Rb gas by absorption image in a quadrupole and Ioffe configuration trap,” *Chinese Physics Letters* **20**, 799 (2003). 43
- [96] K. Gibble, S. Chang, and R. Legere, “Direct observation of *s*-wave atomic collisions,” *Phys. Rev. Lett.* **75**, 2666–2669 (1995). 49
- [97] A. Steane, P. Szriftgiser, P. Desbiolles, and J. Dalibard, “Phase modulation of atomic de Broglie waves,” *Phys. Rev. Lett.* **74**, 4972–4975 (1995). 49
- [98] M. A. Kasevich, D. S. Weiss, E. Riis, K. Moler, S. Kasapi, and S. Chu, “Atomic velocity selection using stimulated Raman transitions,” *Phys. Rev. Lett.* **66**, 2297–2300 (1991). 49
- [99] Z. T. Lu, K. L. Corwin, M. J. Renn, M. H. Anderson, E. A. Cornell, and C. E. Wieman, “Low-velocity intense source of atoms from a magneto-optical trap,” *Phys. Rev. Lett.* **77**, 3331–3334 (1996). 49
- [100] C. Y. Park, M. S. Jun, and D. Cho, “Magneto-optical trap loaded from a low-velocity intense source,” *J. Opt. Soc. Am. B* **16**, 994–997 (1999). 49
- [101] E. Donley, T. Heavner, and S. Jefferts, “Optical molasses loaded from a low-velocity intense source of atoms: an atom source for improved atomic fountains,” *Instrumentation and Measurement, IEEE Transactions on* **54**, 1905–1910 (2005). 49
- [102] J. Arlt, O. Marago, S. Webster, S. Hopkins, and C. Foot, “A pyramidal magneto-optical trap as a source of slow atoms,” *Opt. Commun.* **157**, 303–309 (1998). 49
- [103] R. Williamson III, P. Voytas, R. Newell, and T. Walker, “A magneto-optical trap loaded from a pyramidal funnel,” *Opt. Express* **3**, 111–117 (1998). 49
- [104] H. J. Lewandowski, D. M. Harber, D. L. Whitaker, and E. A. Cornell, “Simplified system for creating a Bose-Einstein condensate,” *J. Low. Temp. Phys.* **132**, 309–367 (2003). 49, 94
- [105] J. Goldwin, S. Inouye, M. L. Olsen, B. Newman, B. D. DePaola, and D. S. Jin, “Measurement of the interaction strength in a Bose-Fermi mixture with 87Rb and 40K,” *Phys. Rev. A* **70**, 021601 (2004). 49
- [106] T. B. Swanson, D. Asgeirsson, J. A. Behr, A. Gorelov, and D. Melconian, “Efficient transfer in a double magneto-optical trap system,” *J. Opt. Soc. Am. B* **15**, 2641–2645 (1998). 49, 50

- [107] W. Wohlleben, F. Chevy, K. Madison, and J. Dalibard, “An atom faucet,” *Eur. Phys. J. D* **15**, 237–244 (2001). [67](#)
- [108] L. Cacciapuoti, A. Castrillo, M. de Angelis, and G. Tino, “A continuous cold atomic beam from a magneto-optical trap,” *Eur. Phys. J. D* **15**, 245–249 (2001). [49](#), [62](#), [67](#)
- [109] S. R. Mishra, S. K. Tiwari, S. P. Ram, and S. C. Mehendale, “Generation of hollow conic beam using a metal axicon mirror,” *Opt. Eng.* **46**, 084002 (1–5) (2007). [53](#)
- [110] S. Pradhan, S. J. Gaur, K. G. Manohar, and B. N. Jagatap, “Enhancement in the number of trapped atoms in a cesium magneto-optical trap by a near-resonant control laser,” *Phys. Rev. A* **72**, 053407 (2005). [55](#)
- [111] S. G. Miranda, S. R. Muniz, G. D. Telles, L. G. Marcassa, K. Helmerson, and V. S. Bagnato, ““Dark-spot” atomic-beam slowing for on-axis loading of traps,” *Phys. Rev. A* **59**, 882–885 (1999). [56](#)
- [112] V. S. Bagnato, L. G. Marcassa, S. G. Miranda, S. R. Muniz, and A. L. de Oliveira, “Measuring the capture velocity of atoms in a magneto-optical trap as a function of laser intensity,” *Phys. Rev. A* **62**, 013404 (2000). [57](#), [79](#)
- [113] S. R. Muniz, K. M. F. Magalhães, P. W. Courteille, M. A. Perez, L. G. Marcassa, and V. S. Bagnato, “Measurements of capture velocity in a magneto-optical trap for a broad range of light intensities,” *Phys. Rev. A* **65**, 015402 (2001). [64](#)
- [114] A. Ashkin, “Trapping of atoms by resonance radiation pressure,” *Phys. Rev. Lett.* **40**, 729–732 (1978). [67](#), [72](#), [81](#)
- [115] J. Dalibard and C. Cohen-Tannoudji, “Dressed-atom approach to atomic motion in laser light: the dipole force revisited,” *J. Opt. Soc. Am. B* **2**, 1707–1720 (1985). [67](#), [72](#), [81](#)
- [116] M. Schiffer, M. Rauner, S. Kuppens, M. Zinner, K. Sengstock, and W. Ertmer, “Guiding, focusing, and cooling of atoms in a strong dipole potential,” *Appl. Phys. B* **67**, 705–708 (1998). [67](#)
- [117] J. Yin, Y. Zhu, W. Jhe, and Z. Wang, “Atom guiding and cooling in a dark hollow laser beam,” *Phys. Rev. A* **58**, 509–513 (1998).
- [118] X. Xu, V. G. Minogin, K. Lee, Y. Wang, and W. Jhe, “Guiding cold atoms in a hollow laser beam,” *Phys. Rev. A* **60**, 4796–4804 (1999).
- [119] K. Szymaniec, H. J. Davies, and C. S. Adams, “An atomic fountain guided by a far-off resonance laser beam,” *Europhys. Lett.* **45**, 450–455 (1999). [67](#)
- [120] L. Pruvost, D. Marescaux, O. Houde, and H. T. Duong, “Guiding and cooling of cold atoms in a dipole guide,” *Opt. Commun.* **166**, 199–209 (1999). [67](#)
- [121] D. Müller, E. A. Cornell, D. Z. Anderson, and E. R. I. Abraham, “Guiding laser-cooled atoms in hollow-core fibers,” *Phys. Rev. A* **61**, 033411 (2000).

-
- [122] B. T. Wolschrijn, R. A. Cornelussen, R. J. C. Spreeuw, and H. B. van Linden van den Heuvell, “Guiding of cold atoms by a red-detuned laser beam of moderate power,” *New J. Phys.* **4**, 69 (2002).
- [123] M. J. Pritchard, A. S. Arnold, S. L. Cornish, D. W. Hallwood, C. V. S. Pleasant, and I. G. Hughes, “Transport of launched cold atoms with a laser guide and pulsed magnetic fields,” *New J. Phys.* **8**, 309 (2006).
- [124] L. Ke, W. Xiao-Rui, H. Ling-Xiang, Z. Ming-Sheng, and L. Bao-Long, “Enhancement of transfer efficiency of cold atoms using an optical guiding laser beam,” *Chinese Phys. Lett.* **24**, 2562 (2007). [67](#)
- [125] Y. Shu-Bin, G. Tao, Z. Tian-Cai, and W. Jun-Min, “Continuously transferring cold atoms in caesium double magneto-optical trap,” *Chinese Phys.* **15**, 1746 (2006). [67](#)
- [126] E. Dimova, O. Morizot, G. Stern, C. G. Alzar, A. Fioretti, V. Lorent, D. Comparat, H. Perrin, and P. Pillet, “Continuous transfer and laser guiding between two cold atom traps,” *Eur. Phys. J. D* **42**, 299–308 (2007). [67](#), [68](#), [81](#)
- [127] J. Wang, J. Wang, S. Yan, T. Geng, and T. Zhang, “Transferring cold atoms in double magneto-optical trap by a continuous-wave transfer laser beam with large red detuning,” *Rev. Sci. Instrum.* **79**, 123116 (2008). [68](#), [81](#)
- [128] X. Xu, Y. Wang, and W. Jhe, “Theory of atom guidance in a hollow laser beam: dressed-atom approach,” *J. Opt. Soc. Am. B* **17**, 1039–1050 (2000). [72](#), [81](#)
- [129] A. M. Steane, M. Chowdhury, and C. J. Foot, “Radiation force in the magneto-optical trap,” *J. Opt. Soc. Am. B* **9**, 2142 (1992). [79](#)
- [130] D. Yum, J. Park, W. Lee, and W. Jhe, “Systematic study of the rf-induced evaporation of ^{87}Rb atoms in a spherical magnetic quadrupole trap,” *J Korean Phys. Soc.* **60**, 1–5 (2012). [94](#)
- [131] M.-O. Mewes, “Bose-Einstein condensation of sodium atoms,” Ph.D. thesis, Massachusetts Institute of Technology (1997). [96](#)
- [132] M. Landini, “A tunable Bose-Einstein condensate for quantum interferometry,” Ph.D. thesis, University of Trento (2012). [96](#)
- [133] J. Stuhler, P. O. Schmidt, S. Hensler, J. Werner, J. Mlynek, and T. Pfau, “Continuous loading of a magnetic trap,” *Phys. Rev. A* **64**, 031405 (2001). [97](#), [102](#)
- [134] S. P. Ram, S. R. Mishra, S. K. Tiwari, and H. S. Rawat, “Temperature and phase-space density of cold atom cloud in a quadrupole magnetic trap,” Submitted. [110](#)